

**Multiscale Characterization and Design for 3D Concrete Printing: Material Formulation,
Printing Process, and Mechanical Behavior**

A Report

by

Bo Rider

Completed During the Degree
Master of Science in Civil Engineering
School of Civil and Environmental Engineering

Georgia Institute of Technology

January 2026

Multiscale Characterization and Design for 3D Concrete Printing: Material Formulation, Printing
Process, and Mechanical Behavior

Advisors:

Dr. Kimberly Kurtis, Co-Advisor
School of Civil and Environmental Engineering
Georgia Institute of Technology

Dr. Lauren Stewart, Co-Advisor
School of Civil and Environmental Engineering
Georgia Institute of Technology

ACKNOWLEDGEMENTS

Thank you to all who have supported me through a time of amazing personal and professional growth. I have gained an incredible amount of technical knowledge, creative problem-solving skills, and insight into the academic research process. Every person I have met at Georgia Tech has played a role in that.

To my advisors and the other professors I have built relationships with: thank you for your guidance, assistance, and education. To the incredible staff in CEE: you made working in this department a true delight. To our project sponsors: I greatly appreciate your support and enthusiasm towards our work. To my labmates and colleagues: your friendship has carried me through the highs and lows, and I truly could not have done this without you. To my family: your unconditional support through this journey has been invaluable.

I will greatly miss the family I have at Georgia Tech, and I will carry you all with me as I move onto the next chapter.

TABLE OF CONTENTS

ACKNOWLEDGEMENTS.....	iii
TABLE OF CONTENTS.....	iv
LIST OF TABLES.....	vii
LIST OF FIGURES.....	viii
NOMENCLATURE.....	xi
SUMMARY.....	xv
CHAPTER 1. INTRODUCTION.....	xv
1.1. Motivation and Objectives.....	1
1.2. Report Structure.....	3
CHAPTER 2. LITERATURE REVIEW—SHOULD PROCESS DESIGN FOR 3D CONCRETE PRINTING RELY ON RHEOLOGY?.....	4
Abstract.....	4
2.1. Introduction.....	4
2.2. Background.....	5
2.2.1. Review of 3DCP Processes.....	5
2.2.2. Relevant Rheological Theory.....	6
2.3. Mixture Design for 3DCP.....	13
2.3.1. Rheological Properties of 3DCP Mixtures.....	13
2.3.2. Common Features of 3DCP Mixtures.....	14
2.4. Rheological Criteria for 3DCP.....	15
2.4.1. Criteria for Buildability.....	15
2.4.2. Criteria for Printability.....	17
2.4.3. Rheological Modeling.....	19
2.5. Other Fresh-State Characterization Methods.....	20
2.5.1. Soil Mechanics Type Characterization.....	20
2.5.2. Other Mechanical Tests.....	21
2.5.3. Non-Mechanical and Indirect Tests.....	22
2.6. Applicability of Rheology to 3DCP.....	23
2.6.1. Paste-Scale to Mortar-Scale.....	24
2.7. Discussion.....	25
2.8. Conclusions and Future Work.....	27

CHAPTER 3. INVESTIGATION OF MICROSTRUCTURAL AND MACROPHYSICAL ANISOTROPY IN STEEL-FIBER-REINFORCED 3D-PRINTED CEMENTITIOUS COMPOSITE	29
Abstract	29
3.1. Introduction	29
3.2. Experiment	30
3.3. Results	35
3.3.1. Flexural Testing	35
3.3.2. Sorptivity Testing	36
3.3.3. Microstructure Quantification via μ CT	38
3.4. Discussion	40
3.5. Conclusions	43
CHAPTER 4. EVALUATION OF MACHINE-LEARNED OSCILLATORY RHEOLOGY TO DESIGN BLENDED CEMENT SYSTEMS FOR 3D PRINTING	45
Abstract	45
4.1. Introduction	46
4.2. Background	48
4.2.1. Oscillatory Rheology of Cement-Based Materials	48
4.2.2. HML Modeling	50
4.3. Experiment	51
4.3.1. Materials	51
4.3.2. Rheometry	53
4.3.3. Data Analysis	55
4.3.4. Validation and Printing	59
4.4. Results	60
4.4.1. Rheological Properties	60
4.4.2. Model Performance and Predictions	67
4.4.3. Validation by Printing: Paste to Mortar Scale	78
4.5. Discussion	79
4.6. Conclusions	82
CHAPTER 5. INSIGHTS INTO THE COMPRESSIVE AND FLEXURAL BEHAVIOR OF 3D-PRINTED CONCRETE THROUGH DIGITAL IMAGE CORRELATION	85
Abstract	85
5.1. Introduction	85
5.2. Background	87

5.3.	Experiment.....	88
5.3.1.	Materials	88
5.3.2.	Printing and Specimen Preparation.....	90
5.3.3.	Mechanical Testing.....	90
5.3.4.	Digital Image Correlation	92
5.4.	Bulk Mechanical Properties.....	94
5.4.1.	Compression	94
5.4.2.	Flexure	96
5.5.	Image Analysis.....	97
5.5.1.	Compression	97
5.5.2.	Flexure	100
5.6.	Conclusions.....	104
CHAPTER 6. CONCLUSIONS AND RECOMMENDATIONS		106
6.1.	Conclusions.....	106
6.2.	Recommendations for Practice	106
6.3.	Recommendations for Future Work.....	107
REFERENCES		109

LIST OF TABLES

Table 3.1. Mixture design of the printed material, normalized by weight of portland cement....	31
Table 3.2. Selected settings and resulting resolution (voxel size) for μ CT scanning.	35
Table 3.3. Absorption and total absorbed mass after 48 hours.	37
Table 4.1. Oxide composition of PC and MK in percent by weight.	52
Table 4.2. Phase composition of PC.	52
Table 4.3. Physical characteristics of PC and MK.....	52
Table 4.4. Physical characteristics of the sand used.	52
Table 4.5. Measured rheological properties by mixture composition. Values should be taken as having three significant figures, with time values to the nearest 30 seconds.	60
Table 4.6. Pearson correlation coefficients of four selected rheological properties.	62
Table 4.7. Linear regression coefficients and accuracy for rheological properties.....	73
Table 4.8. Relative feature importance in determining testability.	74
Table 4.9. Accuracy of GPR models for rheological properties.	75
Table 4.10. Comparison of predicted and measured rheological properties of candidate mixtures, as predicted with logarithmic transform and with physical units. Values should be taken as having three significant figures, with time values to the nearest 30 seconds.	78
Table 4.11. Selected mortar design for printing, from Candidate Mixture I.....	79
Table 5.1. Oxide composition of the commercial 3DCP binder.	89
Table 5.2. Printer settings used in this experiment. Note that the horizontal offset corresponds to an adjacent layer overlap of 10%, while the vertical offset exactly matches the desired layer height. The horizontal and vertical interlayer times are not constant.....	90
Table 5.3. Tests conducted and naming convention.	91
Table 5.4. Loading rates for the four types of specimens tested.....	92
Table 5.5. Parameters for digital image correlation.	93
Table 5.6. Average compressive strength by orientation and age.....	95
Table 5.7. Average elastic modulus in compression by orientation and age.	95
Table 5.8. Average flexural strength by orientation and size.....	96
Table 5.9. Average elastic modulus in flexure by orientation and size.	97

LIST OF FIGURES

Fig. 2.1. Common types of rheological behaviors.....	8
Fig. 2.2. Phased stress-strain behavior in oscillatory rheometry, and characteristic of viscoelastic materials.....	10
Fig. 2.3. Shear moduli in a sample subjected to logarithmically increasing strain.	12
Fig. 2.4. Shear stress-strain curve of a cementitious sample in oscillatory rheology. The red star represents the yield point.	12
Fig. 2.5. The two predominant failure modes during printing in 3DCP.....	16
Fig. 2.6. A cross-section of hose during concrete pumping, exhibiting formation of a fines-rich lubrication layer due to shear-induced particle migration.	18
Fig. 3.1. Gradation of aggregate used in printing material.	32
Fig. 3.2. Flexural testing of printed beam specimens.	34
Fig. 3.3. Sorptivity testing of cores from printed and cast beam specimens.	34
Fig. 3.4. Stress-deflection curves of flexural testing of printed and cast beams	36
Fig. 3.5. Sorptivity test curve, with printed and cast samples from the edge and bulk regions exposed to solution and monitored for 48 hours. Plotting absorption against the square root of time follows the ASTM C1585 convention.	37
Fig. 3.6. Distributions of void aspect ratio, void size, and fiber alignment of printed and cast samples. An aspect ratio of 1 is a perfect sphere, and an angle of 90° corresponds to the printing direction.	39
Fig. 3.7. μ CT image of voids in the printed sample, colored by aspect ratio (1 = perfectly spherical).....	41
Fig. 3.8. μ CT image of fibers in the printed sample, colored by orientation (90° = longitudinal, i.e., printing direction).	42
Fig. 4.1. Particle size distributions of binder powders and aggregate.	53
Fig. 4.2. Storage modulus and flow onset stress of mixtures of varying water-binder ratios.	63
Fig. 4.3. Storage modulus and flow onset stress of mixtures of varying metakaolin substitutions.	64

Fig. 4.4. Open time for systems with constant w/b of 0.40 with varying metakaolin substitution and superplasticizer dosage.....	65
Fig. 4.5. Storage modulus and flow onset stress of mixtures of varying superplasticizer dosages.	66
Fig. 4.6. Storage modulus and flow onset stress of neat, blended, and plasticized mixtures all with w/b 0.40.	67
Fig. 4.7. Zeta potential as a function of superplasticizer dosage for a PLC only system and one with 30% MK. Adapted from [183].....	71
Fig. 4.8. Hierarchical machine learning approach utilized in this study.	72
Fig. 4.9. Confusion matrix from LOOCV for classification of mixtures as testable or not testable.	73
Fig. 4.10. Parity plot for predictions of G' (a) and t_{open} (b). Error bars represent one standard deviation of predicted probability distribution at individual points, while the shaded region represents one standard deviation of global prediction error over the whole dataset.	77
Fig. 4.11. Printing of the mortar designed from candidate mixture I.	79
Fig. 5.1. Mapping of the deformation of a subset with respect to a reference configuration.	88
Fig. 5.2. Size distribution of the binder and aggregate portions of the printable material.	89
Fig. 5.3. Printed specimen orientation and axis convention.	91
Fig. 5.4. Orientations of beams tested. Solid lines represent vertical interlayers, and dashed lines represent adjacent interlayers.....	92
Fig. 5.5. Testing setup for digital image correlation.....	94
Fig. 5.6. The normal horizontal strain field for a cast cube.....	98
Fig. 5.7. The normal horizontal strain field for a printed cube with compression parallel to the Z axis.	99
Fig. 5.8. The normal horizontal strain field for a printed cube with compression parallel to the Y axis.	100
Fig. 5.9. The normal longitudinal strain field for a cast beam.....	101
Fig. 5.10. The normal longitudinal strain field for a printed beam with bending about the X axis.	102
Fig. 5.11. The normal longitudinal strain field of a printed beam with bending about the Y axis.	103

Fig. 5.12. The normal longitudinal strain field of a printed beam with bending about the Z axis.

..... 104

NOMENCLATURE

Abbreviations

1K	One-component printing system
2K	Two-component printing system
3D	Three-dimensional
3DCP	3D concrete printing
ANOVA	Analysis of variance
ARD	Automatic relevance determination
ASTM	American Society for Testing and Materials
DIC	Digital image correlation
GPR	Gaussian process regression
HML	Hierarchical machine learning
KI	Potassium iodide
LASSO	Least absolute shrinkage and selection operator
LC3	Limestone – calcined clay cement
LOOCV	Leave-one-out cross-validation
LVER	Linear viscoelastic regime
MK	Metakaolin
OPC	Ordinary portland cement
PLC	Portland – limestone cement
RILEM	International Union of Laboratories and Experts in Construction Materials, Systems, and Structures
RMSE	Root mean square error
SG	Specific gravity
SIPM	Shear-induced particle migration
SP	Superplasticizer
SSA	Specific surface area
SSD	Saturated – surface dry
μ CT	Computed microtomography

Symbols

A	Amplitude
A_s	Volumetric specific surface area
a	Loosening effect function
a/b	Aggregate-binder ratio, by mass
b	Wall effect function; element width
C	Cohesion; concentration
d	Particle diameter
E	Young's modulus
f	Mass fraction of a binder component
G	Shear modulus
G'	Storage modulus
G''	Loss modulus
G^*	Complex shear modulus
g	Acceleration due to gravity
H	Object height
h	Layer height
i	Mathematical constant = $\sqrt{-1}$
K	Herschel-Bulkley consistency index; particle packing index; Freundlich cofactor
k	Krieger-Dougherty exponent; Chateau-Ovarlez-Trung exponent
n	Herschel-Bulkley flow index; inverse of Freundlich exponent
\vec{p}	Parameter vector
p	Statistical significance
R^2	Coefficient of determination
\sin	Sine function
t	Time
t_{open}	Open time
TPD	Total particle density
WFT	Water film thickness

w/b	Water-binder ratio, by mass
X	Predictors, in linear regression
\vec{X}	Position vector
y	Response, in linear regression
β	Ideal packing fraction; linear regression coefficients
γ	Shear strain; virtual packing density
$\dot{\gamma}$	Shear strain rate
$\Delta\vec{X}$	Deformation vector
δ	Phase shift angle
ε	Regression error; strain
ζ	Zeta potential
η	Plastic viscosity
η'	Real component of viscosity, in oscillatory rheology
η''	Imaginary component of viscosity, in oscillatory rheology
η^*	Complex viscosity, in oscillatory rheology
θ	Proportion of adsorbed species
λ	Complexity penalization parameter
μ	Proportion of voids
μ_w	Portion of voids ratio responsible for filling interparticle porosity
μ'_w	Portion of voids due to excess water
ν	Poisson's ratio
$\tilde{\xi}$	Shape function
π	Mathematical constant ≈ 3.14
ρ	Density
Σ	Summation function
σ	Stress
σ_n	Normal stress
τ	Shear stress
τ_0	Yield stress
τ_M	Flow onset stress

ϕ	Solid volume fraction
ϕ_m	Random packing density
φ	Angle of internal friction
ω	Rotational frequency

SUMMARY

The field of 3D concrete printing (3DCP) has attracted growing interest from both research and industry, yet its successful implementation remains limited by an incomplete understanding of the processes governing printability and structural performance. While prior work has emphasized the importance of fresh-state material tailoring and process design and control, the fundamental mechanisms linking these criteria to material behavior and mechanical performance are not yet well established.

This report investigates the relationships between 3DCP processing, material structure, and mechanical response in cementitious materials. The influence of printing is explicitly examined by linking microstructural characteristics of printed and cast components to their macroscopic physical behavior. Rheological measurements are used to guide the development of printable material formulations and to evaluate the role of fresh-state mechanical behavior in printing success. Additionally, the compressive and flexural responses of printed and cast specimens are quantitatively and qualitatively compared to assess the effects of printing-induced anisotropy and interlayer interfaces on mechanical failure.

Collectively, this work advances the scientific understanding of cementitious materials in the context of additive manufacturing, contributing to improved reliability and performance of 3D concrete printing as a construction technology.

CHAPTER 1. INTRODUCTION

1.1. Motivation and Objectives

Modern concrete construction is governed by expensive labor and comparably cheap building materials. This phenomenon has led to the widespread adoption of repeatable, standardized, and prismatic structural forms which liberally add material volume to the structure to simplify construction and reduce labor [1]. Today's most common construction methods thus may use excess material—and contribute to additional carbon emissions—for limited structural advantage.

Recent innovations in advanced manufacturing and construction automation provide opportunities to reduce dependence on labor. Additionally, modern material formulations allow for reduced carbon emissions and cost through the use of largely abundant materials which require less processing than conventional portland cement [2]. By combining these advances, multiple thrusts of sustainability are addressed; both material consumption and energy-intensity are reduced.

Three-dimensional (3D) concrete printing (3DCP) utilizes the automated deposition of concrete or mortar (in the common case in which coarse aggregate is omitted) layers to create a free-form, self-supporting structure without the use of formwork. Initially conceptualized as “contour crafting” by Khoshnevis [3], the technology has been the subject of rapid development in both research and industrial applications; several structural-scale 3DCP applications have been realized, including double-story buildings and mid-span pedestrian bridges [4,5]. A primary challenge of this technology is that the material must immediately support load, even in the fresh state. The current state-of-the-art relies on highly controlled material rheology so that it has

relatively low viscosity (resistance to flow) for pumpability and high yield stress (stress required to initiate flow) and initial stiffness for layering, or “buildability,” all with a system-dependent appropriate open time [6]. Then, it is possible to extrude complicated structures which support their own weight immediately after deposition, and the weight of additional layers shortly thereafter. While mixtures for 3DCP have often relied on high paste content [7], modern cement systems—including limestone – calcined clay cement (LC3) [8]—may provide synergistic benefits on both sustainability and rheology [9].

As a relatively immature technology, 3DCP faces challenges in being applied at a heavy-structural scale, including high-rise structures and roadway bridges. In general, a lack of fundamental information on the rheology and early-age mechanical behavior, microstructural anisotropy, and hardened-state mechanics and failure of printed cementitious materials precludes further development, in addition to the challenge of reinforcing free-formed printed structures [10]. This research aims to fill missing links in critical composition – process – property relationships for 3DCP.

The objectives of this research can thus be summarized as follows:

1. Determine effect of blending and plasticizing on transient and temporal rheological properties of fresh cement systems.
2. Develop design approach for formulations of blended, plasticized cement systems for 3D-printing applications using rheology and machine learning.
3. Quantify microstructural anisotropy, fiber alignment, and macroscale physical behavior in 3D-printed cementitious composites.
4. Compare mechanisms of anisotropy and softening in cast and 3D-printed mortars.

1.2. Report Structure

This report is organized into six chapters. Chapter 1 is the introduction, containing background and motivating information and a definition of the research objectives. Chapter 2 reviews the current state of the art in 3DCP in the context of rheology, identifying research gaps which are addressed throughout the work. Chapters 3 through 5 represent the major research findings, moving up in physical scale as the report progresses. Chapter 3 evaluates the microstructure of 3D-printed, fiber reinforced cementitious composites and relates these observations to macroscale, physical behavior. Chapter 4 provides a combined experimental-analytical mix design procedure for blended cement systems based on rheological characterization and machine learning, and validates this procedure through printing. Chapter 5 analyzes the hardened-state behavior in 3DCP through mechanical testing and digital image correlation. Chapter 6 represents the main conclusions of the work and provides recommendations for both practice and future research works.

CHAPTER 2. LITERATURE REVIEW—SHOULD PROCESS DESIGN FOR 3D CONCRETE PRINTING RELY ON RHEOLOGY?

Abstract

3D concrete printing (3DCP) is a construction methodology which places stringent and often conflicting demands on the printing material, due to the need of the material to be pumped and extruded yet also stacked vertically. Many researchers have relied on rheology to inform design of the 3DCP process to avoid collapse of the printed part, as rheology provides a mechanical characterization framework for soft, viscoelastic materials. However, difficulties exist in implementing the findings of rheometric testing in 3DCP process design. This review examines the applicability of such techniques, and other fresh-state characterization methods, to 3DCP. It is explained that rheology provides a strong fundamental understanding of the mechanistic behavior of fresh cement-based systems, though rheometric testing may be insufficient for fully designing 3DCP structures for fresh-state integrity.

2.1. Introduction

3D concrete printing (3DCP) shows promise as an advanced construction manufacturing technology due to its ability to create free-formed, optimized structures while eliminating the need for formwork and heavily reducing required labor [1,3]. Due to the lack of supportive and protective formwork, the fresh-state behavior of the 3D printable material is especially critical, as structures become highly prone to failure during concrete placement. Currently, the difficulty of reliably achieving required fresh-state behavior poses a serious barrier to widespread adoption of this construction technology [11].

Researchers and practitioners have relied on many methods to design the printing material for adequate fresh-state behavior, though rheological characterization has been especially prominent [12]. Many materials, cementitious and otherwise, are designed with rheology as a primary focus, including self-consolidating concrete (SCC), shotcrete, oil-well cement slurries, paints, cosmetics, and food products.

Fresh-state characterization techniques are used to quantify *printability* (ability to be extruded as a smooth, continuous filament) and *buildability* (ability to withstand the weight imposed by successively stacked layers). However, despite extensive analysis of the material, rheological and otherwise, 3DCP processes have proven sensitive, variable, and prone to fresh-state failure [5,13,14]. Overall, by reviewing the applications of rheometry to 3DCP design, this chapter will explore the following question—is the 3D concrete printing process best designed through a rheological framework?

2.2. Background

2.2.1. Review of 3DCP Processes

3DCP relies on automated, robotically-controlled deposition of material into a predetermined layout. Strictly speaking, the printing material is often a mortar, not a concrete, due to the use of only fine aggregate. Success in 3DCP construction is governed by the material's ability to be 1) conveyed through the printer system (*pumping*), 2) deposited through the nozzle without blockages or filament tearing (*extrusion*), and 3) assembled into the desired structure without collapse (*building*). Each of these three subprocesses require specific, and sometimes conflicting, fresh-state material properties (explained further in Section 2.3.1).

Different types of printers will induce different material demands. Typically, printer systems are either suspended from a planar gantry or mounted to a multi-axis robotic arm. While gantry printers are (in theory) only limited in size by how large the enveloping gantry can be built, robotic arms often have more precise geometric control by incorporating rotational degrees of freedom. There are several impacts the printer type can have on the process. For example, a large gantry printer may require the material to be pumped tens of meters, requiring a highly stable mix to avoid pressure-induced segregation with a long open time to avoid setting in the hose. Additionally, a robotic arm system that seeks to leverage rotational degrees of freedom to print structures with overhangs (i.e., not perfectly vertical) will require a sufficiently strong mixture capable of such self-support [15–17].

Finally, printers may rely on injecting the material with an accelerant at the nozzle for fine-tuned rheology control or “set-on-demand” [18]. Such systems are called “two-component” or 2K, and unique properties of 2K printing mixtures are discussed later in the chapter. The alternative are printers which rely on the mixture being sufficiently stiff at deposition without additional enhancement, 1K. As will be discussed in Section 2.3.2, 1K and 2K mixes can have different rheological requirements.

2.2.2. Relevant Rheological Theory

Rheology is the study of mechanics of flow and deformation of soft materials. It is applied to materials that exhibit both viscous (liquid-like) and elastic (solid-like) behavior [19]. Concrete is a viscoelastic material, and its fresh-state behavior is commonly of interest due to workability and placement concerns; the slump test can be considered a rudimentary quantification of rheological behavior. However, rheometry gives a much more sophisticated insight into the mechanics of the fresh material. Rheometers measure the torque and rotational displacement of

soft materials, allowing for defined relationships between shear stress and strain. Importantly, conventional rheometers typical to other industries (such as polymer engineering and food science) are typically of the size that cementitious pastes are tested (without aggregates), rather than mortars or concretes. Larger rheometers specifically designed for mortars and concretes are available, though less common in research and practice [20].

Many models exist to relate shear stress and strain in rheology. It is common to seek a relationship between shear stress, τ , and the strain rate, $\dot{\gamma}$, by continuously rotating the sample [21]. In Newtonian fluids, this relationship is linear, with the proportionality constant being called the plastic viscosity, η . Newtonian fluids include water and oils. However, some fluids require a non-zero applied stress to initiate flow, called the yield stress, τ_0 . The Bingham model, given in Eq. 2.1, is the simplest constitutive law for yield stress fluids, relating the shear stress to the strain rate through the plastic viscosity and the yield stress.

$$\tau = \tau_0 + \eta\dot{\gamma} \quad (2.1)$$

Additionally, many materials exhibit a non-linear relationship between shear stress and strain rate. Such materials are called shear thinning if their apparent plastic viscosity decreases with increasing shear rate, and shear thickening if their apparent plastic viscosity increases with increasing shear rate; cement suspensions are often shear thinning at typical shear rates and material formulations [21]. Other examples of shear thinning fluids include paints and ketchup, while cornstarch slurry is a common shear thickening fluid. Such fluids are commonly described using the Herschel-Bulkley model (see Eq. 2.2), a generalized form of the Bingham model.

$$\tau = \tau_0 + K\dot{\gamma}^n \quad (2.2)$$

The flow index, n , characterizes the non-linear viscous behavior ($n = 1$ describes ideal Bingham behavior, $n < 1$ corresponds to shear thinning, $n > 1$ represents shear thickening) and K is an empirical constant. Fig. 2.1 shows a visual summary of common types of rheological behaviors in fluids.

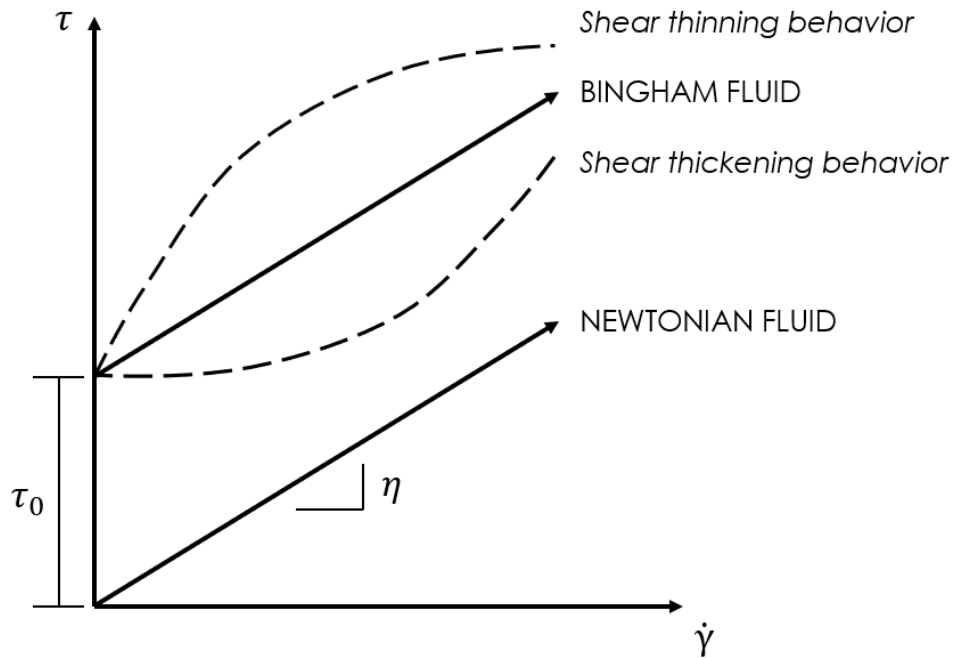


Fig. 2.1. Common types of rheological behaviors.

Finally, the rheological behavior of some complex fluids is thixotropic, in that it depends on the physical arrangement of its microstructure, which in turn depends on previous flow history and allowed time for particle flocculation. Cementitious systems are thixotropic, and thus see their yield stress and viscosity increase immediately after the cessation of flow as the microstructure reassembles. Notably, thixotropy is an entirely physical phenomenon and is completely reversible; chemical hardening also stiffens the cementitious material, though is irreversible and is a distinct, though overlapping, process.

2.2.2.1. Oscillatory Rheometry

Modern rheology also commonly utilizes oscillatory measurements, whereby repeated back-and-forth perturbations are placed on the same material sample to elucidate its direct stress-strain response, rather than applying continuous rotation and using strain rate as the control variable. Oscillatory rheometry allows for the separation of viscous and elastic components of a viscoelastic material.

When rotating the sample repeatedly, the elastic and viscous components of mechanical response are those with stress and strain entirely in phase and entirely out-of-phase, respectively [21].

Given a harmonic applied strain (Eq. 2.3), the stress response will be harmonic and may have a phase shift (Eq. 2.4).

$$\gamma(t) = A_\gamma \sin(\omega t) \quad (2.3)$$

$$\tau(t) = A_\tau \sin(\omega t + \delta) \quad (2.4)$$

Where ω is the rotational frequency and δ is the phase angle. $\delta = 0$ represents the ideally elastic case, where the material behaves as a Hookean solid; $\delta = 90^\circ$ represents the ideally viscous case, where the material behaves as a Newtonian fluid. The tangent of δ is the ratio of viscous to elastic behavior and is commonly referred to as the loss factor. Fig. 2.2 depicts the phased stress-strain response of viscoelastic materials.

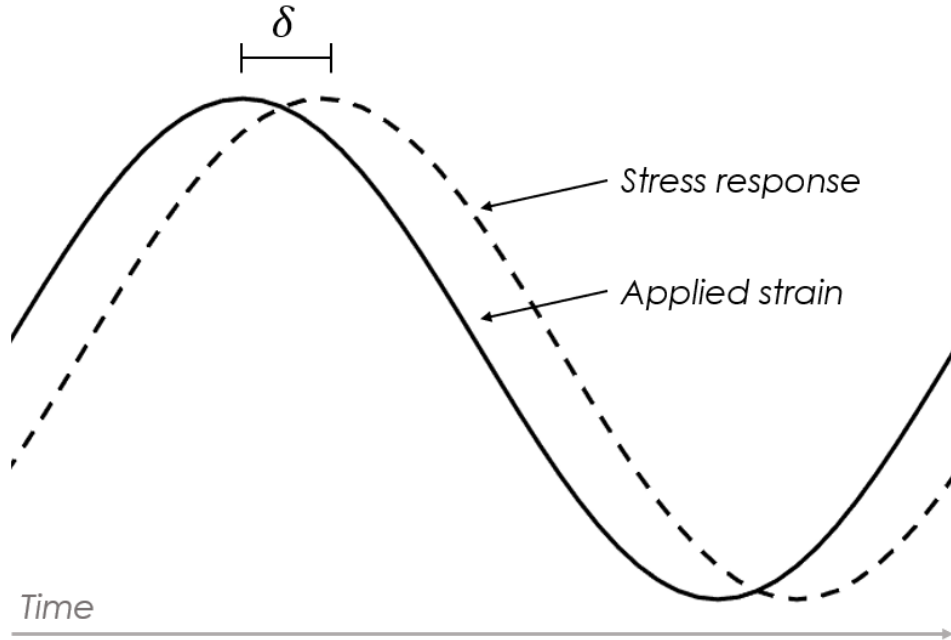


Fig. 2.2. Phased stress-strain behavior in oscillatory rheometry, and characteristic of viscoelastic materials.

The stress-strain behavior is quantified by the stiffness moduli corresponding to elastic behavior (the storage modulus, G'), viscous behavior (the loss modulus, G''), and the composite (the complex shear modulus, G^*), as defined in Eq. 2.5. The linear viscoelastic regime (LVER) is defined as the region in which the moduli are constant.

$$G^* = \frac{\tau}{\gamma} = G' + iG'' \quad (2.5)$$

Finally, oscillatory rheometry can also be used to quantify viscosity, though in a different form than traditional rotational rheometry—see Eq. 2.6.

$$\eta^* = \frac{\tau}{\dot{\gamma}} = \frac{G^*}{\omega} \quad (2.6)$$

Note that the viscosity is denoted with a * superscript and is referred to as the complex viscosity (analogous to the complex shear modulus) as opposed to the plastic viscosity from rotational

rheometry. The complex viscosity is further separated into its real and imaginary components, similarly to the stiffness moduli, as in Eq. 2.7.

$$\eta^* = \eta' + i\eta'' = \frac{G''}{\omega} + i\frac{G'}{\omega} \quad (2.7)$$

The benefits of oscillatory rheology to 3DCP lie in the ability to determine the extent of the LVER (so that it is known how many superseding layers the bottom layers may support while maintaining linear-elastic behavior) and to non-destructively probe stiffening behavior over time (to determine strengthening and open time) [22]. Fig. 2.3 shows G' and G'' as a function of shear strain. It can be observed that, for strains below a certain point, the properties are constant—this is the LVER. After a certain strain, the apparent stiffness decreases, identified as the yield point. This leads to the identification of a yield strain and yield stress, marked with a star in Fig. 2.4. Note that the yield stress is not necessarily the maximum stress, which practically correlates to the start of viscous flow.

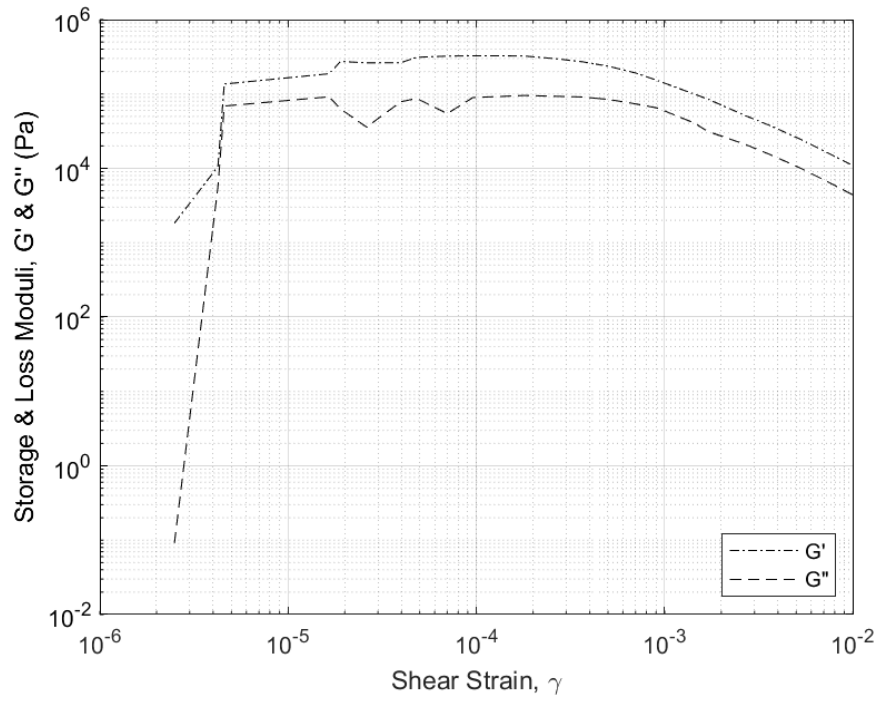


Fig. 2.3. Shear moduli in a sample subjected to logarithmically increasing strain.

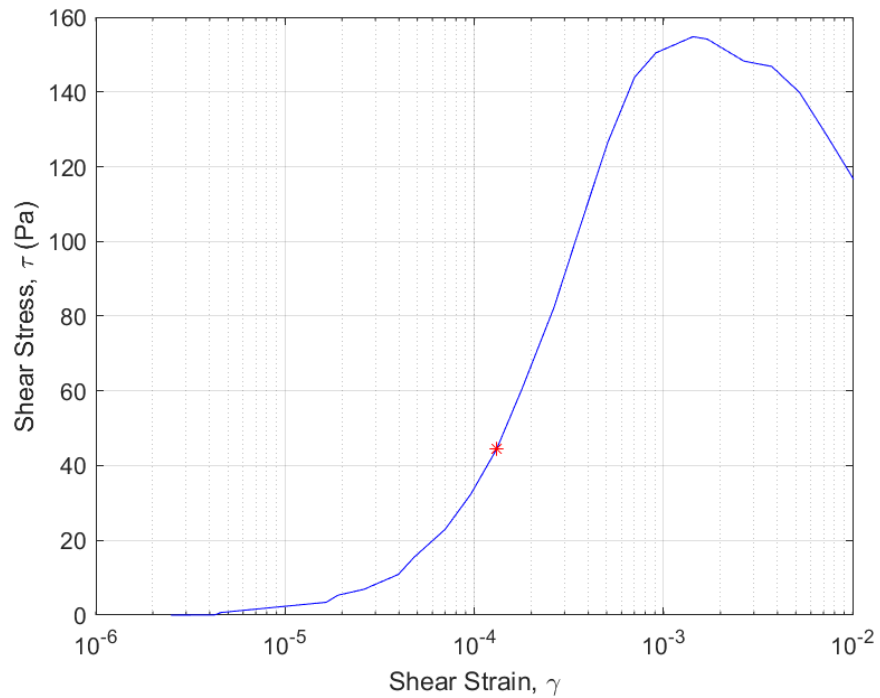


Fig. 2.4. Shear stress-strain curve of a cementitious sample in oscillatory rheology. The red star represents the yield point.

2.2.2.2. Measurement Artefacts

It is important to note that there are many ways in which rheometric testing may give results not truly representative of the material behavior. Most commonly, these include slippage of the material against the testing apparatus (often called wall slip), causing the material to not be strained fully, and shear-induced particle migration whereby larger particles move away from high-shear zones [20,21]. These artefacts are particularly relevant in highly dense suspensions, such as mixtures designed for 3DCP, as discussed further in the next section [12]. A full review on rheometry of cementitious systems is outside the scope of this paper, though the reader is referred to a recent report [20].

2.3. Mixture Design for 3DCP

2.3.1. Rheological Properties of 3DCP Mixtures

It is recognized that a key difficulty in design of mixtures for 3DCP lies in the competition between printability and buildability [23]. To have a material which is able to be pumped and extruded as a continuous filament (and able to be formed as a homogenous, fluid mixture at all), it must have relatively low viscosity. On the other hand, for a material must be strong enough to support its own weight immediately after deposition, and the weight of superseding layers within seconds or minutes, it must have a sufficiently high yield stress [23]. These two demands are often considered contradictory, and have not traditionally been required together. For example, SCC has low viscosity and yield stress for pumpability and self-flow, respectively, while dry cast or slipform concretes have high yield stress to reduce the need for formwork and high viscosity, in that they are typically harsh and grainy. Beyond the traditional Bingham parameters (viscosity and yield stress), 3DCP mixtures are known to have sufficiently high oscillatory rheometry shear moduli to minimize elastic deformation and susceptibility to buckling, while the stiffness should not be so high so that the filament is brittle and prone to tearing [24].

Furthermore, the structuration and setting of 3DCP mixes must be precisely controlled. This poses a second set of dueling requirements; the mixture must set quickly enough for rapid vertical construction, but not so rapid that cold joints form between layers [25–27]. Rheological characteristics for successful printing are further discussed in Section 2.4.

2.3.2. *Common Features of 3DCP Mixtures*

In order to achieve suitable rheology, 3DCP mixtures often contain some or all of the following features [6,7,9,28–37]:

- High paste content (often over 50% by volume).
- Small maximum aggregate size (on the order of a few mm).
- Somewhat low water-binder ratio (typically below 0.40), with large dosages of superplasticizers, viscosity modifying admixtures, set retarders and/or accelerators, and other chemical admixtures.
- Alternative cements such as calcium aluminate and calcium sulfoaluminate cements (for rapid set behavior).
- Fine particles (both aggregates and supplementary cementitious materials like fly ash and silica fume) to enhance particle packing, thixotropy, resistance to segregation, and other rheo-physical characteristics.

These ingredients are included to aid in printability and/or buildability. Importantly, it must be noted that 1K and 2K mixtures are often designed quite differently. 1K systems rely on extruding a mixture which is uniform and rigid due to particle flocculation and thixotropic buildup after pumping-induced shearing [13,38]. However, as the idea of 2K systems is to decouple demands of pumping and extrusion from vertical stacking (i.e., printability from buildability [39]),

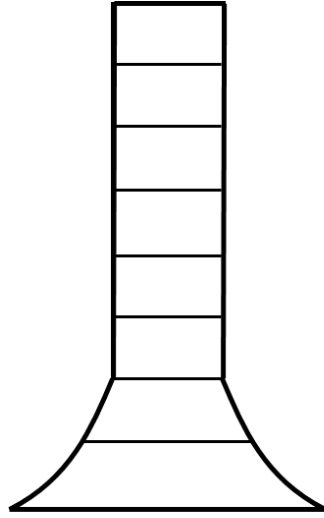
mixtures for 2K may resemble self-consolidating, highly flowable concrete for ease of pumping and uniform extrusion until it is deposited and injected with accelerant, and it stiffens rapidly. Chemically, these mixtures must be designed for the two components to result in rapid hardening once met, with any residual retardation effect in an individual component cancelled out or overcome. Such mixtures often rely on sulfate- or sulfoaluminate-based accelerators for setting by rapid precipitation of ettringite. By decoupling conflicting demands, 2K systems may be less sensitive to small material or environmental variations [40]. Additionally, further care must be taken in a 2K system to allow for proper extrusion while avoiding cold joints between layers [16,26]. A full review on 2K 3DCP design is outside the scope of this paper—the reader is referred to this recent review article [41].

2.4. Rheological Criteria for 3DCP

Fundamentally, rheology may be used as a physio-mechanical characterization method to understand the behavior of a viscoelastic system under stress and/or over time. In the context of design for 3DCP, it can determine the ability of a 3D-printed element to support its self-weight as it is constructed (i.e., as load is increasingly superimposed on a given layer, and simultaneously, as the material in that layer strengthens).

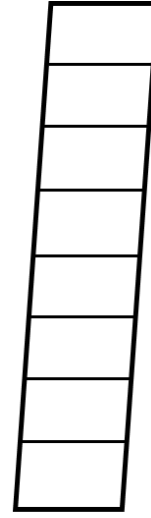
2.4.1. Criteria for Buildability

A designation of analytical, mechanical requirements for 3DCP structures in the fresh state was derived by Roussel in 2018 [42]. This article explores designing for resistance to plastic yielding (in which the material transitions from linear viscoelastic to viscoplastic/flowing behavior) and elastic buckling (i.e., stability-based failure), as depicted in Fig. 2.5.



PLASTIC YIELDING

- *Material failure*
- *Insufficient yield strength*



ELASTIC BUCKLING

- *Geometric stability failure*
- *Insufficient material stiffness*

Fig. 2.5. The two predominant failure modes during printing in 3DCP.

In this work, the integrity of a single layer under its own weight is scaled and generalized to describe criteria for an entire printed structure. The yield stress of a single layer of height, h , must be large enough to support its self-weight, as represented by Eq. 2.8.

$$\tau_0 > \rho gh \quad (2.8)$$

Where ρ is the material density and g is acceleration due to gravity. However, when applied to an entire structure, the failure mode will transition from shear (von Mises) failure to simple compressive failure [18,23]. As a structure is printed, the yield stress at all times must be sufficient to support the height at any given time, H —see Eq. 2.8.

$$\tau_0(t) > \frac{\rho g H(t)}{\sqrt{3}} \quad (2.8)$$

Notably, while the yield stress must increase linearly with increasing structural height, to prevent buckling failure, the Young's modulus should increase with the cube of height, as shown in Eq. 2.10 [18,27,42].

$$E(t) > \frac{3\rho g[H(t)]^3}{2b^2} \quad (2.10)$$

Where b is the width of the considered wall element. This presents a key contradiction, as stiffness does not necessarily evolve cubically with strength. In the literature, there are disagreements between the relationship between yield stress (or green strength) and elastic modulus at early ages. While some authors have theorized and observed a linear relationship between strength and stiffness over time [43,44], others note an unclear, nonlinear relationship between the two parameters [45,46]. This may be due to strength and stiffness being driven by some overlapping yet some distinct cement hydration mechanisms; while both properties evolve with increasing C-S-H interparticle bridging, yield stress will only be improved by long bridges which remain unbroken at high strain, and is further influenced by colloidal interactions in the paste system [45].

It is possible that the requirement for high yield stress, and especially for high Young's modulus, in the fresh state leads to structural overdesign for the hardened state; it has been argued that 2K systems may decouple the need for fresh strength from that of strength in service [47]. Of particular value would be a deeper understanding of the decoupled mechanisms controlling yield stress and stiffness evolution, so that fresh-state material design could consider each separately.

2.4.2. *Criteria for Printability*

A 3DCP mixture must be pumpable so that it is able to be delivered to the nozzle and extruded uniformly. For a concrete to be pumpable, it generally will form a lubrication layer [12,32,33,48], in which small particles (paste and some very fine aggregates) tend towards the walls of the hose; this is referred to as shear-induced particle migration (SIPM), and is depicted in Fig. 2.6 [49,50]. In the context of mixture design for pumpability, there must be sufficient paste content for a lubrication layer to form [32,51]. A mix with too high an aggregate content will not facilitate the formation of a lubrication layer and be prone to either paste-aggregate segregation or jamming and clogging [33,52,53]. Many concretes may also have an unsheared “plug zone” near the center of the pipe [54]. While composition of the plug and bulk zones are similar, their shear histories, and corresponding rheological behavior determined by thixotropy, will be different. Notably, Mohan et al. [33] found that plug flow did not occur in mixtures suited for 3DCP.

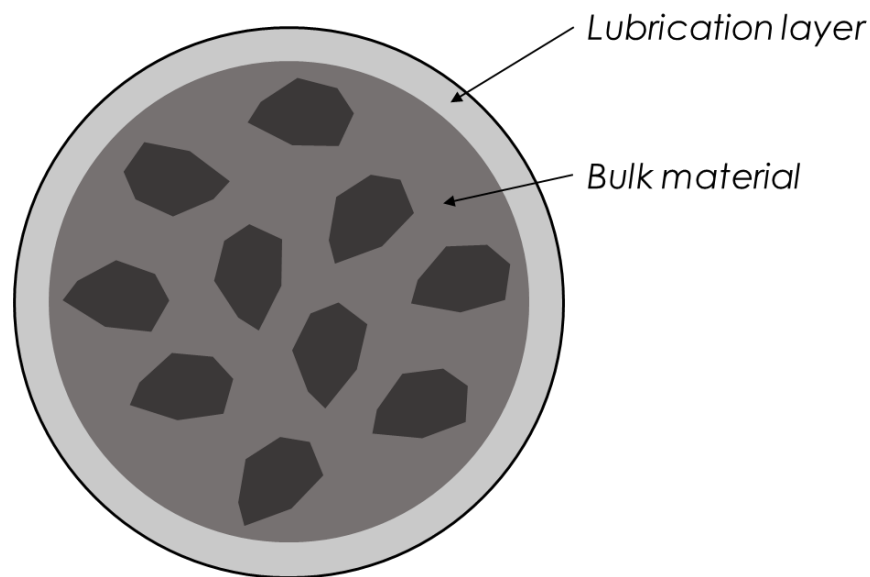


Fig. 2.6. A cross-section of hose during concrete pumping, exhibiting formation of a fines-rich lubrication layer due to shear-induced particle migration.

In terms of requirements, pumping pressure is proportional to both viscosity and yield stress of the lubrication layer [33,55]. Thus, to maintain pumpability without sacrificing buildability, viscosity should be reduced while maintaining yield stress as high as possible; as mentioned in Section 2.3.1, these requirements may be considered contradictory. Some mixture components which may reduce viscosity without dramatically reducing yield stress include spherical supplementary cementitious materials such as fly ash (to promote the ball-bearing effect of flow) and air entraining admixtures (in which entrained voids are deformable when pumping yet stabilize and increase yield stress during building) [32].

It is harder to quantify the rheological demands of the extrusion and deposition processes themselves. However, it is important to note that with a sufficiently fast speed of the print head, inertial effects may place tensile stresses on the material which can result in localized or complete fracturing (tearing) of the filament [42,56]. Some mixtures, even at slow print speeds, will not extrude continuously or uniformly. However, this may be due to poor pumpability, in that the material is poorly cohesive or prone to segregation.

2.4.3. Rheological Modeling

Some authors have used rheological properties to create models and simulations of the printing process. Kruger et al. [57] derived rheological requirements based on Mohr-Coulomb failure (discussed further in Section 2.5) with a conservative assumption of no inter-particle friction, reducing to the Tresca failure criterion. When this analytical model was compared to a finite element simulation, it was found that it significantly underpredicted the allowable height of a single layer for resistance to flow under self-weight. A second model by the same authors was over-predictive in estimating the point of plastic collapse (i.e., yielding) in a 3DCP structure [58]. The authors noted that the rheological testing had a very high variability, which increased

modeling uncertainty; high variance has also been observed in other rheological studies [59]. This may be due to high sensitivities to mixing procedure (influencing flocculation state and subsequent thixotropic recovery, air entrapment, etc.) and measurement artefacts (e.g., wall slip) [20]. Many more modeling studies have relied upon mechanistic analysis common in soil mechanics, as discussed further in the subsequent section.

2.5. Other Fresh-State Characterization Methods

2.5.1. Soil Mechanics Type Characterization

Wolfs et al. [60] proposed a macro-mechanical characterization methodology for fresh 3DCP materials which relies on tests common in soil mechanics and geotechnical engineering. This approach typically assumes the material to exhibit Mohr-Coulomb behavior, with pressure-dependent strengths and finite cohesion. The shear strength of a Mohr-Coulomb material is given in Eq. 2.11.

$$\tau = \sigma_n \tan \varphi + C \quad (2.11)$$

Where τ and σ_n are the shear strength and applied normal stress, respectively, and material properties φ and C are the angle of internal friction and cohesion, respectively. The properties are typically measured by combining information from an unconfined uniaxial compression test (ASTM D2166 [61]) and direct shear test (ASTM D3080 [62]), though a triaxial compression test (ASTM D2850 [63]) can also be used [64]. Furthermore, these tests can be completed at regular intervals to define temporal behavior of the material properties; it has been found that φ remains roughly constant while C increases linearly with time in the first ~ 90 minutes [60,65,66]. Notably, these tests must be repeated discretely and uniquely, whereas (oscillatory) rheometry can quantify setting continuously and non-destructively (i.e., on a single sample).

Suiker [67] and Suiker et al. [68] incorporated soil mechanics characterization into a model for constructing 3DCP walls. This mechanistic model aimed to predict the failure mode of a 3DCP wall (i.e., plastic yielding or elastic buckling) and the height of the wall at failure, as a function of compressive strength and elastic modulus with time. However, while failure mode was predicted well with these models, the height of failure was slightly underpredicted, leading to an overly conservative design. Other experiments have used Mohr-Coulomb (or the more general Drucker-Prager) failure criterion to estimate buildability of 3DCP with varying success [60,66,69,70]. In general, while these models tended to accurately predict the failure mode, the failure height was overpredicted, giving a non-conservative design (in contrast to the work of Suiker [67,68]). This may be because the testing was conducted on cast samples of the printable mixture and had some manual consolidation, rather than a printed mix which not only may be less consolidated but also will be anisotropic.

2.5.1.1. Shear Vane

A handheld shear vane, in contrast to an automated rheometer, was used by Le et al. [6] in one of the first works to design a concrete mixture for 3D printing, and has been used by other authors since [29,71]. The device is commonly used in geomechanics, but has similar working principles to rotational rheometry, in that a shear stress is applied onto a material to determine when it yields (viscosity may not be strictly measured here, as varying the shear rate across orders of magnitude is difficult by hand). A key benefit of the shear vane is that mortars are tested, not only pastes (as is common in traditional rheometry).

2.5.2. Other Mechanical Tests

Some authors have analyzed fresh 3DCP mixtures using a fracture mechanics framework [72,73]. These types of tests may not specifically give information on strength of the fresh material (and thus buildability) but rather quantify the end of the printability window (i.e., open time). Another test which relies on the fracture of the material at early ages is the “Slugs Test,” developed specifically for 3DCP [74]. The value of this test is that it is developed as an “in-line” quality control method meant for detecting information about the extruded material during printing and throughout the process; other in-line tests may be mechanical or quasi-mechanical in nature, though due to the fact that they measure material properties during printing, they are not used for the formulation and development of printable materials themselves [13,75].

2.5.3. *Non-Mechanical and Indirect Tests*

Many material tests exist to quantify fresh-state material characteristics that are not strictly mechanical in nature; such tests are often correlated to a certain mechanical property [13,18,39,53,65,76–78]. Prominently in 3DCP, these include:

- The ASTM C1437 mortar flow test [79]
- Ultrasonic pulse velocimetry
- Measuring resistance to penetration
- Calorimetry

It is critical to note that these tests indirectly measure mechanical properties. They may be most helpful for measuring the evolution of mechanical behavior with time, rather than providing an absolute quantification of printability or buildability. However, these measurements can be correlated to mechanical properties [80], and may be used to identify appropriate mixtures for a given printer, even if they cannot be considered universally applicable. Furthermore, while

“slow” penetration tests which measure continuous evolution of penetration resistance with time may help quantify strength, setting time tests like the Vicat test [81] may not correlate well with changes in rheology [82]. Stronger relationships may be observed between evolution of heat and rheological properties though hydration and microstructure formation are, in principle, distinct phenomena [78,83,84].

2.6. Applicability of Rheology to 3DCP

It has been established throughout this chapter that failure during 3DCP is largely governed by two modes: plastic collapse (due to yielding) and elastic buckling (due to instability). Thus, for a mechanical characterization method to be valuable, it must be able to capture one or both of the yield strength and Young’s modulus. This means that oscillatory rheology may be considered more valuable than rotational rheometry, as the shear modulus is calculated; the shear modulus is directly related to the Young’s modulus as shown in Eq. 2.12:

$$E = 2G(1 - \nu) \quad (2.12)$$

Importantly, this fundamental linear-elastic relationship concerns the shear modulus, G , not the complex shear modulus, G^* . G may be considered approximately equal to G^* , specifically calculated as the slope of the shear stress-strain curve with a forced zero-intercept, as in Moini et al. [24]. That work found G to have a stronger relationship to buildability than G' or G'' , or the yield stress or strain. However, as of the time of writing, no other works exist relating G to G^* ; it may be more valuable to use G' in Eq. 11 as this represents the elastic component of the modulus.

Zat et al. [85] found that significant deformation of printed elements occurred before yielding and collapse. This may be due to elastic deformation in part, but likely comprises some inelastic

creep [86,87]. It is also possible that partial yielding did occur in the lower layers. Critically, this large deformation was acceptable up to a certain threshold before failure. Moreover, this suggests that (inelastic) mechanisms not typically discerned from rotational or oscillatory rheometric testing may be relevant in determining buildability for 3DCP.

2.6.1. Paste-Scale to Mortar-Scale

As noted, rheometric characterization is often performed on a cementitious paste with no aggregate, though occasionally it is performed on a mortar. It has been established that at lower total aggregate volumes the behavior of the paste controls rheological behavior as hydrodynamic and colloidal interactions (in the paste) dominate over frictional interactions (between the aggregates) [88–90]. Additionally, as the aggregate is inert, the evolution of rheological properties over time is entirely dependent on the paste [91]. Thus, it may be appropriate to design the paste and aggregate components of a 3DCP mixture separately, as they affect the rheological behavior differently. Several studies have examined the effect of aggregate content on pumping and deposition specifically in the context of 3DCP; while the paste may have been designed by considering its rheology, a proper design of the overall mixture is a function of aggregate gradation and overall aggregate volume [32,33,52,53,92]. Thus, it may be of interest to quantify the rheological behavior of a mortar or concrete as a function of the constituent paste. The Krieger-Dougherty model [93] and the Chateau-Ovarlez-Trung model [94] (given in Eqs. 2.13 and 2.14, respectively) are commonly used to link the rheology of the constituent paste to that of the mortar or concrete by considering the volume fraction of aggregates, ϕ , and the random maximum packing fraction of aggregate, ϕ_m [33,95]. A particle packing approach can further be used to unify the design of the paste and aggregate components, though overly general assumptions may have to be made about particle shape and size distribution [96,97].

Additionally, the total particle distribution (aggregate and binder) can be designed to closely follow an empirically-optimized formulation, such as the Fuller-Thompson curve [35] or Andreasen and Andersen model [89,98].

$$\eta = \eta_{paste} \left(1 - \frac{\phi}{\phi_m}\right)^{k\phi_m} \quad (2.13)$$

$$\tau_0 = \tau_{0,paste} \sqrt{\frac{1 - \phi}{\left(1 - \frac{\phi}{\phi_m}\right)^{k\phi_m}}} \quad (2.14)$$

2.7. Discussion

It has been demonstrated throughout this review that there exist many methods to characterize 3D printable cement-based materials for process design and successful printing overall. The requirements for a 3DCP mixture, whether thought of mechanically or qualitatively, are stringent and sometimes in competition with one another. Engineers will require a comprehensive, universal, repeatable tool to formulate 3DCP mixtures and assure their quality.

Rheometry allows for the fundamental mechanical characterization of a fresh cementitious system and thus is a powerful tool for 3DCP. By allowing for the determination of strength and stiffness over time, it quantifies the ability to rapidly build tall, slender structures. Additionally, it informs users of the ability of the material to be successfully pumped and extruded. However, it may be considered an incomplete characterization as it often only tests the constituent paste; this is especially problematic if highly non-uniform, non-spherical aggregate is used, which can lead to widely varying effects on buildability [99]. This is where soil mechanics style testing presents value, as it tests on the complete composite material, not an individual phase. But, design for printing based only off soil mechanics testing (and associated failure criteria) has been highly

variable and not suitably accurate, perhaps due to variability in the printing process or the fact that these tests were performed on cast samples, which will not exhibit the same behavior as printed parts. Furthermore, such mechanical characterization treats the material as an elasto-plastic solid; ignoring the viscous contribution may be non-conservative [100].

An obvious alternative here is rheometry on the mortar or concrete, rather than the constituent paste. However, most benchtop rheometers cannot accommodate granularity larger than several hundred microns, nor do they have the ability to characterize materials as strong, stiff, or viscous as mortars and concretes. Rheometers designed for measurement on mortars or concretes are available, and pose a promising solution to the limitations of paste rheometry. However, common idealizations, such as modeling as a Bingham or Herschel-Bulkely fluid, may no longer be valid in the presence of large, inert, solid aggregate particles. In practice, the complexity of the rheological behavior of mortars and concretes, as well as the reduced sensitivity (due to the requirement of torque/rotation sensors to measure over an even greater range) and large size of mortar/concrete rheometers, may preclude their utility for mixture and process design. Such methods may be better suited to validation of the process (e.g., in-print quality control) than its fundamental design. Fortunately, as noted in Section 2.6, the behavior of the paste tends to dominate rheology of cementitious systems of low aggregate content (common in 3DCP), and paste will always drive temporal evolution of rheology.

Overall, this suggests that no one test is perfectly comprehensive in 3DCP process design. So, process design for 3DCP may rely on rheology, though not exclusively. Rheology provides a useful mechanical framework for understanding the viscoelastic behavior of fresh cementitious systems, though it may be incomplete in characterizing the whole composite material, and how it is affected by the printing process. For that, engineers must couple fundamental, laboratory-scale

characterization (for material development and formulation) with robust, site-scale quality assurance, whether that be through in-line mechanical testing or determining an empirical relationship between performance and an indirect test.

2.8. Conclusions and Future Work

This review has investigated the applicability of rheology to process design for 3D concrete printing. As this nascent construction technology has stringent and unique demands of the material in the fresh-state, rheology is demonstrated to be an effective method of mechanical characterization. However, combining rheometric testing with other techniques may provide a more comprehensive understanding of the material and its suitability for the 3DCP process. In particular, the following observations are made:

1. Rheological requirements for 3DCP may be dueling, and compromises have to be made between a highly flowable material for pumping and extrusion and a stiff, solid material for building.
2. Tests besides rheometry may provide complimentary information about the material, especially as it relates to quality assurance during printing. However, such tests are often not strictly mechanical, and thus cannot be considered an absolute physical metric, but a vehicle for characterization in the context of a specific printer system.
3. A characterization method which relies on preparing a cast sample may be prone to non-conservative process design, as the material is apparently stronger and stiffer than it is after printing.
4. Use of a two-component (2K) printing system may reduce contradictory rheological criteria for printability and buildability and may yield a more robust, less variable

process. However, care must be taken to not induce cold joints or filament discontinuities.

To further progress 3DCP construction by understanding the fundamental mechanical demands of the process, further work may involve determining the relevance of different deformation modes (i.e., elastic, plastic, inelastic creep) on printed object performance, relating soil mechanics testing to rheometry to elucidate their combined beneficial potential for material characterization, and relation of indirect tests to mechanical properties and behaviors.

CHAPTER 3. INVESTIGATION OF MICROSTRUCTURAL AND MACROPHYSICAL ANISOTROPY IN STEEL-FIBER-REINFORCED 3D-PRINTED CEMENTITIOUS COMPOSITE

Abstract

The action of extrusion creates an anisotropic microstructure in 3D concrete printing, which in turn leads to anisotropic physical properties. This contrasts with conventional, cast concrete which features a randomly oriented microstructure and thus largely isotropic behavior. While an anisotropic pore system can negatively affect mechanical performance and durability, preferentially aligned fiber reinforcement may enhance strength and ductility. This study investigates the anisotropic microstructure (including fiber alignment) and physical behavior of a 3D-printed cementitious composite as compared to a cast counterpart. It is found that the printed system exhibits greater fiber alignment, greater sorptivity, and decreased flexural stiffness as compared to the cast version.

3.1. Introduction

3D concrete printing (3DCP) has obvious, macro-scale differences when compared to cast concrete. These include the presence of layers and the ability of the material to hold its form immediately upon deposition. However, a comprehensive understanding of the microscopic differences between 3DCP and cast concrete is essential to establish a robust relationship between material composition and in-service behavior. Specifically, the 3D printing process leads to directional alignment of voids [101–107] and oblong particles, like reinforcing fibers [108–110]. This process-induced anisotropy leads to directionally dependent mechanical

performance [111–116]. Additionally, the traits of the microstructure control the ingress and transport of deleterious agents, and thus the system’s durability [117,118].

In general, 3DCP elements exhibit a larger average void size and greater quantity of “very large” voids on the millimeter scale. The voids are often more interconnected, though the overall bulk porosity is often similar to that of cast specimens [101–107]. While mechanical anisotropy of 3DCP systems has been well established [111–116], and several authors have studied their durability [98,103,106,115,119–121], the quantitative link between microstructural anisotropy and heterogeneity and macrophysical behavior is less defined. Moreover, the contribution of fibers to mechanical and durability behavior is of great interest as the reinforcement of 3DCP structures with conventional rebar is difficult due to geometric irregularities [10,122]; the orientation of fibers is expected to play a significant role, as in other fiber-reinforced concrete applications [123,124].

This study aims to establish a preliminary understanding for 3DCP with rigid reinforcing fibers, accounting for anisotropy, fiber alignment, and mechanical deficiencies. Thus, three characterization techniques were selected: flexural testing, sorptivity testing, and computed microtomography (μ CT). The two testing techniques elucidate the microstructure’s effect on mechanical behavior and transport properties, while μ CT allows for qualitative and quantitative characterization of the microstructure. Overall, this experiment will allow researchers and practitioners to understand qualities of 3DCP which correspond to mechanical strength, ductility, and durability.

3.2. Experiment

A calcined clay-based cementitious composite was printed and cast into beams for this experiment. The material was reinforced with Dramix straight steel fibers with length of 13 mm and diameter of 0.18 mm at 0.25% by volume.

The mixture materials and design proportions are listed in Table 3.1, though superplasticizer and water were varied slightly depending on ambient conditions and observations throughout printing. The binder was developed as a low-strength, sustainable material for housing applications [125]. Commercially available Type I/II portland cement (Quikrete) and metakaolin (BASF) were used as cementitious materials. The superplasticizer was a commercially available polycarboxylate-based suspension with a solids content of 36% (MasterGlenium 7920, Master Builders). As this experiment did not involve printing of tall structures or at high vertical construction rates, the material’s long set time allowed for a longer mixing process to properly disperse fibers. The aggregate was a natural concrete sand (specific gravity 2.6, absorption capacity 2%) which was sieved to comply with constraints of the printing system—a maximum aggregate size corresponding to the standard #16 sieve (1.18 mm) was selected. The aggregate gradation is shown in Fig. 3.1.

Table 3.1. Mixture design of the printed material, normalized by weight of portland cement.

Material	Normalized Weight
Portland Cement	1.00
Metakaolin	2.25
Water	3.31
Sand	4.50
Superplasticizer	0.007
Steel Fiber	0.18

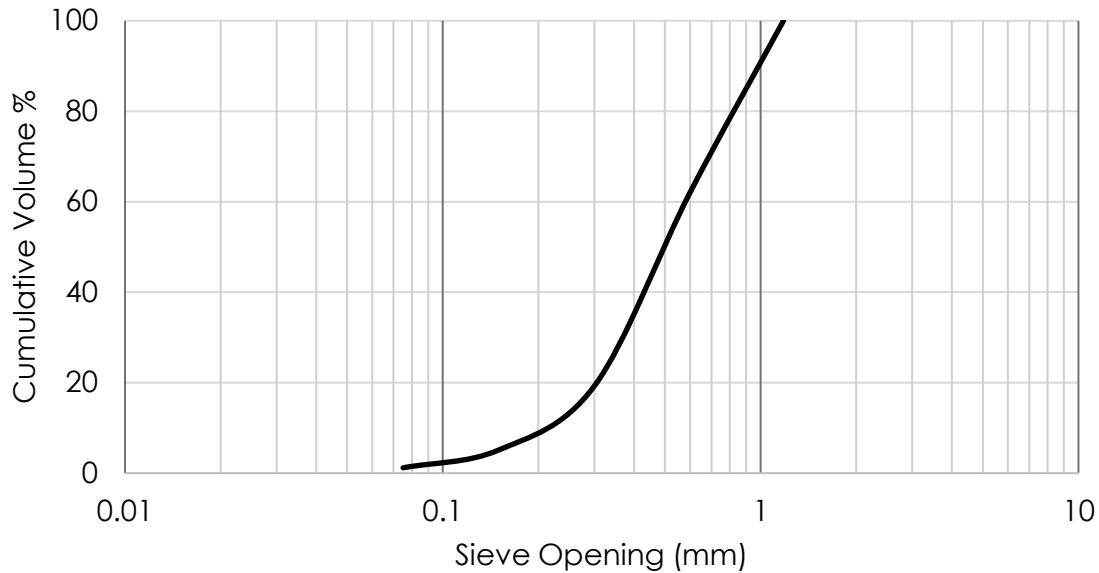


Fig. 3.1. Gradation of aggregate used in printing material.

The printing process involved the fabrication of beam specimens, to be compared to cast counterparts. A 30 mm nozzle with 15 mm layer height was selected to print beams with a nominal size of 120x120x360 mm, compared against 100x100x350 mm cast samples. While the size of the cast beams aligned with ASTM C1609 [126], the printed beam nominal dimensions were selected for compliance with the nozzle size.

The beams were tested in four-point bending in accordance with ASTM C1609 to determine differences in strength and stiffness between the printed and cast samples, and to examine the effect of fiber entrainment. An MTS universal testing machine with 67-kip capacity was paired with an Epsilon Technology Corp deflectometer to measure midspan deflection during testing—see Fig. 3.2.

After flexural testing, core samples were extracted from the cast and printed beams—near the edge of the specimen and within its bulk—for observation by computed microtomography (μ CT) and for sorptivity testing. Care was taken to extract the cores away from mechanically damaged

regions in order to not artificially increase local porosity. The cylindrical samples measured approximately 50 mm in diameter by 50 mm tall.

In total, eight specimens were tested for sorptivity: two each for the printed and cast samples, near the edge and in the bulk. Two samples were selected for qualitative analysis by μ CT imaging: one from the printed beams and one from the cast beams, each near the edge. The sorptivity test consisted of measuring absorbed mass of 0.6M potassium iodide (KI) solution with respect to time using a modified ASTM C1585 [127] procedure. KI was utilized instead of water so that it could be seen during μ CT scanning; the concentration was determined by Moradllo et al. [128] to be suitable for tracing by x-ray.

During sorptivity testing, core samples were sealed on the sides and placed in a bin, elevated from the bottom surface and with solution coming approximately 1 mm up the side, as shown in Fig. 3.3. The mass change of the specimens following one-sided exposure to solution was recorded at the following times: 1 min, 5 min, 10 min, 20 min, 30 min, 1 hour, 2 hours, 3 hours, 4 hours, 5 hours, 6 hours, 24 hours, and 48 hours.



Fig. 3.2. Flexural testing of printed beam specimens.



Fig. 3.3. Sorptivity testing of cores from printed and cast beam specimens.

A Scanco uCT50 unit was utilized for μ CT imaging. Table 3.2 contains the settings selected for the μ CT scanning, and the resulting resolution. Segmentation and image rendering were completed with the commercial x-ray analysis software Dragonfly, with threshold intensity values selected for segmentation of the fibers, voids, and the mortar matrix. μ CT was conducted on the same sample before and after sorptivity testing with the goal of visually observing the pattern of fluid ingress.

Table 3.2. Selected settings and resulting resolution (voxel size) for μ CT scanning.

Setting	Value
Energy	90 kV
Intensity	155 μ A
Integration Time	1200 ms
Filter	0.5 mm Al
Field of View	35.2 mm
Voxel Size	34.4 μ m

3.3. Results

3.3.1. Flexural Testing

Three printed beams (labeled P-I, P-II, and P-III) were tested alongside two cast counterparts (labeled C-I and C-II) in order to determine differences in their behaviors. The cast beams were prepared from the same mixture and consolidated manually. The stress-deflection curve is shown in Fig. 3.4 rather than a load-deflection curve to normalize geometric inconsistencies in the printed beams. As shown in Fig. 3.4, all beams exhibited similar flexural strengths, though the printed beams exhibited approximately 52-79% decreased stiffness when compared to the cast specimens. This shows that, in addition to being more compliant, the mechanical response of the printed beams was more variable, while both cast specimens exhibited similar bending stiffnesses.

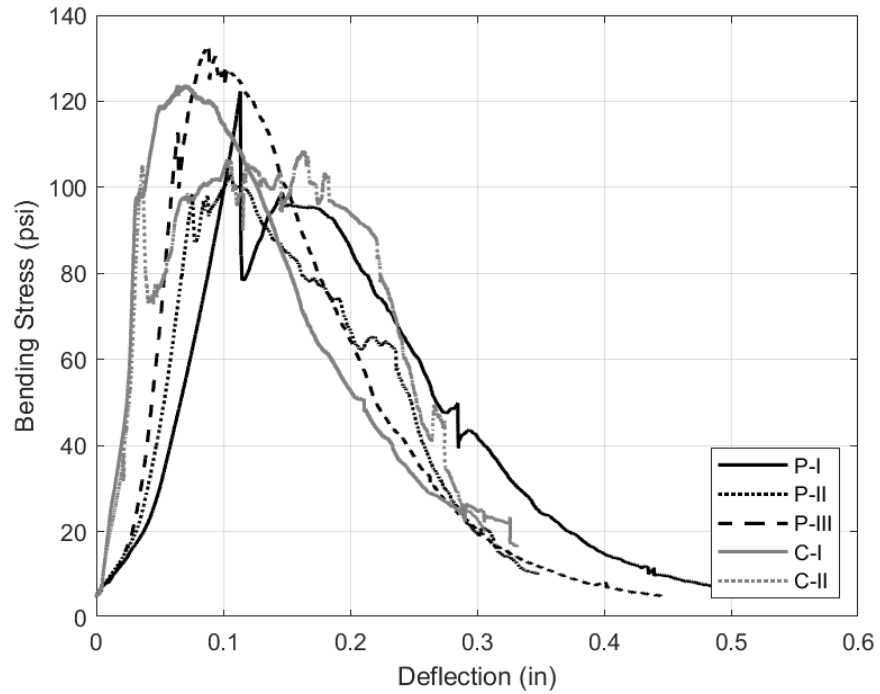


Fig. 3.4. Stress-deflection curves of flexural testing of printed and cast beams

Notably, all beams showed significant post-peak ductility, remaining intact at deflections over 3x greater than at peak stress, even at a relatively low dosage of fibers. This demonstrates that even a small dosage of fibers can provide ductility to the quasi-brittle cementitious material.

3.3.2. Sorptivity Testing

By recording the mass change of the specimens and knowing the area of the cores and density of solution (1.1 g/mL), the absorption can be measured. Table 3.3 contains the final absorption of the specimens and percentage mass absorbed, and Fig. 3.5 displays the progress of absorption with respect to the square root of time.

Table 3.3. Absorption and total absorbed mass after 48 hours.

Sample ID	PE-I	PE-II	PB-I	PB-II	CE-I	CE-II	CB-I	CB-II
Sample Type	Printed, Edge	Printed, Edge	Printed, Bulk	Printed, Bulk	Cast, Edge	Cast, Edge	Cast, Bulk	Cast, Bulk
Absorption at 48 hr. (mm)	15.8	13.5	13.9	15.6	17.3	17.1	14.9	15.9
Percent Mass Absorbed	23.8	24.7	22.8	22.8	25.6	26.0	25.7	25.4

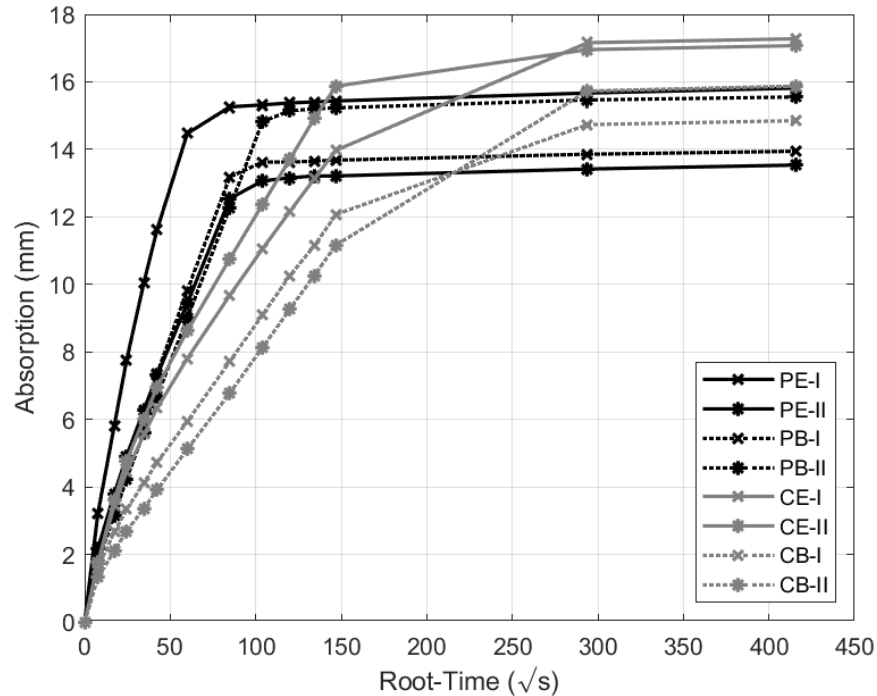


Fig. 3.5. Sorptivity test curve, with printed and cast samples from the edge and bulk regions exposed to solution and monitored for 48 hours. Plotting absorption against the square root of time follows the ASTM C1585 convention.

The data exhibit that printed specimens (in black) had a 61% higher average initial rate of absorption, while cast specimens (in gray) had lower initial sorptivity but continued to absorb solution longer than the printed specimens did; on average, the cast specimens had an 11% higher absorption capacity (by mass absorbed) than the printed specimens. Finally, the samples extracted from near the edge of the beams (solid lines) had 35% higher average initial sorptivity than those from the bulk (dashed lines), though the final absorption capacities between samples

from the two regions are similar, at 15.9 and 15.1 mm average absorption in the edge and bulk regions, respectively.

A higher initial sorptivity suggests greater void interconnectivity (due to the ease with which the testing fluid travels through the specimen), which is known to lead to enhanced transport of outside substances within the concrete's microstructure. This can adversely affect durability, as deleterious agents can more easily enter the concrete and lead to physicochemical degradation. While their higher initial sorptivity suggests that printed specimens may be more prone to degradation reactions, the larger absorption capacity of cast samples may promote higher total loading of deleterious agents, and a potential competing mechanism for overall durability.

3.3.3. Microstructure Quantification via μ CT

By using μ CT, the void aspect ratio distribution, void size distribution, and fiber alignment distribution may be quantified, while the volume of pores and fibers can be computed. In the images from before sorptivity testing, sand and paste may be separated, but in the images from after sorptivity testing, diffusion of the KI solution made segmentation of the individual matrix components impossible. This is likely due to high capillary porosity in the system (due to the high water-binder ratio of the mixture), which allowed for full saturation of the samples after only 48 hours of sorptivity testing.

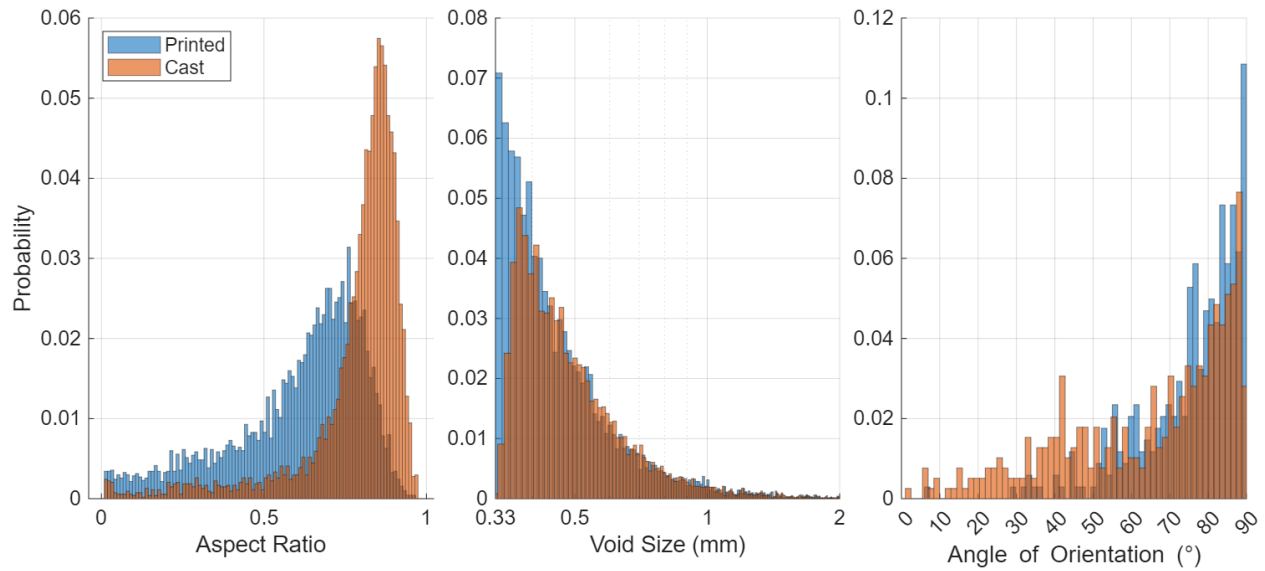


Fig. 3.6. Distributions of void aspect ratio, void size, and fiber alignment of printed and cast samples. An aspect ratio of 1 is a perfect sphere, and an angle of 90° corresponds to the printing direction.

Distributions of void aspect ratio, void size, and fiber alignment are shown in Fig. 3.6. An aspect ratio of 1 corresponds to a perfect sphere, while 0 is a completely flat, planar void. The mean void aspect ratios were 0.61 and 0.79, and the median void aspect ratios were 0.66 and 0.83, for the printed and cast systems, respectively. The aspect ratio distribution is notably left-skewed in both printed and cast specimens, demonstrating that voids tend towards perfectly spherical. However, the printed system shows more voids at lower aspect ratios (i.e., irregular in shape). Additionally, the distribution of the cast system has a much higher peak, representing a higher concentration of more spherical voids. This contrasts with the printed system, which has a flatter distribution and thus a wider array of varying morphologies.

The μ CT analysis aligns with other research that has found that printed systems may have similar, but slightly higher total porosity than cast [101]. In this experiment, the porosities of the printed and cast systems were 2.20% and 1.93%, respectively. The void size distribution of the printed and cast systems are largely similar, with both showing a high concentration of voids near 0.33 mm (corresponding to the resolving power of the μ CT) and minimal voids above 1

mm. However, it is shown that the printed system has many voids smaller than about 0.37 mm, while the printed system's distribution shows a peak at that size. This may be due to differences in the consolidation of the material provided by the extrusion pressure (in the printed system) as opposed to manual consolidation (in the cast system).

The fiber alignment distribution shows that in both systems, fibers tended to align in the longitudinal direction (i.e., the printing direction), corresponding to 90°. However, the printed system exhibited greater alignment overall; the mean fiber orientations were 75.5° and 64.6°, and the median fiber orientations were 79.1° and 72.1°, in the printed and cast systems, respectively. Additionally, the cast system showed many more poorly aligned fibers (closer to 0°) whereas in the printed system, virtually all fibers exhibited some degree of alignment.

3.4. Discussion

Quantitative distributions of material features obtained by μ CT are supplemented by qualitative image analysis of the printed specimen. Fig. 3.7 shows that the larger voids are more likely to have a low aspect ratio, while the small voids are more spherical. These large voids may represent poor consolidation provided by the extrusion process, or smearing as the nozzle drags along the printed filament. Contrastingly, the relative sphericity of the small voids implies that they are intrinsic to the material system and formed during the mixing process.

Additionally, the micrograph of the void system does not clearly show the interlayer region. This may be due to the short pass time in printing, mitigating drying damage [107,111,129]. However, this suggests that the observed differences in pore size and aspect ratio are not controlled by the interlayer region only.

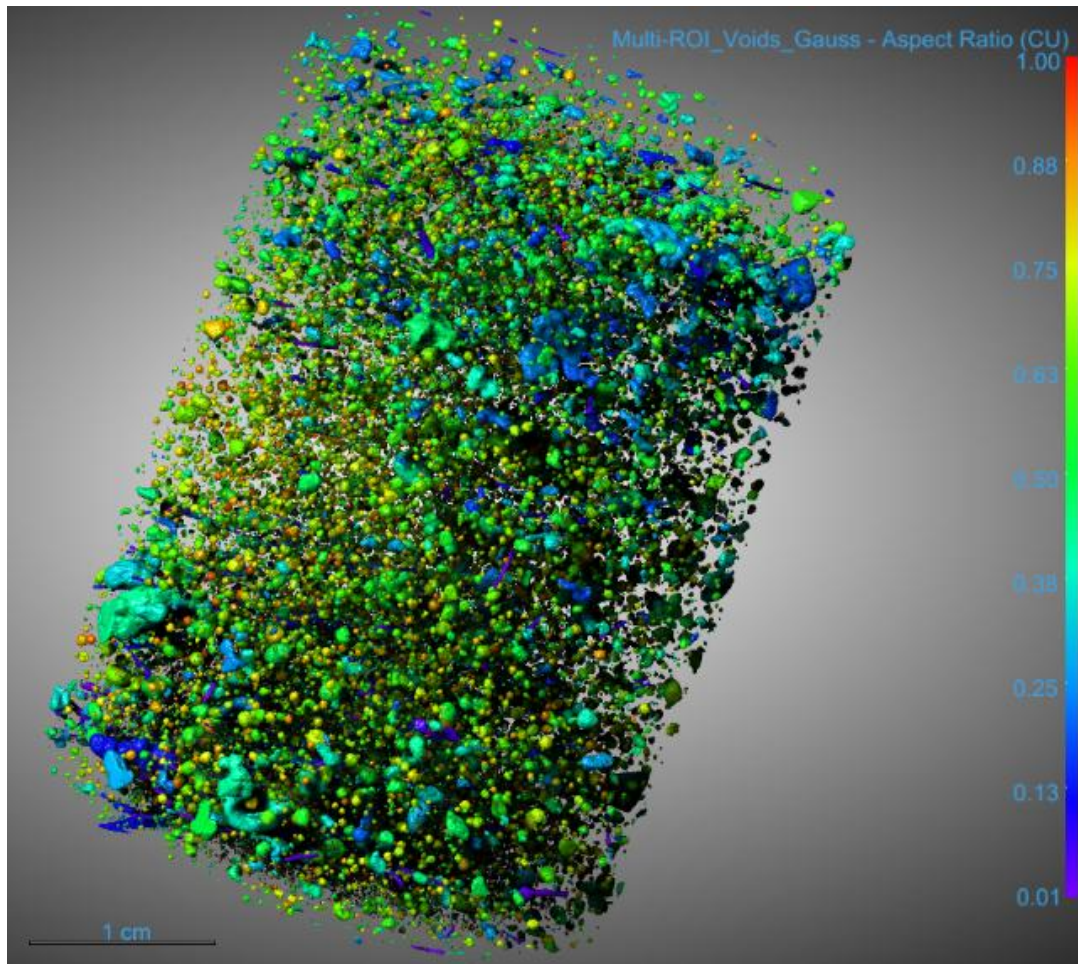


Fig. 3.7. μ CT image of voids in the printed sample, colored by aspect ratio (1 = perfectly spherical). A qualitative analysis of images of fibers in the printed sample corroborates quantitative insights from the distribution, where fibers appear to be preferentially oriented. Fig. 3.8 also shows that fibers are grouped together in regions corresponding to layers. Fibers are almost entirely absent from the interlayer region, and they appear especially well-aligned in the layer interior. This demonstrates that the fibers migrate to the center of the extruded filament when they align, which can be interpreted as a form of shear-induced particle migration (SIPM), in which the pumping process causes the coarser particles of the suspension to the center of the pipe [49,50]. This corroborates the work of Kolawole et al. [26], who found that material heterogeneity in the filament (from SIPM) contributed to mechanical anisotropy in the printed element.

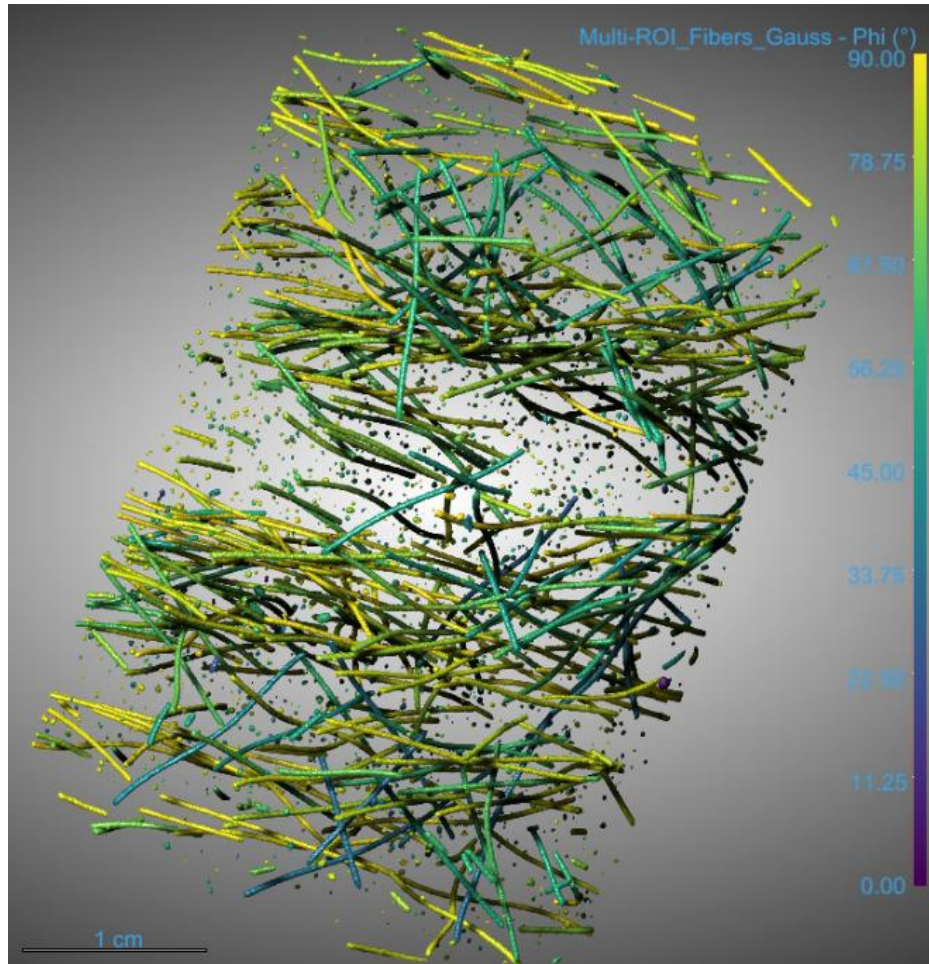


Fig. 3.8. μ CT image of fibers in the printed sample, colored by orientation (90° = longitudinal, i.e., printing direction).

Observations of the microstructure may help to explain the response of the different systems during flexural and sorptivity testing. The printed beams were up to 79% less stiff in flexure than those cast. While the modulus of elasticity is most commonly measured in compression, this agrees with general findings that printed specimens were less stiff than those cast [130,131]. Notably, ultimate flexural strength values were similar for printed and cast specimens. The similarity in strength yet discrepancy in stiffness may be due to void alignment and coalescence in the printed sample, effectively reducing the sectional bending rigidity. In a recent multi-laboratory study on the mechanical behavior of 3DCP [132], the flexural strength in printed and

cast specimens was similar when the bending axis aligned with the print direction, as in this research.

Sorptivity measurements allow for quantification of the transport properties of the material. A concrete which more readily sorbs fluid may experience greater exposure to aqueous, ionic species which can cause degradation, and is also prone to (partial or total) saturation and subsequent damage through freezing and thawing. Sorptivity can thus be seen as a proxy for determining the material durability [133]. It is observed that the initial sorptivity (slope of the line in Fig. 3.5) is greater in all printed specimens than those cast. This initial sorptivity is governed by capillary suction, and results in rapid ingress of water into the specimen [134], while the continued sorption of fluid after the capillaries are saturated is controlled by dissolution into small gel pores [135]. Therefore, the irregularly shaped voids in the printed specimen contribute to a better-connected microstructure, facilitating ease of initial sorption. Contrastingly, the total absorbed fluid was generally greater in the cast specimens at 48 hours. This can be explained by considering that the total mass absorbed by all cast specimens was similar, while for those printed, specimens extracted from the edge absorbed more than those from the bulk. This may be due to saturation near the edge of the specimen, forcing additional water to enter the printed sample through the slower mechanism of dissolution, rather than capillary suction, while no such barrier existed in the cast sample.

3.5. Conclusions

This work investigated the microstructure of a 3D-printed, fiber-reinforced cementitious composite, compared it to a cast counterpart, and related these observations to macro-scale physical phenomena. The following conclusions are drawn from the results:

1. While the printed and cast specimens had similar overall bulk porosities, the printed version showed a greater concentration of irregularly shaped voids of low aspect ratio, and of small voids near the resolving power of the μ CT. Both systems exhibited some alignment of fibers to the horizontal. However, the printed system exhibited greater alignment.
2. The printed specimens were up to 79% less stiff in bending than those cast, though they had similar strengths. This decreased stiffness may be due to irregularly shaped voids (and the presence of interlayers) in the printed specimen, which effectively reduce the sectional (geometric) stiffness.
3. Sorptivity testing reveals that the printed specimens allow for easier initial ingress of fluid into the microstructure, especially near the specimen edge. However, cast specimens tend to have a greater absorption capacity overall. These results demonstrate the ease with which the printed specimens are saturated, though the total fluid ingress is greater in cast specimens. These contrasting findings may affect the durability of printed and cast specimens differently.

CHAPTER 4. EVALUATION OF MACHINE-LEARNED OSCILLATORY RHEOLOGY TO DESIGN BLENDED CEMENT SYSTEMS FOR 3D PRINTING

Abstract

For successful construction, 3D concrete printing (3DCP) demands carefully tailored fresh-state properties to balance pumpability, extrudability and buildability. In this work, machine learning was applied to predict testability and printability of limestone – calcined clay cement (LC3) mixtures; testability was defined as the ability to form a homogenous mixture while printability represented the quality of the 3DCP forms. We hypothesized that printability could be modeled as a function of storage modulus, viscosity, flow onset stress, and open time, and we generated a dataset of 54 LC3 mixtures with water-binder ratio of 0.30-0.45, metakaolin fraction up to 30% by weight, and polycarboxylate superplasticizer dosage up to 0.4% by weight of binder to explore the dependence of composition on rheology. From such data, a hierarchical machine learning framework utilizing domain knowledge was generated to classify testability and predict mixtures with optimal rheology for printing. Such mixtures had a water-binder ratio of 0.30-0.34 with either high metakaolin and superplasticizer content (21-30% and 0.35-0.37%, respectively) or low metakaolin and superplasticizer content (6-12% and 0.17-0.18%, respectively). A low metakaolin – low superplasticizer mortar was printed but exhibited filament tearing, while a high metakaolin – high superplasticizer mortar exhibited pronounced shear thickening, preventing extrusion. We conclude that the disconnect between testability and printability lies in the relatively low shear rates accessed in oscillatory rheology and that truly predictive models will require material parameters acquired under conditions representative of pumping and extrusion, but that machine learning is capable of modeling the interplay of composition and properties which undergird 3DCP.

4.1. Introduction

Additive manufacturing via 3D concrete printing (3DCP) is an emerging construction technology that employs the robotic, automated deposition of a cementitious material in layers to create a free-formed structure without the use of formwork [3]. The 3DCP construction process requires that the fresh material exhibit sufficient pumpability, extrudability, and buildability while having a carefully controlled open time [23]. These demands are often conflicting. Specifically, the material must exhibit appropriate viscous flow for the entire pumping sequence and to ensure homogenous extrusion. Then, after some residence time in the printing system, the material is deposited, and it must hold its shape immediately and gain elastic strength and stiffness rapidly enough to support the weight of subsequently deposited layers [136,137]. As the fresh-state material requirements involve both viscous and elastic behavior, the mixture design process can be thought of in a rheological framework [18,42]. Oscillatory rheometry can be used to obtain deconvoluted quantification of both viscosity and elasticity [138], including continuous tracking of temporal evolution of the same sample [139,140]. This allows for the characterization of extrusion behavior, buildability, and temporal evolution thereof within the same experimental framework.

This work utilized machine learning to explore a large space of material behavior while reducing the need for physical experimentation. In particular, hierarchical machine learning (HML) allowed for reliable, generalizable predictions based on small datasets by incorporating relevant physicochemical information (domain knowledge) into the model learning process [141]. The incorporation of domain knowledge has been demonstrated to be beneficial for applications concerning cementitious systems [142,143].

Furthermore, limestone – calcined clay cements (LC3) were utilized to reduce the clinker fraction by substituting widely abundant materials but more minimally processed materials [8]. Workability has been identified as one of the key barriers to the widespread adoption of LC3s [144–147]. However, the rheological attributes of LC3s—including increased yield stress and thixotropy [148–151]—can be beneficial for 3DCP [9,97,152–154]. The objective of this research was to evaluate the ability of HML-predicted rheological behavior to design printable LC3s. Previous studies have either applied oscillatory rheometry to 3DCP mixtures [24,33,40,51,69,78,83] or used machine learning to predict rheological parameters [155,156]. However, there has been no research that translates oscillatory rheology into mixture design via machine learning. To the authors’ knowledge, this is the first study aimed at creating such a framework.

Because rheometry is highly sensitive and often exhibits poor inter-laboratory repeatability [20], this study prioritized a controlled, in-house experimental dataset over a larger but inherently noisy compilation from the literature. By using a single operator, consistent material sources, and identical equipment throughout, the present dataset minimizes variability from extraneous factors. Moreover, pastes were examined using a high-resolution benchtop rheometer which lacks the torque capacity required for mortars under the hypothesis that, at a fixed aggregate volume fraction, variations in paste rheology govern the behavior of the corresponding mortars [88]. The resulting set of 54 mixtures—modest in size but well suited to HML—was characterized by completing both amplitude and time sweep oscillatory rheometry tests on LC3 pastes with a water-binder mass ratio (w/b) of 0.30-0.45, metakaolin fraction up to 30% by weight, and superplasticizer dosage up to 0.4% by weight of binder. Appropriate rheological parameters relating to printing success and relevant domain knowledge were established from

theory and from the literature. A decision boundary was created to predict whether a mixture would form a homogenous paste upon mixing and be able to be tested. Finally, candidate mixture designs were identified through a multi-objective optimization procedure, used to create printable mortar, and validated by printing. Overall, this work established a framework for 3DCP mixture design in which HML served to create linkages between material formulation, rheological behavior, and printing performance.

4.2. Background

4.2.1. *Oscillatory Rheology of Cement-Based Materials*

Oscillatory rheology allows for differentiation between viscous and elastic behavior by examining the phase shift between an applied strain and the stress response, or vice versa. In this research, two oscillatory rheology tests are conducted. An amplitude sweep subjects the sample to increasing strain amplitude over a short time, allowing effects of early hydration to be neglected, while a time sweep imposes a constant, small strain amplitude over an extended period of time to determine temporal evolution of rheological behavior without destroying the microstructure.

In the amplitude sweep, up to a certain applied strain amplitude, the stress response is linear—this is the linear viscoelastic regime (LVER). Within the LVER, the relationship between stress and strain is defined by the complex shear modulus, G^* , as in Eq. 4.1.

$$G^* = \frac{\tau}{\gamma} = G' + iG'' \quad (4.1)$$

The complex shear modulus can be separated into real, in-phase (elastic) and imaginary, out-of-phase (viscous) components: the storage modulus G' and loss modulus G'' , respectively. A

similar relation exists to define the complex viscosity η^* (relating stress to shear rate) within the LVER, given applied rotational frequency ω in rad/s, as in Eq. 4.2.

$$\eta^* = \frac{\tau}{\dot{\gamma}} = \frac{G^*}{\omega} = \eta' + i\eta'' = \frac{G''}{\omega} + i \frac{G'}{\omega} \quad (4.2)$$

The end of the LVER is determined as the point at which the above properties are no longer constant with increasing strain. Physically, this reflects the point at which the evolving particle-hydrate network can no longer maintain its structure under increasing strain, marking the yield point [45,157,158]. In some complex fluids, including cementitious suspensions, the structure continues to resist shear, although it progressively loses stiffness [157]. After reaching a peak stress, the percolated microstructure breaks down, the system can no longer sustain significant stress, and macroscopic flow begins [138,157,159]. Therefore, the point of maximum stress is defined as the flow point.

In the time sweep, stiffening behavior of the system can be quantified and related to workability. Mostafa and Yahia [160,161] defined a “percolation threshold” time at which the phase angle δ stops decreasing substantially, indicating that the viscous component of the material response has reached a minimum. Some authors have examined the time of the “crossover point” at which $\delta = \pi/4$ (i.e., the viscous and elastic components are equal) [162] while other authors consistently see $G' \gg G''$ and thus observe no crossover point [51,139].

This research observed no crossover point and found highly noisy values for δ . This variability likely results from the heterogeneous and rapidly evolving microstructure of fresh cementitious suspensions, combined with sensitivity of δ to small stresses and instrument limitations. Thus, the end of the workable period was defined as the time at which G' reaches some critical value, as G' consistently increases during the induction period of cement hydration and provides a more

robust measure of structural evolution [163,164]. However, once the mixture reaches a system-dependent critical stiffness, it may either hinder pumping or compromise extrudability.

4.2.2. HML Modeling

HML provides a method of integrating domain knowledge which is particularly useful for materials informatics problems [141]. Rather than predicting the response directly from compositional input variables, HML incorporates a “middle layer” of features known to quantitatively describe the physicochemical nature of the modeled system; in this experiment, the middle layer connects microstructural attributes to macroscopic rheological response, improving generalizability (prediction on unseen data) and model convergence on small datasets. This approach has been applied to the design of cementitious systems [143,165–168] and additive manufacturing [169,170], though not previously for 3DCP.

The inputs to the model were raw compositional variables commonly used for the design of cementitious systems. They were the water-to-binder mass ratio (w/b), substitution of metakaolin for cement, and dosage of superplasticizer by weight of binder. The identification of middle layer features was based on observations of the dataset and is given in Section 4.4.2.1.

To fully characterize the material response—stiffness, viscosity, strength, and rate of structuration—the following properties were measured to quantify print performance:

- G' , the storage modulus, should be maximized to improve buildability [24,27,42,136].
- η' , the real component of material viscosity, should be minimized to improve extrudability [32,33,171].
- τ_M , the flow onset stress, should be maximized to improve buildability. This property was selected over the yield stress (which represents the end of the LVER) as some studies

have found that nonlinear viscoelastic behavior contributes significantly to buildability in 3DCP [86,87].

- t_{open} , the open time, should approximately match the material residence time in the system—about 20 minutes in this work [6]. This is taken as the time for G' to reach 200 kPa [24].

4.3. Experiment

4.3.1. Materials

Commercially available ASTM C595 portland-limestone cement (PLC) (Buzzi, Chattanooga, TN) and metakaolin (MK) (KaMin, Gordon, GA) were blended to create the binder. A commercially available polycarboxylate-based suspension (MasterGlenium 7920, Master Builders) with 36% solids content was used as the superplasticizer (SP). Chemical and physical characterization of the PLC and MK are given in Tables 4.1-4.2 and 4.3, respectively, and particle size distribution is given in Fig. 4.1. Particle size analysis was performed using laser diffraction of the suspended powder in 99.5%-purity isopropanol (Malvern Mastersizer 3000E); specific surface area was approximated from the particle size analysis, assuming spherical particles and using the producer-reported specific gravities in Table 4.3 [89]. Oxide compositions were obtained through x-ray fluorescence spectroscopy, while phase composition of the cement was determined from Rietveld-refined quantitative x-ray powder diffraction (Rigaku Miniflex, Cu-K α radiation, 5-70° 2 θ) with 15% by weight 99.9%-purity zinc oxide as internal standard. A natural (alluvial) masonry sand was used as the aggregate in the mortars to comply with the printer's limitations on maximum particle size. The aggregate was brought to saturated – surface

dry condition before mixing. Its size distribution is given in Fig. 4.1 and a summary of its physical properties is in Table 4.4.

Table 4.1. Oxide composition of PC and MK in percent by weight.

Component	PC	MK
CaO	64.45	0.02
SiO ₂	19.45	51.77
Al ₂ O ₃	4.23	43.75
Fe ₂ O ₃	3.18	0.47
SO ₃	2.59	0.04
Na ₂ O	0.10	0.25
K ₂ O	0.63	0.16
MgO	3.68	0.04
TiO ₂	0.26	1.61

Table 4.2. Phase composition of PC.

Component	Weight %
C ₃ S	50.5
C ₂ S	19.1
C ₃ A	1.4
C ₄ AF	8.0
Calcite	11.0
Dolomite	2.7
Brucite	0.7
Gypsum	1.9
Bassanite	3.5
Minor Phases/Amorphous	1.2

Table 4.3. Physical characteristics of PC and MK

Property	PC	MK
D ₁₀ (μm)	1.81	0.72
D ₅₀ (μm)	13.38	3.74
D ₉₀ (μm)	35.55	10.79
SSA (m ² /kg)	572	1449
Specific Gravity	3.11	2.48

Table 4.4. Physical characteristics of the sand used.

Property	Value
Bulk Specific Gravity	2.59
Random Packing Density, ϕ_m	0.62
Fineness Modulus	1.70
Max Grain Size	2 mm
Absorption Capacity	1.2%

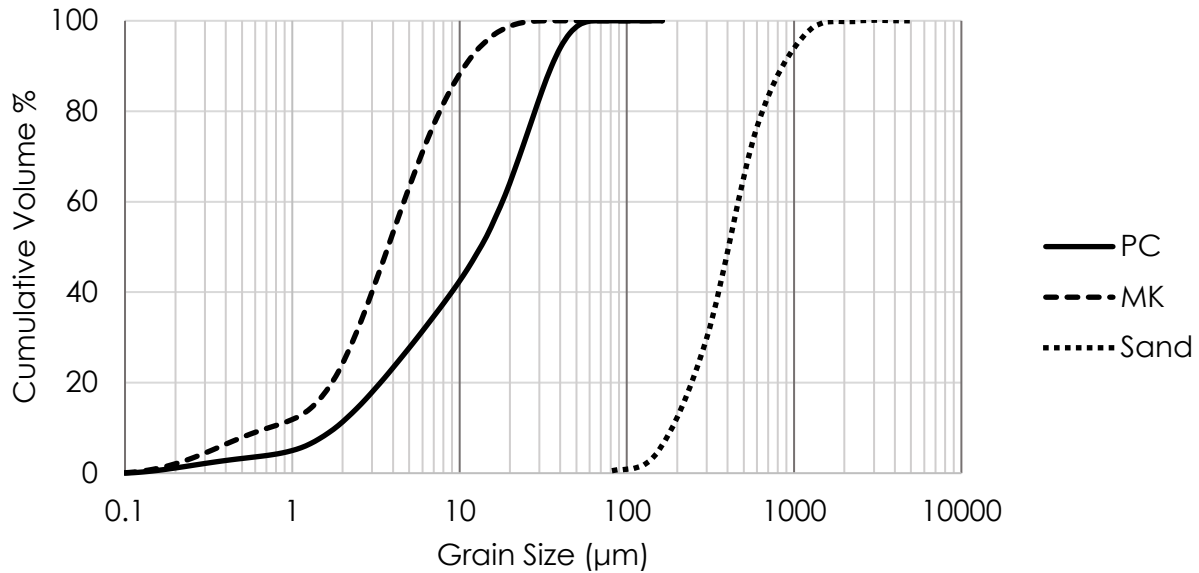


Fig. 4.1. Particle size distributions of binder powders and aggregate.

4.3.2. Rheometry

The preliminary rheological evaluation consisted of 54 pastes with w/b between 0.30 and 0.45, MK substitution of PLC between 0 and 30% by mass, and SP dosage by weight of binder (PLC and MK) between 0 and 0.4%. The SP dosage herein is given by weight of solids (i.e., active ingredients), not by weight of total product, to directly quantify polymer-particle interactions in the HML model. The water from the liquid SP suspension is accounted for in the mixture w/b. The complete dataset of mixtures, including rheological results, is given in Table 4.5. Generally, mixtures were tested at w/b of 0.30, 0.35, 0.40, and 0.45; MK substitutions of 0, 10, 20, and 30%; and SP dosages of 0, 0.1, 0.2, and 0.4%.

Rheological testing of cementitious pastes was carried out using a 50-mm parallel plate testing geometry (Anton Paar MCR 102). The gap between plates was initially set to 1 mm, and 80-grit sandpaper was adhered to the plates to mitigate slip [172,173]. The test configuration was selected to accommodate stiff mixes prone to wall slip in other geometries [173,174]. The

rotational frequency ω was maintained at 10 rad/s during all tests as this has been observed to be within the LVER for cementitious systems [138,162,164]. Tests were conducted at a constant temperature of 25°C. All reported rheological values are the averages of duplicate tests.

Paste samples for rheometric testing utilized 20 grams of binder, with appropriate amounts of deionized water (resistivity of 18.2 M Ω) and SP added. All materials were conditioned to 21 \pm 2°C before mixing. An automated immersion mixer (Hamilton Beach) was used for mixing according to the following procedure: binder was added to water (with SP, if used), the sample was mixed at medium speed (approximately 700 rpm) for 90 seconds, the bowl was scraped for 30 seconds, and the sample was once again mixed at medium speed for 60 seconds. After mixing, excess material was placed on the bottom plate, the top plate was moved into position, and the sample was trimmed. Once the sample was trimmed, it was ensured that no normal force, which would act as a confinement pressure and influence the shear properties, was acting on the sample.

Because shear history has a pronounced effect on the rheology of thixotropic materials, such as cement paste, a standardized pre-shear before each test was applied [174]. The goal of the pre-shear was to destroy any formed microstructure so that all tests could be considered as beginning from the same reference state. In lieu of a high-frequency continuous rotation, oscillation was utilized in the pre-shear: for 30 seconds, the material was subjected to 10% strain (considered in the large amplitude regime) at the same frequency as in testing (10 rad/s). Per Bellotto [164], this sufficiently deflocculates the sample while minimizing risk of fracturing it. After the pre-shear, the sample was rested for 30 seconds so that the test was not influenced by initial percolation and rigidification, reported by Roussel et al. [157] to occur on this time scale.

In the amplitude sweep, the sample was subjected to an increasing shear strain amplitude from 0.0005% to 1% (5 to 10,000 microstrain) in 24 logarithmically spaced steps while the corresponding stress was recorded at each strain step [175]. The time sweep followed the amplitude sweep on the same sample. The pre-shear and resting procedure outlined above was applied in between these two tests. In the time sweep, the sample was subjected to a small shear strain within the LVER at 30-second intervals for 60 minutes, leading to a total of 120 time steps. This test was designed to probe the evolution of rheology during the induction period of cement hydration [158]. The system was set to maintain zero normal force during the time sweep test by reducing the gap [176]. The testing apparatus was protected from evaporative water loss by filling the ring around the bottom plate with water; this was observed to work as well as more complicated methods to prevent evaporation. Thus, the reduction in gap is assumed to account strictly for chemical and autogenous shrinkage [176].

4.3.3. Data Analysis

Rheological data was imported into MATLAB (R2025a, including Statistics and Machine Learning Toolbox) to develop predictive models for selected rheological properties. The workflow is detailed in this section. Note that, in lieu of average values, duplicate test results for each mixture design were directly incorporated into the model to more directly account for repeatability.

4.3.3.1. Classification of Testable Mixtures

Of the sample set of 54 mixtures, six did not form a homogenous, viscous paste and thus could not be characterized through rheometry. To predict whether a simulated mixture would be testable—and thus whether a predicted rheological property was within the bounds of the

training data—a model was trained for binary classification of a mixture as testable or untestable using the same features as for rheological property prediction. The result is a multidimensional decision boundary which demarcates testability in terms of the coupled effects of the individual features.

The decision boundary was constructed with RUSBoost, which utilizes adaptive boosting with random under-sampling to address the class imbalance present in this data (i.e., 48 testable mixtures, 6 untestable mixtures) [177]. At each boosting iteration, a balanced training subset was formed by randomly under-sampling the majority class (i.e., testable), allowing the ensemble to learn decision rules influenced by the minority class (i.e., untestable). The model was trained with a learn rate of 0.1 over 200 cycles, with a specified minimum leaf size of five observations to mitigate overfitting. Additionally, the relative importance of each feature in classifying the mixture was measured through its Gini impurity: for each feature, the importance score reflects the average reduction in classification loss contributed by that feature across all trees in the ensemble. Features that consistently produced large reductions in loss were considered more influential in determining whether a mix was untestable.

4.3.3.2. Preliminary Evaluation by Linear Regression

A model for predicting rheological properties was first formed via linear regression to assess the ability of a simple model to capture trends in the data. Linear regression seeks to find optimal coefficients β to relate the response y to a vector of predictor variables X such that $y = \beta X^T + \varepsilon$, where ε is the error. Standardizing both predictors and responses ensured that all variables are on the same length scale, allowing the magnitude of β to indicate the relative importance of each feature, and the sign to indicate whether it is directly or inversely proportional to the response.

4.3.3.3. Dimensionality Reduction

To mitigate overfitting on this high-dimensional dataset, a dimensionality reduction approach based on least absolute shrinkage and selection operator (LASSO) regression was employed. LASSO functions as a guided linear regressor, with the guiding assumption that many features are largely irrelevant in predicting the response, and thus that many regression coefficients tend toward zero. The algorithm is controlled by the penalization parameter λ , which governs the magnitude of coefficient shrinkage and can be considered in the context of a bias-variance tradeoff. In MATLAB, a five-fold cross-validation scheme is utilized to determine λ . Both the λ value that minimizes prediction error as well as that which achieves minimal complexity (and thus greatest generalizability) while only reducing the accuracy by one standard error are computed; the latter is used as the selected feature set for model training.

In this work, LASSO selected from individual features and pairwise interactions. While the machine learning model itself can capture feature interactions, LASSO can be used outside the HML framework to identify the interactions which best capture rheological behavior, promoting faster model convergence and better generalizability.

4.3.3.4. Rheological Property Prediction

This research used Gaussian process regression (GPR) models for rheological property prediction due to their suitability for small datasets with highly non-linear relationships and feature interactions. Additionally, GPR is a Bayesian method, and thus predicted a Gaussian probability distribution for a target variable, rather than a single value, enabling direct uncertainty quantification. All outputs except t_{open} were transformed using a base-10 logarithm

to account for variation over several orders of magnitude, and all data were standardized (zero mean, unit variance) prior to training.

Model evaluation utilized a leave-one-out cross-validation (LOOCV) scheme. This approach works well for small datasets where withholding a larger testing set would remove an unacceptable amount of training data. In LOOCV, the model is trained on all data samples except one, and the prediction is made for the single remaining sample, a process which is then repeated until every sample in the population has been left out.

GPR is a kernel-based method, where the kernel defines similarities between adjacent observations and allows the model to handle non-linear relationships efficiently. In this work, the kernel selected is the Matérn function with automatic relevance determination (ARD) and the Matérn exponent set to $3/2$. While the Matérn function generalizes well for highly complex data, ARD allows for variation of the predictions over differing length scales (orders of magnitude) [165]. A linear basis function was used to capture basic rheological trends while mitigating overfitting.

4.3.3.5. Multi-Objective Optimization

Using the completed models, the selected rheological properties could be predicted from mixture composition. Predictions were performed over the experimental space at w/b increments of 0.01, MK substitution at increments of 1%, and SP dosage at increments of 0.01%. This resulted in a total of 20,336 simulated mixtures. From this synthetic dataset, a multi-objective optimization scheme was defined to select mixtures that are predicted to exhibit optimal performance in printing. A Pareto front was constructed to determine favored mixture designs: a mixture was deemed Pareto-optimal if improving one of its objectives necessarily worsens another [178].

These Pareto-optimal solutions are referred to as non-dominated. The first step of this procedure was defining the objectives.

By considering the criteria established in Section 4.2.2, optimization objectives for G' and τ_M were defined as “larger-the-better,” η' was “smaller-the-better,” and t_{open} was “nominal-the-best” (and is system dependent). To identify non-dominated solutions, each mixture was assigned normalized “desirability” scores for each property. For example, a mixture with the highest observed G' (or lowest observed η') in the simulation would have desirability for that property of 1, while the lowest observed G' (or highest observed η') would have a desirability of 0. In practice, 5th and 95th percentile mixtures for each property were used in place of the absolute minimum and maximum to protect against outliers. For larger-the-better and smaller-the-better objectives, desirability scaled linearly between the upper and lower bound percentile values. For nominal-the-best objectives, an exponential decay function better modeled desirability. The desirability of all four properties for a given mix was assembled into an objective matrix with all objectives weighted equally. Finally, a series of nested logical statements determined whether a given mixture has a more optimal option or if it is non-dominated. Of the Pareto-optimal mixtures, those selected for validation and printing had the highest average desirability score across the four rheological properties.

4.3.4. Validation and Printing

To validate the HML modeling, the selected optimal pastes were used to form mortars for printing. In this work, mortars are designed with an aggregate-binder mass ratio (a/b) of 1.2; many mixtures in the literature have an a/b near this value [6,7,9,29–37]. For a mixture to be suitable for printing, the mortar must first be extrudable by the given printer without clogging or

segregation. Buildability is then quantified by measuring an elastic property of the extruded material. Here, yield stress is determined using the Slugs test [74] to measure buildability.

The printer used in this experiment was a 3D PotterBot 10 Micro. This benchtop printer utilizes a ram extruder with a 70 mm diameter barrel and 19 mm diameter die. The printed object was a square column with 60 mm side length and 6 mm layer height. The nozzle speed was 20 mm/s, with a material flow rate of 8.2 L/hr. The mortars were mixed using the same equipment and same mixing speed as for the pastes, with the following procedure: the paste was mixed for 60 seconds, the aggregate was added and the mortar was mixed for 60 seconds, the bowl was scraped for 30 seconds, and the mortar was mixed once again for 30 seconds.

4.4. Results

4.4.1. Rheological Properties

A complete summary of rheological testing for the 48 tested mixtures, including their compositions and values for selected relevant properties, is detailed in Table 4.5. Mixtures 22, 25, 26, 31, 34, and 43 were too stiff to test. Table 4.6 shows the Pearson correlation values between the rheological parameters.

Table 4.5. Measured rheological properties by mixture composition. Values should be taken as having three significant figures, with time values to the nearest 30 seconds.

Mix	W/B	MK %	SP %	G' (kPa)	η' (Pa·s)	τ_M (Pa)	t_{open} (mins)
1	0.30	0	0.00	54.6	980	14.6	17.0
2	0.35	0	0.00	30.9	763	4.28	11.0
3	0.40	0	0.00	22.5	568	2.17	16.0
4	0.45	0	0.00	14.1	515	1.22	9.5
5	0.35	10	0.00	154	3410	23.9	7.0
6	0.40	10	0.00	98.0	2370	12.6	13.0
7	0.45	10	0.00	78.2	1800	9.66	12.0
8	0.40	20	0.00	236	5560	33.2	3.0

9	0.45	20	0.00	214	4920	33.5	4.0
10	0.30	0	0.10	35.7	727	24.5	14.0
11	0.30	0	0.20	17.2	394	11.9	19.0
12	0.30	0	0.40	0.115	2.78	0.255	34.0
13	0.35	0	0.10	11.1	189	6.19	20.0
14	0.35	0	0.20	3.34	69.3	2.76	30.5
15	0.35	0	0.40	0.00775	0.403	0.0274	53.0
16	0.40	0	0.10	3.82	85.4	3.14	32.0
17	0.40	0	0.20	1.42	32.8	0.982	34.0
18	0.40	0	0.40	0.00619	0.200	0.00875	60.0
19	0.30	10	0.10	50.5	714	32.4	19.5
20	0.30	10	0.20	44.3	945	36.5	13.5
21	0.30	10	0.40	4.02	71.0	6.71	23.0
22	0.30	20	0.10	-	-	-	-
23	0.30	20	0.20	45.0	645	66.6	15.5
24	0.30	20	0.40	6.99	108	14.0	21.0
25	0.30	30	0.10	-	-	-	-
26	0.30	30	0.20	-	-	-	-
27	0.30	30	0.40	37.6	781	79.1	11.0
28	0.35	10	0.10	27.8	447	16.1	15.0
29	0.35	10	0.20	10.7	235	11.7	29.5
30	0.35	10	0.40	0.0386	1.14	0.161	60.0
31	0.35	20	0.10	-	-	-	-
32	0.35	20	0.20	33.0	514	41.1	19.0
33	0.35	20	0.40	1.31	18.7	1.74	30.0
34	0.35	30	0.10	-	-	-	-
35	0.35	30	0.20	50.6	721	47.4	13.0
36	0.35	30	0.40	2.63	40.7	8.40	20.0
37	0.40	10	0.10	30.0	541	10.9	19.5
38	0.40	10	0.20	3.64	60.8	3.42	26.0
39	0.40	10	0.40	0.0785	1.76	0.153	45.0
40	0.40	20	0.10	41.9	694	18.3	16.5
41	0.40	20	0.20	12.8	207	18.3	23.0
42	0.40	20	0.40	0.297	4.65	0.535	39.0
43	0.40	30	0.10	-	-	-	-
44	0.40	30	0.20	40.2	623	40.0	17.0
45	0.40	30	0.40	0.940	12.7	1.93	28.0
46	0.45	10	0.10	22.3	430	7.28	25.5
47	0.45	10	0.20	1.47	29.5	1.77	31.0
48	0.45	10	0.40	0.00758	0.283	0.0216	60.0
49	0.45	20	0.10	42.5	732	12.4	19.0
50	0.45	20	0.20	12.5	202	13.0	19.0
51	0.45	20	0.40	0.203	2.55	0.213	40.0

52	0.45	30	0.10	107	2100	25.5	9.0
53	0.45	30	0.20	49.0	900	32.6	14.0
54	0.45	30	0.40	0.763	10.6	1.07	44.5

Table 4.6. Pearson correlation coefficients of four selected rheological properties.

	G'	η'	τ_M	t_{open}
G'	1			
η'	0.984	1		
τ_M	0.453	0.383	1	
t_{open}	-0.594	-0.559	-0.534	1

4.4.1.1. Effect of w/b

In the initial microstructure, a higher w/b leads to increased interparticle spacing and subsequently decreased interparticle interaction forces. The mechanical properties of fresh cementitious systems are governed by colloidal interactions (electrostatic interaction, van der Waal's forces) [159,161], so if the interparticle spacing increases, the system's elasticity generally will decrease [45]. In other words, a highly percolated system will have a well-connected network of suspended particles (anhydrous binder powder grains and early hydration products) which give the system elasticity; increasing w/b leads to poorer percolation. Therefore, as expected, increased w/b leads to decreased G' and τ_M , as shown in Fig. 4.2.

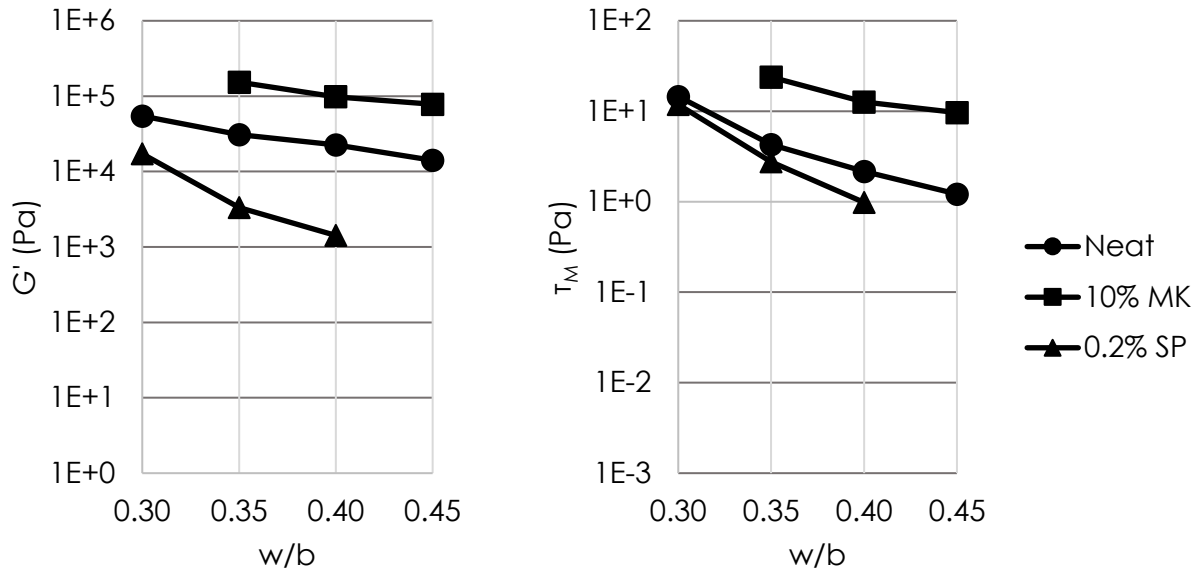


Fig. 4.2. Storage modulus and flow onset stress of mixtures of varying water-binder ratios.

There was no consistent effect of w/b on t_{open} . Mostafa and Yahia [161] reported that increased w/b led to more rapid microstructural percolation and decreasing rate of increase of G' , but that was not observed reliably here. While it is generally agreed upon that increased w/b leads to a later set time [117], Bentz [179] explained that for cement pastes with mid-range w/b (approximately 0.40 to 0.45), self-desiccation during hydration—which will preferentially occur in larger pores—may lead to preferential formation of hydrates in smaller pores, reducing capillary porosity and increasing strength more rapidly. However, further research is needed to reveal the true underlying mechanism of this observation.

4.4.1.2. Effect of Metakaolin Content

At a constant w/b and SP dosage, increasing MK substitution led to higher G' and τ_M , as expected [151,166,180]. MK increases rigidity of the fresh paste through several mechanisms, including high specific surface area and non-spherical morphology, both of which increase water demand. Additionally, the high surface charge of MK leads to increased adsorption of SP and

tendency to agglomerate in low-dimensional fractals, entrapping the lubricating water [153,181].

The effect of MK appears stronger than that of w/b, as the G' – MK and τ_M – MK curves are largely insensitive to w/b, as shown in Fig. 4.3.

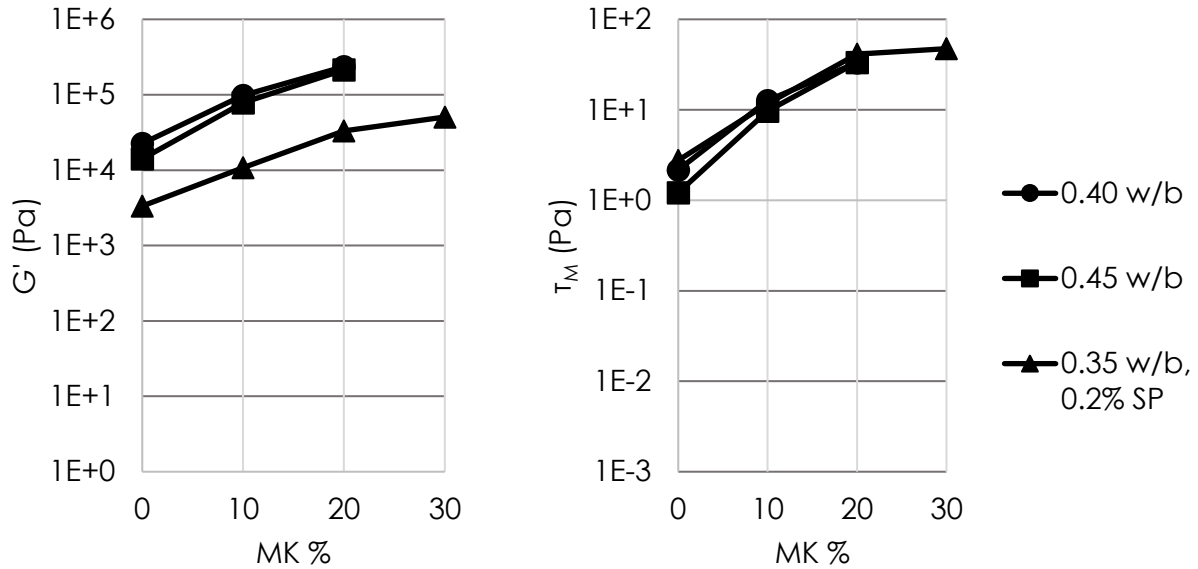


Fig. 4.3. Storage modulus and flow onset stress of mixtures of varying metakaolin substitutions. Increasing MK substitution also reduced open time (see Fig. 4.4). While increasing MK increased the immediate G' value, as discussed above, and thus would be expected to reduce the time for G' to reach 200 kPa, the finely divided clay particles also promote nucleation [161]. In the fresh state, this corresponds to an increasing number of pseudo-contact points between particles, leading to heightened particle-particle interaction forces. Additionally, the available surface area for precipitation of early hydration products is proportionally increased, further bridging anhydrous binder particles and strengthening the elastic interaction network.

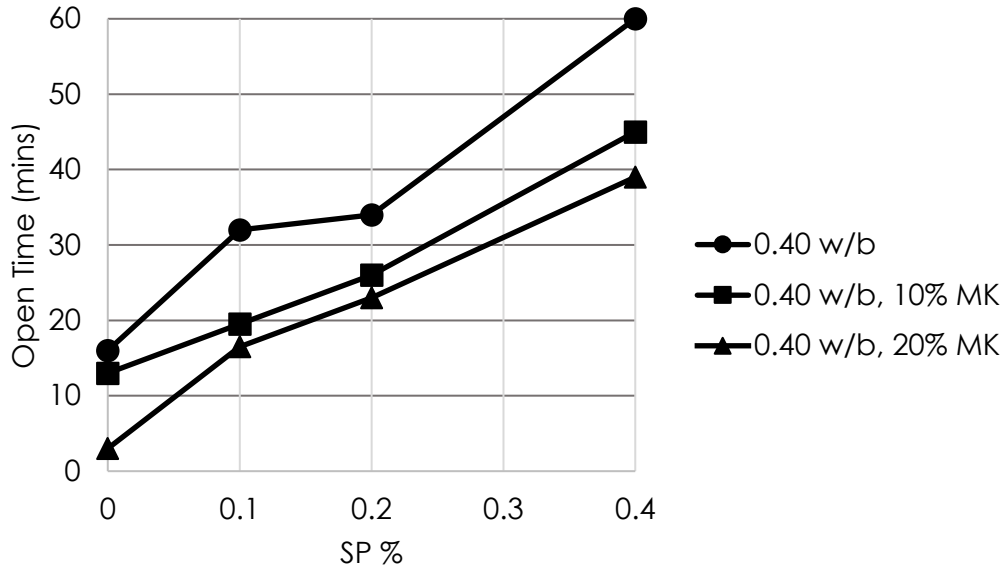


Fig. 4.4. Open time for systems with constant w/b of 0.40 with varying metakaolin substitution and superplasticizer dosage.

4.4.1.3. Effect of Superplasticizer Dosage

The dispersing action of polycarboxylate-based superplasticizers comes primarily through two mechanisms: steric hindrance and electrostatic repulsion [181]. SP increases the workability of the mixture by reducing agglomeration, in turn promoting the ability of water to lubricate individual (or smaller flocs of) binder particles. With respect to rheology, some authors have observed that SP dominantly reduces the yield stress and its effects on viscous behavior are minor [33,182], while others have observed that SP effectively reduces both yield stress and plastic viscosity [183,184]. In this work, plastic viscosity is not quantified directly, but increasing SP dosage was observed to effectively decrease both G' and τ_M , with a much stronger effect observed than that of w/b or MK substitution, as shown in Fig. 4.5.

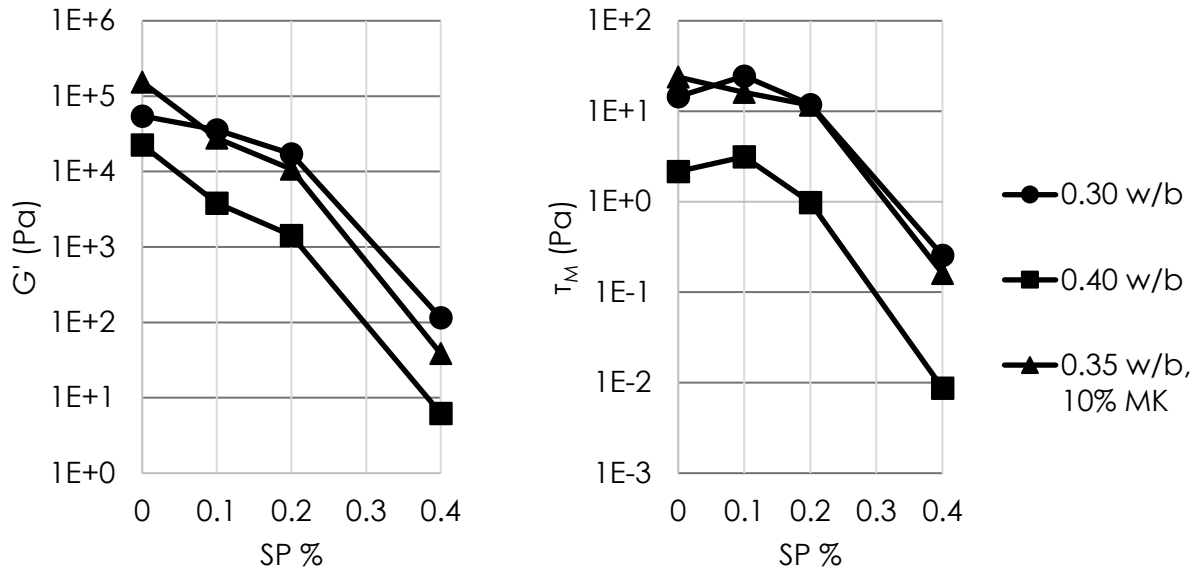


Fig. 4.5. Storage modulus and flow onset stress of mixtures of varying superplasticizer dosages.

The two systems without MK exhibited increased τ_M when SP was added at a dosage of 0.1%, before subsequently decreasing. This may be attributed to increased strain capacity (i.e., ductility) in the plasticized systems. The flow onset was achieved well after yield; the SP provided increased ability for the system to continue resisting shear inelastically at larger deformations.

Increasing SP also significantly extended t_{open} (see Fig. 4.4). The set retardation effect of polycarboxylate SPs is due to particle dispersion, preventing flocculation and microstructural percolation; adsorption onto binder particle surfaces, slowing their early dissolution; and complexation with Ca^{2+} ions in solution, reducing the available calcium to react with silicates and aluminates [185–187].

4.4.1.4. Combined Effects

To explore the combined effect of binder composition and SP dosage, Fig. 4.6 shows the G' and τ_M of mixtures with w/b of 0.40. Adding 0.2% SP reduced G' by an order of magnitude and

approximately halved τ_M , while substituting 20% MK increased both G' by an order of magnitude and τ_M by two orders of magnitude. The addition of SP had a similar effect to both the PLC and blended LC3 mixtures: G' decreased by an order of magnitude, and τ_M was roughly halved. Overall, MK had the strongest effect on G' , while SP primarily affected τ_M .

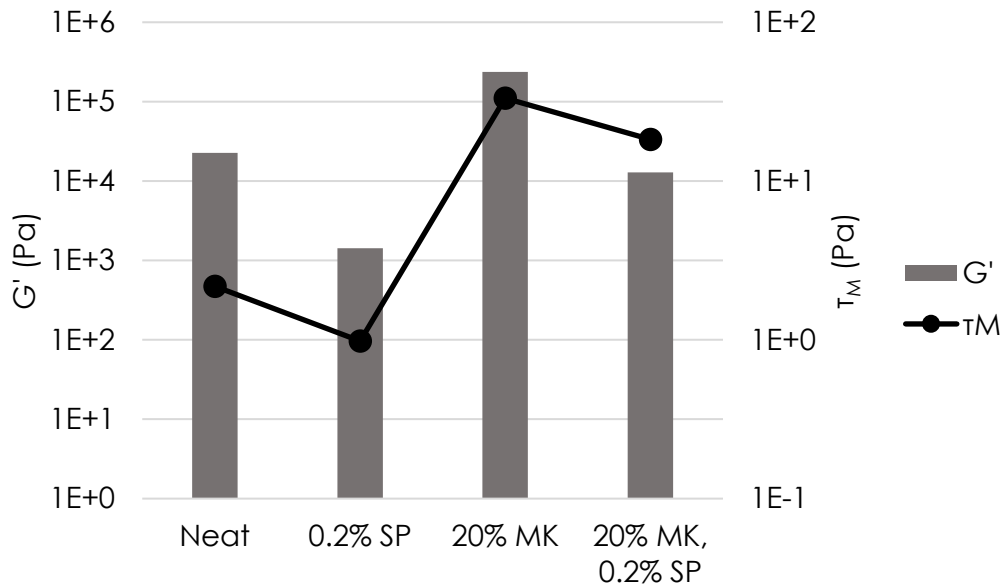


Fig. 4.6. Storage modulus and flow onset stress of neat, blended, and plasticized mixtures all with w/b 0.40.

4.4.2. Model Performance and Predictions

4.4.2.1. Feature Selection

Seven features were evaluated to serve in the “middle layer” in this HML model. The parameters represent a combination of particle loading, physical packing, and chemical interaction parameters.

- **Total solids fraction ϕ** is commonly utilized to model rheological behavior of suspensions. It is defined in Eq. 4.3 (f refers to the mass fraction of a given component). For a review of packing properties of cementitious materials, the reader is referred to [188].

$$\phi = \frac{1}{1 + w/b \left(\frac{SG_{PC}}{f_{PC}} + \frac{SG_{MK}}{f_{MK}} \right)} \quad (4.3)$$

- **Volumetric specific surface area** A_s quantifies the varying surface coverage of pastes with different binder compositions. This is especially critical for considering adsorption of admixtures onto particle surfaces. It is calculated with respect to the volume fraction and mass specific surface area of each component, as shown in Eq. 4.4.

$$A_s = \phi_{MK} SG_{MK} SSA_{MK} + \phi_{PC} SG_{MK} SSA_{PC} \quad (4.4)$$

- **Total particle density** TPD is a metric of the number of particles occupying a unit volume; in this work, it has the unit of particles per 100 μm^3 . While it is related to the solids fraction (in total, and of each binder component), it also accounts for their differences in size and polydispersity [157,166]. It is defined in Eq. 4.5.

$$TPD = \frac{\phi}{\sum(\phi_i d_i)^3} \quad (4.5)$$

- The **particle packing index** K was introduced by de Larrard [189] to quantify the dry packing efficiency of concrete mixtures. Mixes with a high packing index have minimized skeletal porosity, which has been demonstrated to optimize mechanical behavior of cementitious systems in both the fresh and hardened states [168,190]. K considers the interaction between different components, based on the loosening effect term a and the wall effect term b . These terms are calculated based on the full particle size analysis for each considered grain size d , as in Eqs. 4.6-4.7.

$$a_{ij} = \sqrt{1 - \left(1 - d_j/d_i\right)^{1.02}} \quad (4.6)$$

$$b_{ij} = 1 - \left(1 - d_i/d_j\right)^{1.5} \quad (4.7)$$

Using these terms and the relative volume fraction for each grain size ϕ_i , the maximum computed packing density of each component γ_i is estimated (Eq. 4.8), allowing for the calculation of K (Eq. 4.9). The packing index is a function of γ_i and the virtual packing density of each component β_i . The packing fraction β was assigned as 0.74 for all components, which follows from the assumption of monodisperse spherical particles [166,190].

$$\gamma_i = \frac{\beta_i}{1 - \sum_{j=1}^{i-1} \left[1 - \beta_i + b_{ij}\beta_i \left(1 - 1/\beta_j\right)\right] \phi_j - \sum_{j=i+1}^n \left[1 - a_{ij}\beta_i/\beta_j\right] \phi_j} \quad (4.8)$$

$$K = \sum_{i=1}^n \frac{\phi_i/\beta_i}{1/\phi - 1/\gamma_i} \quad (4.9)$$

- **Water film thickness WFT** is used to quantify the water in the system which goes towards lubricating particles, rather than filling interparticle voids [191]. It can be expressed as the proportion of excess water in the system to (volumetric) surface area, as in Eq. 4.10. μ'_w can further be defined in terms of the total solid volume fraction ϕ by considering the voids ratio μ and the water ratio (by volume) in the system μ_w as in Eq. 4.11. WFT has been used in a previous HML effort to predict concrete strength [168] and has been shown to also exhibit a strong relationship to rheology [192,193].

$$WFT = \frac{\mu'_w}{A_s} \quad (4.10)$$

$$\mu'_w = \mu_w - \mu = (1 - \phi) - \frac{1 - \phi}{\phi} = -\frac{(\phi - 1)^2}{\phi} \quad (4.11)$$

- **Proportion of adsorbed superplasticizer** θ quantifies the efficiency of SP in the system; only SP which is adsorbed is expected to have a significant effect on material rheology [185–187,194]. The polymer which adsorbs onto the surface of the binder grains will alter the surface charge—promoting dispersion through electrostatic repulsion—and provide a physical barrier to flocculation through the comb-polymer’s side chains (steric hindrance). The adsorption behavior of the SP onto binder particles obeys the Freundlich isotherm: $\theta = KC^{1/n}$ where C is the added concentration of the adsorbate and K and n are empirically determined fitting constants. The fitting constants quantify the initial efficiency of adsorption and how quickly the surface saturates with adsorbate. The isotherm constants were determined from the data from Chen and Plank [183], who explored the surface chemistry of cement – calcined clay systems with a polycarboxylate SP—see Eqs. 4.12-4.13. Thus, the adsorption proportion will depend on the relative amounts of PLC and MK, and the SP dosage. In these isotherms, C is the SP concentration in mg solid addition per g binder.

$$\theta_{PC} = 0.247 C^{1/2.71} \quad (4.12)$$

$$\theta_{MK} = 0.414 C^{1/2.18} \quad (4.13)$$

- **Zeta potential** ζ is a measurement of the aqueous surface charge of minerals. Specifically, it is the electric potential at the edge of the diffuse layer of ionic species which complex with a mineral surface in solution. The zeta potential quantifies colloidal stability (tendency of the particles to flocculate) and thus directly relates to the suspension’s rheology. As SP adsorbs onto particles, their surfaces become saturated with SP, and some steady state zeta potential is reached [183,186,194–196]. Furthermore, the presence of MK strongly alters the zeta potential at lower SP dosages (i.e., below surface saturation) as these particles adopt a strong negative surface charge in solutions of high pH [181,185]. The values for zeta

potential of the solution are adapted from the study of Chen and Plank [183], who observed the zeta potential of solutions of OPC only (at w/b of 0.50) and OPC with 30% MK substitution (at w/b of 0.60). The w/b ratios used here are similar to those in practical applications, unlike other works in which the zeta potential is measured on a very dilute solution. Therefore, the pH, which strongly affects zeta potential, should be representative of a typical cementitious suspension [195,196]. Furthermore, while Chen and Plank used an ordinary portland cement (OPC) and the present study uses a PLC, the contribution of limestone to the zeta potential is assumed negligible, following from the work of Lowke and Gehlen [196], who found that the surfaces of limestone particles were effectively neutralized in a synthetic cement pore solution of high pH and high ionic strength. The zeta potential is calculated with respect to the SP dosage and by a linear rule of mixtures between the PLC and MK, as depicted in Fig. 4.7.

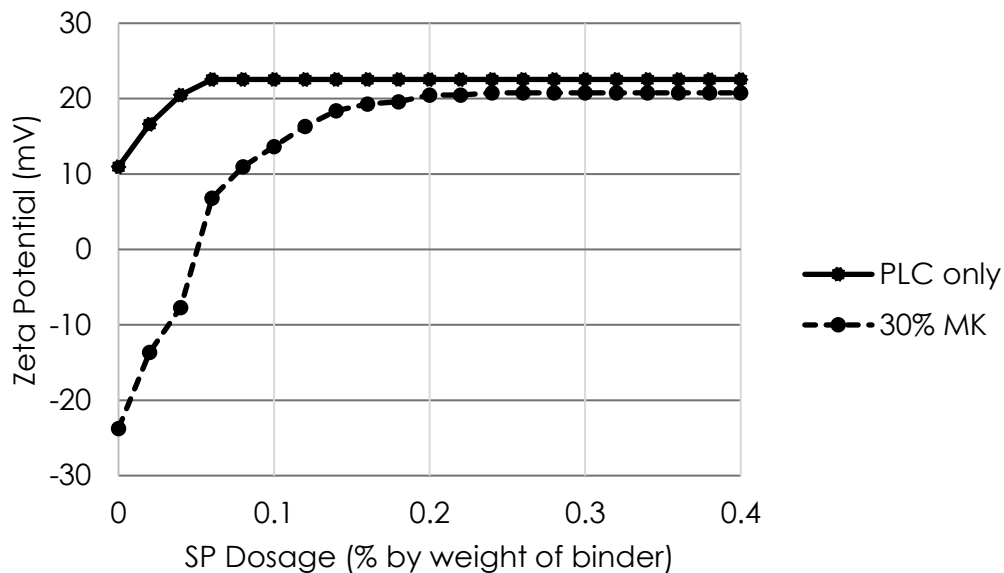


Fig. 4.7. Zeta potential as a function of superplasticizer dosage for a PLC only system and one with 30% MK. Adapted from [183].

It is recognized that the above features are not entirely independent. To mitigate overfitting, features could be eliminated from the middle layer if they do not sufficiently enhance model accuracy. Thus, four of the features are selected for HML: WFT , K , θ , and ζ ; model accuracy was not significantly enhanced by the presence of the other features. It can be concluded that the selected features represent, at least in part, independent physicochemical phenomena. This follows from understanding of the features; WFT is a function strictly of ϕ and A_s while K can be thought of as a more complex analog of TPD . The final HML approach is summarized in Fig. 4.8.

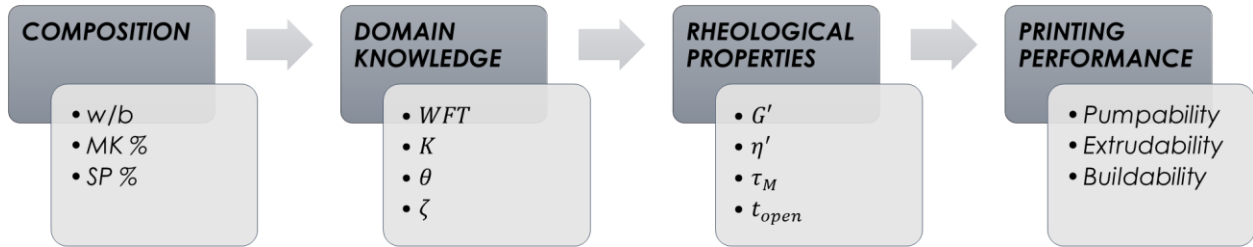


Fig. 4.8. Hierarchical machine learning approach utilized in this study.

To provide an interpretable quantification of feature importance, linear regression was first fit to the data of each rheological property using the four features selected above. The feature importance analysis, summarized in Table 4.7, indicated that for all rheological properties, the relative contributions of the predictors follow the trend $WFT \sim \theta > K > \zeta$. Despite this ranking, all coefficients were of the same order of magnitude, meaning the physicochemical interactions represented by all four features substantially affect rheology. The same relative order of importance for all four properties implies that they are controlled by similar phenomena. Note that for all coefficients, the p-value was on the order of 10^{-3} or less, implying that all four regressors were statistically significant in predicting the response.

Table 4.7. Linear regression coefficients and accuracy for rheological properties.

Property	β_{WFT}	β_K	β_θ	β_ζ	RMSE	R ²
G'	1.319	-0.865	-1.383	0.566	0.610	0.754
η'	1.193	-0.765	-1.355	0.502	0.584	0.758
τ_M	1.556	-0.927	-1.227	0.624	0.543	0.693
t_{open}	-1.107	0.637	1.142	-0.356	9.01	0.643

4.4.2.2. Decision Boundary

The construction of a decision boundary based on WFT , K , θ , and ζ allowed for the prediction of a mixture's ability to form as a homogenous paste and, more broadly, whether a simulated mixture was within the bounds of the training data. The model's performance was assessed using LOOCV and is summarized in the confusion matrix in Fig. 4.9. The model accuracy was 97% and it does not show preference toward incorrectly predicting either class.

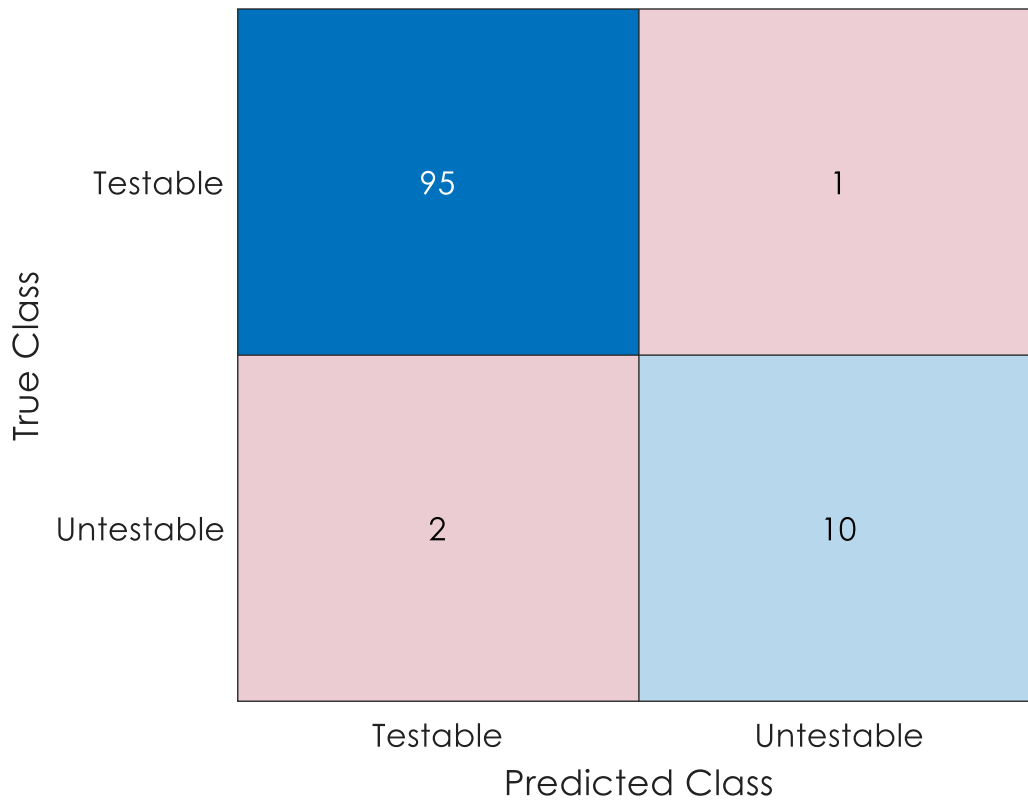


Fig. 4.9. Confusion matrix from LOOCV for classification of mixtures as testable or not testable.

The pattern of feature importance for classification of mixture testability differed from that for regression-based prediction of rheological properties, as shown in Table 4.8. While WFT was among the most informative predictors in both cases, K was an order of magnitude less important than the other features for predicting testability, whereas all features contributed at comparable magnitudes when predicting rheological properties. Additionally, ζ was more influential than θ for classification of testability, whereas the opposite trend was observed for rheological property prediction. Collectively, these findings indicate that particle lubrication (WFT) was the dominant factor governing whether a mixture was testable, followed by surface charge (ζ) and polymer adsorption (θ). The comparatively low importance of K implies that the ability to disperse particles through lubrication and (electrostatic or steric) stabilization exerted greater control over testability than their physical packing alone.

Table 4.8. Relative feature importance in determining testability.

Feature	WFT	K	θ	ζ
Importance	0.0522	0.0011	0.0251	0.0411

4.4.2.3. Accuracy and Confidence

Table 4.9 shows the accuracy of GPR models used to predict the four rheological properties, with training features determined through LASSO regression and accuracy evaluated through LOOCV, as detailed in Section 4.3.3. Note that the models for predicting G' , η' , and τ_M were log-transformed, so the RMSE is in physically insignificant units and can be considered a metric of the order of magnitude of the model's error.

Table 4.9. Accuracy of GPR models for rheological properties.

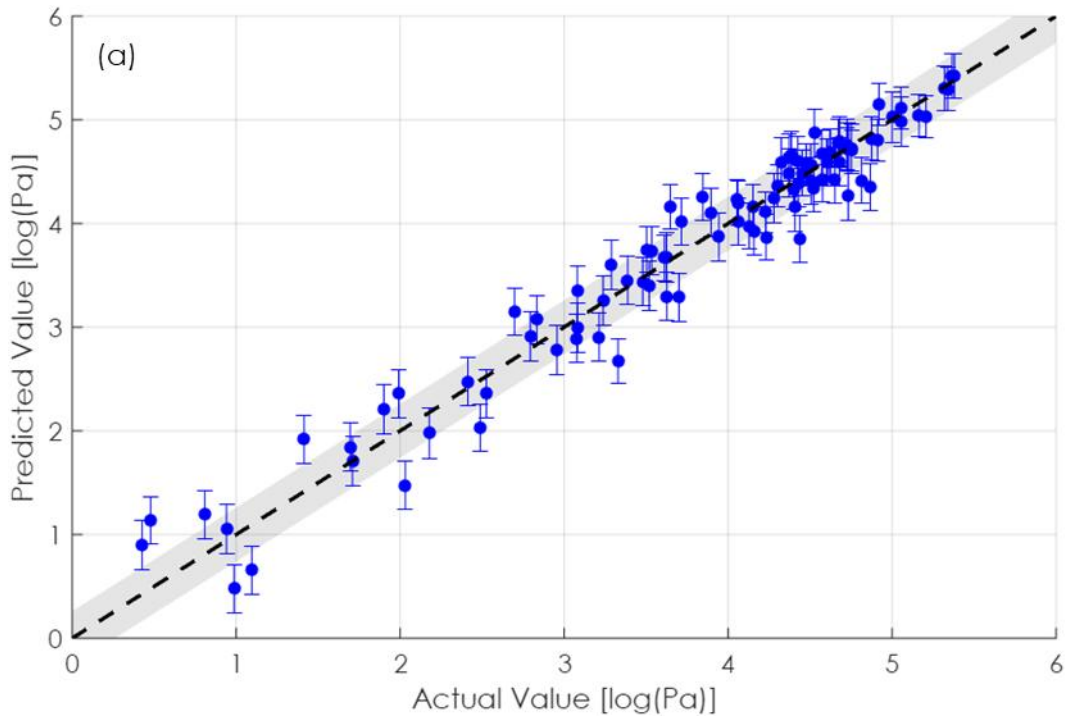
Property	RMSE	R ²
G'	0.259	0.953
η'	0.277	0.943
τ_M	0.204	0.954
t_{open}	7.22	0.758

The models for G' , η' , and τ_M all showed similarly high accuracies with R^2 of about 0.95, while the model for t_{open} had notably lower accuracy, implying it was harder to predict using the given set of features. Nonetheless, all models have greatly improved R^2 from the linear regression, implying that significant non-linear relationships and/or feature interactions describe the rheological behavior and supporting the use of machine learning.

Fig. 4.10a shows the parity plot from LOOCV for G' . The models for η' and τ_M exhibited similar performance to that of G' . The global standard deviation of residuals for this model was 0.26 in the log-transformed space. The inherent uncertainty (represented by error bars) was fairly uniform across all predictions, indicating that there were not any points the model considers uniquely difficult to predict. However, several mean prediction values deviated by more than one global standard deviation from the line of parity, especially at low values of G' . This behavior reflects the larger experimental variability observed in replicate rheological tests, which appeared generally greater in mixtures with low G' .

Fig. 4.10b shows the parity plot for t_{open} . The global standard deviation of residuals was 7.3 mins. Similarly to G' , the inherent uncertainty was relatively uniform. However, this model exhibited greater uncertainty in predictions overall, and more mean prediction values fell further from the line of parity. The observed variance between replicates for t_{open} was not noticeably higher than that of other rheological properties. This suggests that, although the model achieved moderately good accuracy, some physicochemical interactions—particularly those that affect

setting and rigidification behavior—were not well represented by the current set of features. Note that the clustering about 60 mins represents mixtures which did not achieve a G' of 200 kPa by the end of the time sweep test; these mixtures had a t_{open} far too long for successful printing, though a longer time sweep test would allow observation of the full open window. Additionally, some replicates did still exhibit high variance, such as those with w/b of 0.45, 30% MK, and 0.4% SP, represented by the outlier at 29 mins. This particular mixture, with all three compositional parameters at the upper end of the experimental space, represents an extreme case of several competing, nonlinear mechanisms.



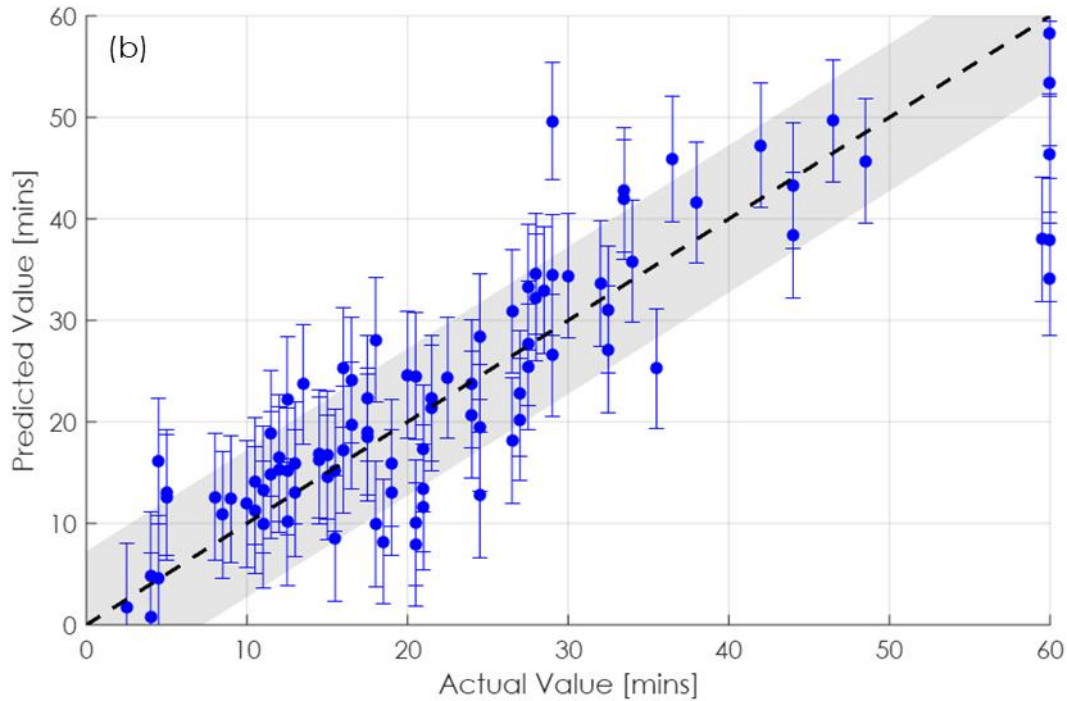


Fig. 4.10. Parity plot for predictions of G' (a) and t_{open} (b). Error bars represent one standard deviation of predicted probability distribution at individual points, while the shaded region represents one standard deviation of global prediction error over the whole dataset.

4.4.2.4. Mixture Selection via Multi-Objective Optimization

From the synthetic database of 20,336 mixtures, 1790 non-dominated, Pareto-optimal designs were identified. Two common design spaces could be identified when examining the most desirable Pareto-optimal mixtures: while all mixtures had w/b of 0.30-0.34, some had a high MK of 21-30% and high SP of 0.35-0.37%, while others had a low MK of 6-12% and low SP of 0.17-0.18%. In these groupings, all mixtures were predicted testable by the decision boundary. This shows that the objectives defined in Section 4.2.2 can be achieved through two different styles of mixture, one of which relies more heavily on stiffening induced by MK and dispersion induced by SP than the other. Notably, the mixture with the higher MK aligns more closely with common formulations for LC3 which use about 30% MK [8,144,190], posing it as the more sustainable alternative. For the sake of comparison, a representative paste composition could be identified

from each of these two general groupings: candidate mixture I with w/b 0.32, 9% MK, and 0.18% SP, and candidate mixture II with w/b 0.33, 28% MK, and 0.36% SP. The HML-predicted and actual rheological properties (averaged from two replicate tests) for these pastes are given in Table 4.10, demonstrating sufficient accuracy of the model predictions.

Table 4.10. Comparison of predicted and measured rheological properties of candidate mixtures, as predicted with logarithmic transform and with physical units. Values should be taken as having three significant figures, with time values to the nearest 30 seconds.

Candidate Mixture	G' log (Pa)		η' log (Pa · s)		τ_M log (Pa)		t_{open}	
	Pred.	Actual	Pred.	Actual	Pred.	Actual		
I	4.57	4.39	2.53	2.61	1.29	1.45		
II	4.09	4.28	2.10	2.52	1.38	1.68		
	(kPa)		(Pa · s)		(Pa)		(mins)	
	Pred.	Actual	Pred.	Actual	Pred.	Actual	Pred.	Actual
I	36.7	24.5	342	411	19.6	28.4	19.8	22.0
II	12.3	19.2	127	330	24.1	48.3	19.4	21.0

4.4.3. Validation by Printing: Paste to Mortar Scale

The goal of mortar-scale testing and printing was to determine whether optimization of the selected rheological properties can be used as a basis for design of printable mortars. When prepared for printing, the mortar based on candidate mixture II displayed pronounced shear thickening behavior, making extrusion very difficult. Hence, candidate mixture I was selected for printing. The full mixture design for the printed mortar is given in Table 9. The mixture was successfully extruded, and the yield stress of the mortar was measured to be approximately 590 Pa by the Slugs test [74]; in a comparative study, mixtures designed for 3DCP had a yield stress between approximately 200 and 1300 Pa as measured by the Slugs test [76].

Table 4.11. Selected mortar design for printing, from Candidate Mixture I.

Component	lb/yd ³ (kg/m ³)
PLC	1380 (819)
MK	136 (81)
Water	480 (285)
Sand	1821 (1080)
SP	7.58 (4.50)
TOTAL	3819 (2266)

During printing, the material held its shape during and immediately after extrusion. Thus, the material was sufficiently strong and stiff to withstand its own self weight [27,42] as well as forces from pressing by the nozzle [100,197,198]. However, the filament was prone to tearing, as can be seen in Fig. 4.11. The presence of filament tearing implies that the objectives of this experiment do not sufficiently account for appropriate viscous behavior of the material, as discussed in the subsequent section.



Fig. 4.11. Printing of the mortar designed from candidate mixture I.

4.5. Discussion

This work has employed a predictive framework based on machine-learned rheological characterization to select mixtures for 3D printing. The HML approach yielded models of high accuracy, while the targeted validation procedure via multi-objective optimization gave mixes whose rheological behaviors agree well with predictions. However, the candidate mixtures displayed two prominent issues: shear thickening and filament tearing.

Shear thickening has frequently been observed in cementitious systems with low w/b, high dosages of SP, and/or presence of clays [183,199–201]. Generally, shear thickening occurs due to particles in suspension being forced into direct contact (i.e., jamming) at high shear rates [202,203]. It can also occur in the presence of high quantities of polymeric additives (e.g., SP) due to entanglement [204]. Because the oscillatory rheometry procedure in this study does not impose sufficiently high shear rates to trigger shear thickening, this behavior was not captured within the present experimental regime. Moreover, the high-pressure environment inherent to ram extrusion may induce shear thickening by dilatancy. While oscillating at higher frequencies may have revealed behavioral irregularities [162,164], oscillatory rheometry conducted in the small amplitude regime may not impose sufficient deformation to force interparticle jamming. Additionally, oscillatory rheometry does not directly quantify the plastic viscosity (and its dependence on shear rate) as in rotational rheometry.

Filament tearing is a complex phenomenon which depends on both the material's viscous behavior and the inertial forces induced by the printing process [205]. While total rupture of the filament can occur due to inertial forces induced during printing [42,206], Fig. 4.11 depicts many small tears but continuous extrusion. Perrot et al. [207] proposed that filament inhomogeneities are formed by local dewatering, which can be framed in the context of soil mechanics and Terzaghi consolidation theory. On the other hand, many authors suggest that the ability of the

material to be pumped and extruded is governed by its tendency toward shear-induced particle migration, such that a lubrication layer can be formed [12,26,32,33,54,171]. The mechanisms of formation of the lubrication layer are in turn related to the mortar's aggregate content—which should be below about 80% of the random loose packing fraction to avoid jamming and dilatancy—and the viscosity of the constituent paste [90,96,171,188,205]. While the aggregate content in the mortars prepared at a/b of 1.2 is 67% of its random loose packing fraction, plastic viscosity is not directly quantified in oscillatory rheometry, nor is pressure-induced consolidation behavior. Therefore, the observed filament tearing can be attributed either to poor stability against pressure-induced filtration or excessive plastic viscosity precluding the proper formation of a lubrication layer.

The mixtures which exhibited these problems were predicted testable by the decision boundary. This suggests that the multi-objective optimization scheme in this work preferentially selected mixtures which were testable. However, mixtures which were testable were not necessarily printable, at least with ideal performance. These issues suggest shortcomings of oscillatory rheology alone in designing printable cementitious materials. A more complete predictive framework will involve techniques which particularly expose and quantify shear thickening and filament tearing. While high shear rate and high deformation are required to induce shear thickening, quantifying filament tearing is more difficult. It is hypothesized that filament tearing in this ram extruder is governed by extensional (not shear) flow at significantly high strain rates at the nozzle exit, resulting in significant structural breakdown and, in turn, local dewatering or lubrication layer instabilities. The damaged suspension, whose microstructure cannot adequately resist extension-induced tensile stresses, is therefore prone to tearing. Characterization relevant to filament tearing may thus involve extensional or extrusion rheometry [154,207]—perhaps

incorporating the Benbow-Bridgwater rheology model [208]—or tribological measurements [33,209]. Additionally, experiments which probe the kinetics of structural breakdown and thixotropic recovery, such as static yield stress recovery tests, may help establish whether the microstructure can rebuild sufficiently rapidly to offset damage and sustain tensile stresses during extrusion.

The formulation of the mixtures in this study can further be compared to other studies on printable LC3s from the literature. In general, other studies have employed lower-grade calcined clays of coarser particle size, higher crystallinity, and lower kaolinite content [37,97,210–213]. These act more like inert or weakly interactive fillers than as active colloidal particles in cementitious suspensions, and their coarser size demands less lubricating water. Contrastingly, the finely divided, largely amorphous, high purity MK used in this study has a large density of dehydroxylated, highly charged surfaces which adsorb SP, exhibit strong interparticle interaction, and promote rapid precipitation of aluminate-bearing hydrates [45,181]. While the lower-grade calcined clays still influence the crowding of solids in the suspension and associated rheological parameters, they contribute less to colloidal structuration due to reduced surface charge, chemical reactivity, and interparticle interaction. Thus, they less dramatically drive the formation of a percolated network of anhydrous binder particles and early hydrates [157] which markedly and rapidly increases the rigidity of the fresh material and may disrupt the printing process. Consequently, while high-grade MK is expected to enhance the pozzolanic behavior of LC3 systems, it may reduce rheological robustness and process tolerance in extrusion-based additive manufacturing.

4.6. Conclusions

This research aims to determine the ability of oscillatory rheometry, coupled with a predictive framework based on hierarchical machine learning, to find optimal limestone – calcined clay cement blends for printing. Based on the results of this work, the following conclusions are drawn:

1. Oscillatory rheology provides a mechanical framework to observe viscoelastic behavior in fresh cementitious systems. For 3DCP, the deconvolution of viscous and elastic components, and temporal evolution thereof, is especially relevant. Four rheological properties were treated as objectives for mixture design for 3DCP: the storage modulus G' , the real component of viscosity η' , the flow onset stress τ_M , and the open time t_{open} .
2. A decreasing w/b, decreasing dosage of SP, or increasing addition of MK led to an increase in G' and τ_M , as expected. While no clear trends were observed between w/b and t_{open} , decreasing dosage of SP or increasing addition of MK shortened the open window.
3. HML utilized relevant physical and chemical domain knowledge as features in the model, rather than the raw compositional variables, for improved accuracy and generalizability. All features were sound predictors of rheological behavior, and the order of feature importance was the same for all properties, implying they are all governed by similar microstructural phenomena.
4. Different features than for predicting rheological properties governed whether a mixture would form a homogenous paste and could be tested. While the water film thickness was highly relevant in predicting both testability and printability, SP adsorption was more influential for printability while surface charge related more to testability. Particle packing was an order of magnitude less important than other features in predicting testability, whereas all features were relevant for printability. A decision boundary based

on an adaptive boosting classification algorithm successfully identified testable mixtures, though a mixture's testability did not guarantee that it exhibited ideal printing behavior.

5. GPR models showed high accuracy and low uncertainty for predicting G' , η' , and τ_M , and moderate accuracy and uncertainty for t_{open} . In a high-throughput simulation, these models predicted two groupings of mixtures for optimal printing: both with w/b of 0.30-0.34 and with either 21-30% MK and 0.35-0.37% SP or 6-12% MK and 0.17-0.18% SP.
6. The model's prediction was validated by printing a mortar with w/b of 0.32, 9% MK, 0.18% SP, and a/b of 1.2. While the mortar was successfully extruded and layered, it exhibited filament tearing. A mortar from the other grouping exhibited strong shear thickening and could not be extruded.
7. Future work should focus on forming a more complete suite of experimental methods for characterizing printing behavior, particularly for avoiding shear thickening and filament tearing. While the mechanisms of shear thickening are generally able to be observed through high-rate rotational testing, filament tearing is a more complex and poorly understood phenomenon whose quantification demands more research attention. While extensional or extrusion-based rheometry may subject the material to similar conditions as in printing, and thus could expose filament tearing directly, tests which probe the ability of the material to rapidly restructure after damage also directly relate to resistance to filament tearing.

CHAPTER 5. INSIGHTS INTO THE COMPRESSIVE AND FLEXURAL BEHAVIOR OF 3D-PRINTED CONCRETE THROUGH DIGITAL IMAGE CORRELATION

Abstract

This study investigates the hardened-state mechanical behavior of 3D-printed cementitious materials, commonly reported as having reduced strength or stiffness and mechanical anisotropy as compared to conventionally cast counterparts. In addition to a suite of bulk mechanical testing, digital image correlation is employed to investigate and contrast the failure modes of cast and printed specimens in compression and flexure. Additionally, the elastic modulus is measured in both compression and flexure to separately observe changes in strength and stiffness. Most mechanical properties were found to be statistically similar between cast and printed samples oriented in all three directions at the 5% significance level, though the elastic modulus in some printed orientations was significantly lower than cast samples in both compression and flexure. Additionally, digital image correlation showed generally similar failure modes across cast and printed specimens. This demonstrates that for the present mixture design and printing settings, which include a 10% adjacent layer overlap and very short pass time, mechanical performance of printed components is more similar to those cast, and more isotropic, than has been found in other studies.

5.1. Introduction

3D concrete printing (3DCP) shows promise as a nascent construction technology to reduce labor demands, material consumption, and requirements for geometric uniformity. However, a thorough understanding of the mechanical behavior of 3DCP members and structures, as compared to traditional cast-in-place concrete, is requisite to widespread adoption. Moreover,

two prominent mechanical phenomena may preclude the use of 3DCP in “heavy” infrastructural applications: anisotropy and reduced stiffness.

The presence of mechanical and microstructural anisotropy in 3DCP has been well documented, though the extent of anisotropy has varied widely across experiments in the literature [17,92,102,110–113,116,214–216]. Such anisotropy has commonly been attributed to the entrapment of air and formation of voids as a layer is deposited on the substrate [104], which leads to an oriented zone of decreased resistance to load and fracture [217–221]. More recently, it has been proposed that the formation of a lubrication layer during pumping results in material heterogeneity within the filament itself [26]. Meanwhile, stiffness loss in 3DCP components has been studied less thoroughly. Reinforced concrete members made partially or wholly by printing have sometimes exhibited similar stiffness to entirely cast counterparts [122,222,223], though at the material level, van den Heever et al. [131] found a significant reduction in stiffness in printed samples. A recent RILEM interlaboratory study [130] has partially corroborated this finding and attributed the stiffness reduction in 3DCP to increased material heterogeneity, though there was significant scatter in the results.

To further investigate anisotropy and reduced stiffness in 3DCP, an experimental program is adopted based on the aforementioned RILEM study and is supplemented with digital image correlation (DIC). DIC has been frequently used to investigate the material behavior of concrete, especially in the context of fracture and cracking [224–226], including for 3DCP [108,215]. This technique allows for the investigation of the characteristics of deformation (e.g., the full strain field) throughout the test, and thus allows observation of zones of concentrated damage and softening [227]. This study will pair quantitative mechanical testing with qualitative observation using DIC to investigate material behavior in 3DCP, as compared to casting.

5.2. Background

DIC tracks the deformation of an object by observing the movement of a speckle pattern on its surface. By assuming the speckle pattern is random, it can be divided into unique subsets which move relative to one another. A shape function can then be defined to quantitatively describe the deformation of some subset (as compared to a reference image) throughout the test [228].

Given a subset whose centroid is represented by a position vector $\vec{X} = (X_1, X_2)$, a deformation $\Delta\vec{X} = (u, v)$ is induced. DIC software algorithmically will solve for the parameter vector \vec{P} (as given in Eq. 5.1) such that the body undergoes an affine transformation: the deformation can be entirely modeled with each component and its first derivatives. The shape function $\vec{\xi}$ utilizes \vec{P} to describe the new, deformed configuration as the sum of the reference position, rigid body translation, and in-plane deformation and rotation, as given in Eq. 5.2. This is depicted graphically in Fig. 5.1.

$$\vec{P} = \left\{ u; v; \frac{\partial u}{\partial x}; \frac{\partial v}{\partial x}; \frac{\partial u}{\partial y}; \frac{\partial v}{\partial y} \right\} \quad (5.1)$$

$$\vec{\xi}(\vec{X}, \vec{P}) = \begin{bmatrix} X_1 \\ X_2 \end{bmatrix} + \begin{bmatrix} P_1 \\ P_2 \end{bmatrix} + \begin{bmatrix} P_3 & P_4 \\ P_5 & P_6 \end{bmatrix} \begin{bmatrix} X_1 \\ X_2 \end{bmatrix} \quad (5.2)$$

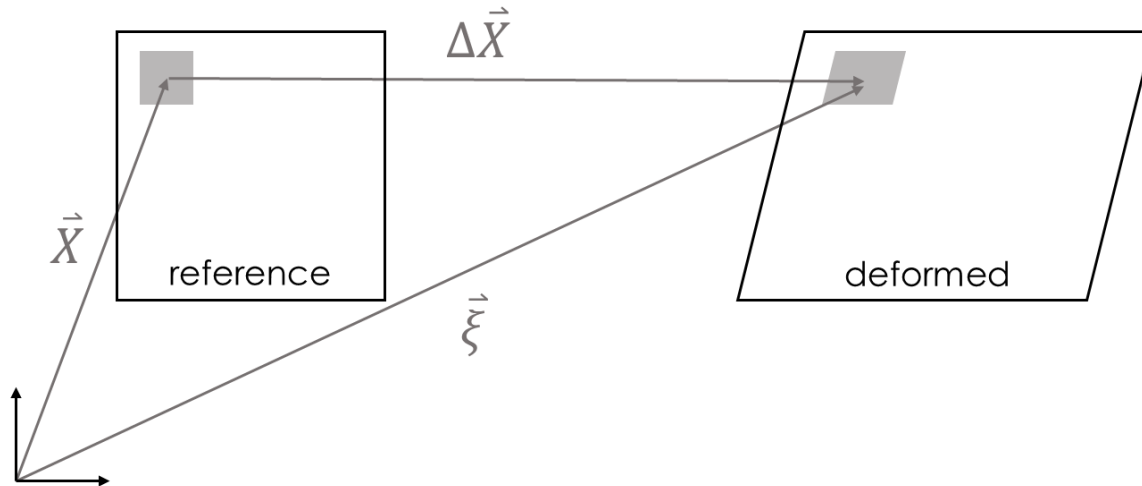


Fig. 5.1. Mapping of the deformation of a subset with respect to a reference configuration. While traditional (planar) DIC can only measure deformation perpendicular to the optical axis (i.e., the camera’s line of sight), this work utilizes stereo DIC (also called 3D DIC) which employs multiple cameras with an overlapping field of view to allow for measurement of the specimen’s deformation in all three directions via triangulation.

3D DIC operates through simultaneous correlation of images between the two cameras (stereo matching) and successive images from the same camera (temporal matching). A prominent advantage of 3D DIC is the ability to measure displacement both in the plane of the specimen and out-of-plane, though it also facilitates ease of testing by not necessarily having to orient the specimen face with a perfect perpendicular orientation to the optical axis.

5.3. Experiment

5.3.1. Materials

A commercially manufactured 3DCP material was used to print the specimens. To analyze the dry material, it was sieved through a 90 μm sieve to separate aggregate and powder (binder). The maximum aggregate size is approximately 3 mm. Oxide composition of the binder was

determined using x-ray fluorescence spectroscopy and is in Table 5.1. Particle size analysis of the binder and aggregate components is given in Fig. 5.2. The ratio of aggregate to binder is 1.29 by mass.

Table 5.1. Oxide composition of the commercial 3DCP binder.

Component	Mass %
CaO	66.05
SiO ₂	19.89
Al ₂ O ₃	5.24
Fe ₂ O ₃	2.99
SO ₃	2.98
Na ₂ O	0.08
K ₂ O	0.39
MgO	1.18
TiO ₂	0.32

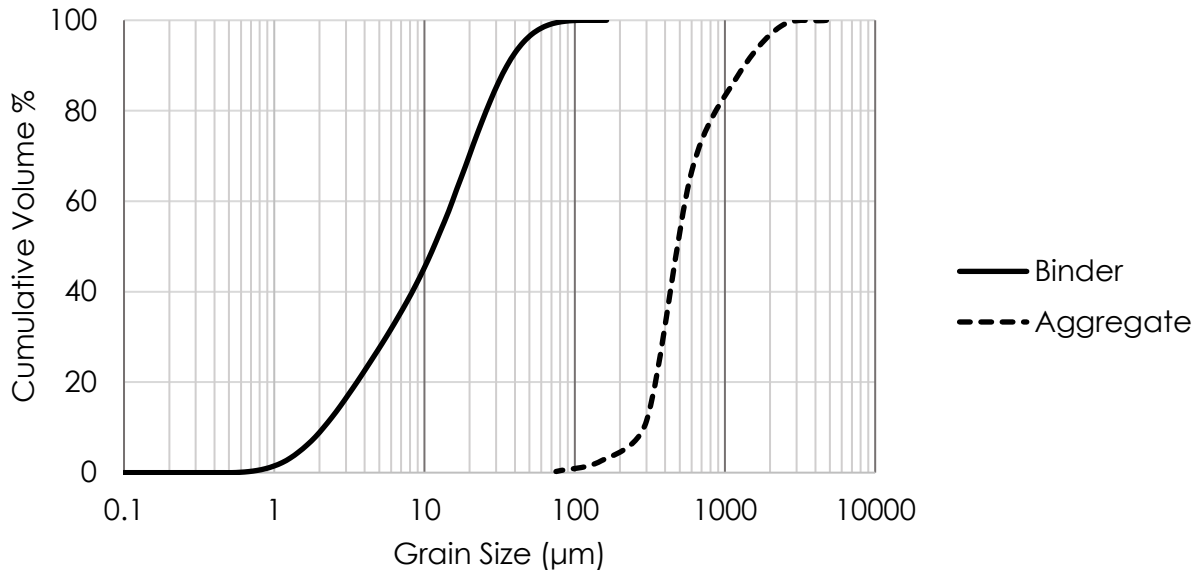


Fig. 5.2. Size distribution of the binder and aggregate portions of the printable material.

The material producer recommends a water addition of 14-16% by mass, corresponding to a water to binder mass ratio (w/b) of approximately 0.32-0.36. For the printing system used in this study, a water addition of 15% (w/b = 0.34) is optimal, and corresponds to an ASTM C1437 [79] flow of about 90%.

5.3.2. *Printing and Specimen Preparation*

To create the specimens for testing, several large rectangular blocks are printed, from which the specimens are extracted via saw-cutting. The printer in this experiment is a Delta WASP 3MT with a 30 mm diameter nozzle. The printer settings are detailed in Table 5.2. During printing, the laboratory was maintained at about 20°C and 60% relative humidity. Shortly after printing, the specimens are transported to a fog room maintained at 23°C and 100% relative humidity. Beam and cube specimens are cut from the printed blocks on the sixth day after printing (in time for 7-day testing) and are stored in the fog room until testing. Specimens were patted dry before testing.

Table 5.2. Printer settings used in this experiment. Note that the horizontal offset corresponds to an adjacent layer overlap of 10%, while the vertical offset exactly matches the desired layer height. The horizontal and vertical interlayer times are not constant

Setting	Value
Layer Width	30 mm
Layer Height	15 mm
Horizontal Offset	27 mm
Vertical Offset	15 mm
Printhead Speed	40 mm/s
Extrusion Flow Rate	1.08 L/min
Interlayer Time	< 150 s

5.3.3. *Mechanical Testing*

Mechanical testing procedures were adapted from the RILEM interlaboratory study mentioned in the Introduction [229]. The experiment is designed to discern the effects of casting versus printing, printed specimen orientation, specimen size, and specimen age on both flexural and compressive behavior. The axis convention is depicted in Fig. 5.3, and a list of tests is in Table 5.3. All tests utilized at least five replicate specimens, except for testing only three cast flexure specimens with 100x100 mm cross section.

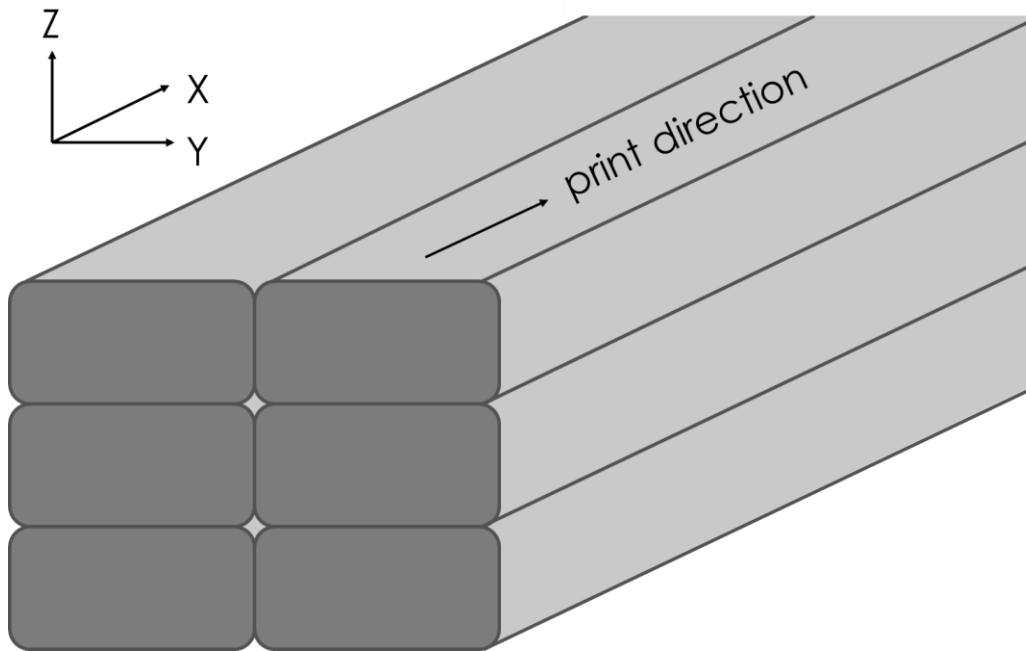


Fig. 5.3. Printed specimen orientation and axis convention.

Table 5.3. Tests conducted and naming convention.

Load Type	Orientation	Age	Size (mm)	Name
Flexure	Cast	28 day	50x50x150	R-C-S
			100x100x300	R-C-L
	Bend About X		50x50x150	R-X-S
			100x100x300	R-X-L
	Bend About Y		50x50x150	R-Y
	Bend About Z		50x50x150	R-Z
Compression	Cast	7 day		C-C-7
		14 day		C-C-14
		28 day		C-C-28
	Parallel to X	7 day	50x50x50	C-X-7
		14 day		C-X-14
		28 day		C-X-28
	Parallel to Y	28 day		C-Y
	Parallel to Z	28 day		C-Z

Tests were conducted in a hydraulically controlled MTS universal testing machine with a 300 kN capacity. Flexural specimens were tested in three-point bending as opposed to four-point bending to promote flexural failure over shear failure in the relatively short beams. Note that the elastic modulus was calculated from both compressive and flexural tests by examining the linear portion

of the stress-strain response, rather than using a separate testing procedure and determining the secant modulus.

The orientations of the tested beams are shown in Fig. 5.4. The loading rates for the four specimen types are given in Table 5.4 and are directly adapted from the RILEM TC 304 interlaboratory study [229].

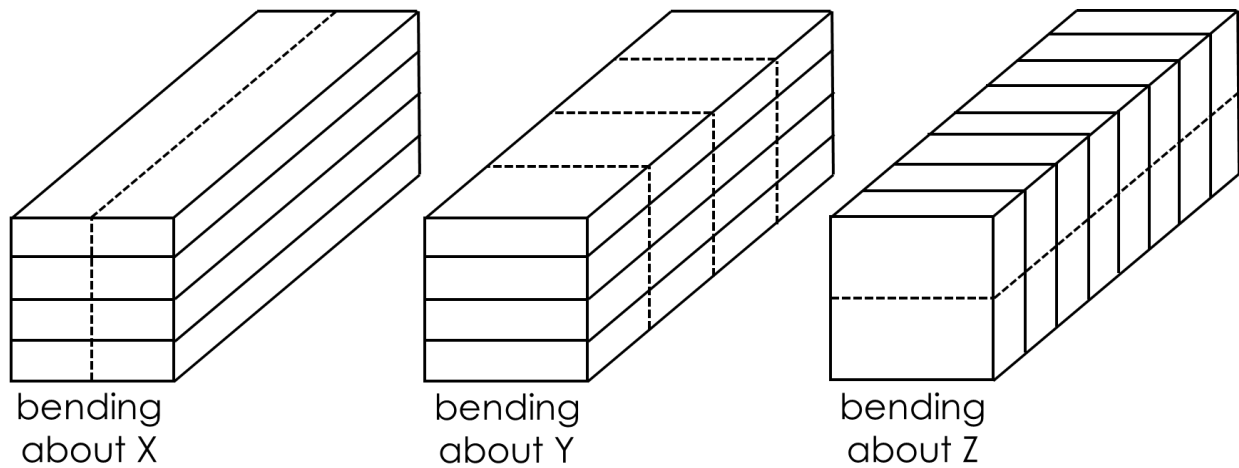


Fig. 5.4. Orientations of beams tested. Solid lines represent vertical interlayers, and dashed lines represent adjacent interlayers.

Table 5.4. Loading rates for the four types of specimens tested.

Load Type	Specimen Size	Cross-Section (mm)	Stress Rate (kPa/s)	Load Rate (N/s)
Flexure	Small	50x50	140	115
	Large	100x100	50	170
Compression	Small	50x50	960	2400
	Large	100x100	600	600

5.3.4. Digital Image Correlation

DIC was conducted using the commercially available Correlated Solutions VIC-3D system.

Stereo (3D) DIC was utilized over planar (2D) DIC to allow for rapid repetition of tests without needing to orient the specimen face perfectly orthogonal to the optical axis.

A lens with a short focal length was selected to accommodate a compact testing configuration. The frame rate was the maximum supported by the cameras. The selection of aperture size and exposure time can be thought of as a tradeoff. A narrow aperture (high f-number) allows for greater depth of field while a wide aperture (low f-number) lets in more light; short exposure times promote image sharpness but require sufficiently high lighting to capture a sufficiently bright image. For this reason, external lighting (beyond ambient brightness) is often required in DIC, and is used here. For sufficient depth of field, an f/11 aperture size was selected, which still allowed for a relatively short exposure time of 2.0 ms with appropriate external lighting.

To achieve an appropriate speckle pattern, specimen faces were painted white with matte spray paint and speckled using a roller. Where the roller did not cover the surface (i.e., in the case of divots), the speckles were manually placed with a Sharpie pen. The selected speckle size results in approximately 4-10 pixels per subset. The subset size and step size were left as the default of the software; the subset size is such that approximately 3-5 speckles are included per subset.

Table 5.5 contains a summary of the experimental parameters. Fig. 5.5 shows the test setup.

Table 5.5. Parameters for digital image correlation.

Parameter	Value
Camera Resolution	16 MP
Lens Focal Length	8 mm
Frame Rate	140 Hz
Aperture Size	f/11
Exposure Time	2.0 ms
Speckle Size	0.18 mm
Subset Size	29 px
Step Size	7 px



Fig. 5.5. Testing setup for digital image correlation.

5.4. Bulk Mechanical Properties

5.4.1. Compression

Results for compressive strength and elastic modulus are given in Tables 5.6 and 5.7, respectively. A one-way ANOVA test reveals that the difference in compressive strengths between cast specimens and those oriented in X, Y, or Z are not statistically significant. While some authors have found that the strengths in printed and cast specimens are similar, and that the effect of orientation (i.e., the anisotropy) is minimal, this may be due to the high degree of variance shown in the printed specimens. The printed specimens having higher variance aligns

with expectations from the literature; while the printing process is uniform, the printed specimens are likely to exhibit less compaction and thus a greater degree of heterogeneity.

Contrary to compressive strength, a one-way ANOVA test found statistically significant differences between elastic moduli at the 5% significance level (i.e., $p < 0.05$). A Tukey-Kramer pairwise comparison reveals that the elastic modulus in compression of the cast samples and those oriented in X are significantly different. Counterintuitively, the samples oriented in X are the strongest. In this orientation, the interlayer region—expected to contribute greatly to stiffness loss—is also not loaded. Nonetheless, the data demonstrate that the elastic modulus is reduced in printed specimens, though the strengths appear similar.

The effect of age cannot be discerned properly from these tests due to high variance. The greatly decreased stiffness with age in the cast specimens is especially confusing and may be due to poor specimen quality.

Table 5.6. Average compressive strength by orientation and age.

Orientation	Age (days)	f_c (psi)	COV (%)
Cast	7	4450	4.63
	14	4820	11.7
	28	4170	5.51
Z	7	4160	13.0
	14	3600	32.8
	28	4510	20.4
X	28	5890	26.2
Y	28	4430	23.1

Table 5.7. Average elastic modulus in compression by orientation and age.

Orientation	Age (days)	E_c (ksi)	COV (%)
Cast	7	536	18.8
	14	459	21.0
	28	164	13.8
Z	7	98	39.6
	14	134	51.5
	28	49	21.8
X	28	59	21.6
Y	28	48	25.0

5.4.2. Flexure

Results for flexural strength and elastic modulus are given in Tables 5.8 and 5.9, respectively.

Welch's t-test (i.e., without assuming equal variance) shows a statistically significant size effect for the flexural strength of cast samples, though not for those with bending about X.

Contrastingly, Welch's t-test shows a statistically significant size effect for the elastic modulus of those with bending about X, though not for those cast. These inconclusive results suggest the possible presence of a size effect in both printed and cast samples, though more research is required to definitively determine the extent of such a phenomenon.

No statistically significant difference was found between the cast and printed specimens of any orientation with regards to flexural strength. However, there is a significant difference in the elastic moduli of the cast specimens and those with bending about Y. This is a somewhat similar phenomenon as observed with respect to compression testing; no significant difference existed between the observed strengths, but there was such a difference in elastic moduli between the cast specimens and one orientation of the printed specimens. This suggests that printed specimens generally have a greater reduction in stiffness than strength as compared to cast counterparts.

Table 5.8. Average flexural strength by orientation and size.

Orientation	Size	f_R (psi)	COV (%)
Cast	Small	1090	9.06
	Large	726	11.4
X	Small	1080	15.0
	Large	980	10.0
Y	Small	950	17.4
Z	Small	860	17.2

Table 5.9. Average elastic modulus in flexure by orientation and size.

Orientation	Size	E_R (ksi)	COV (%)
Cast	Small	217	2.84
	Large	287	20.4
X	Small	174	42.2
	Large	295	25.7
Y	Small	113	46.1
Z	Small	125	26.4

5.5. Image Analysis

5.5.1. Compression

DIC images from compressive and flexural testing tended to reveal insights into the failure mode, though did not prominently show strain localization with regards to layer orientation. The following images show the normal strain in the longitudinal direction of the beam, ϵ_{xx} . Note that the direction x represents the horizontal direction in the image and does not relate to the printing orientation.

All compressive specimens demonstrated failure by axial splitting with various degrees of shear. Such failure modes are typical of cubes, whose lower aspect ratio than typical concrete cylinders contributes to a higher degree of constraint due to contact with the platens, and ultimately a more triaxial stress state. Fig. 5.6 shows a cast cube, which would have no influence of interlayer regions or printing-induced anisotropy. The localization of shear presents two axial paths unified by an inclined shear plane.

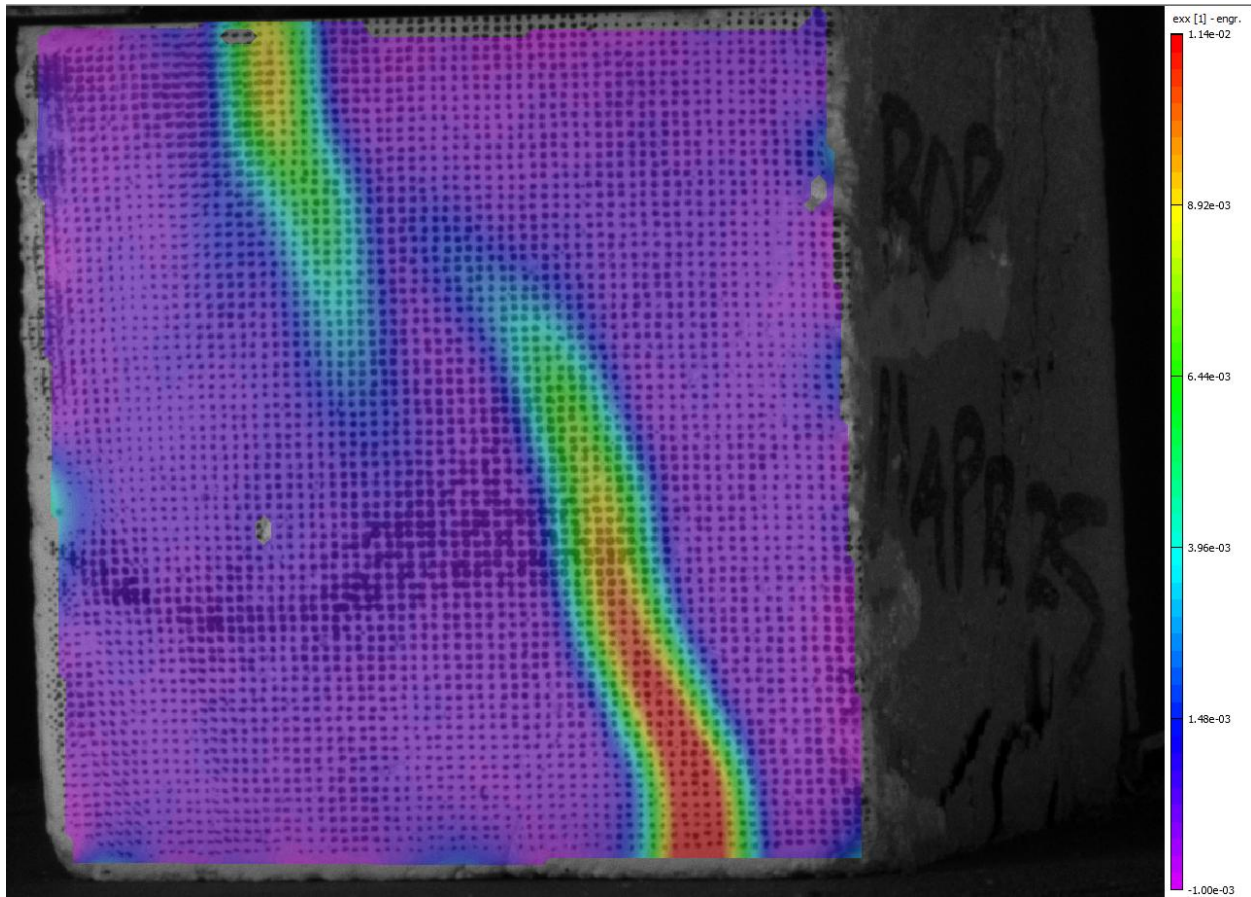


Fig. 5.6. The normal horizontal strain field for a cast cube.

Fig. 5.7 shows the strain field of a cube compressed in the direction of the Z axis, oriented as a 3DCP wall element would be (i.e., the vertical interlayer is perpendicular, and the adjacent interlayer is parallel, to the direction of loading) with one major axial splitting localization and two imperfections at the corners. This result demonstrates no clear influence of the printing process, as the vertical interlayers (which run horizontal in this image) do not show any increased strain.

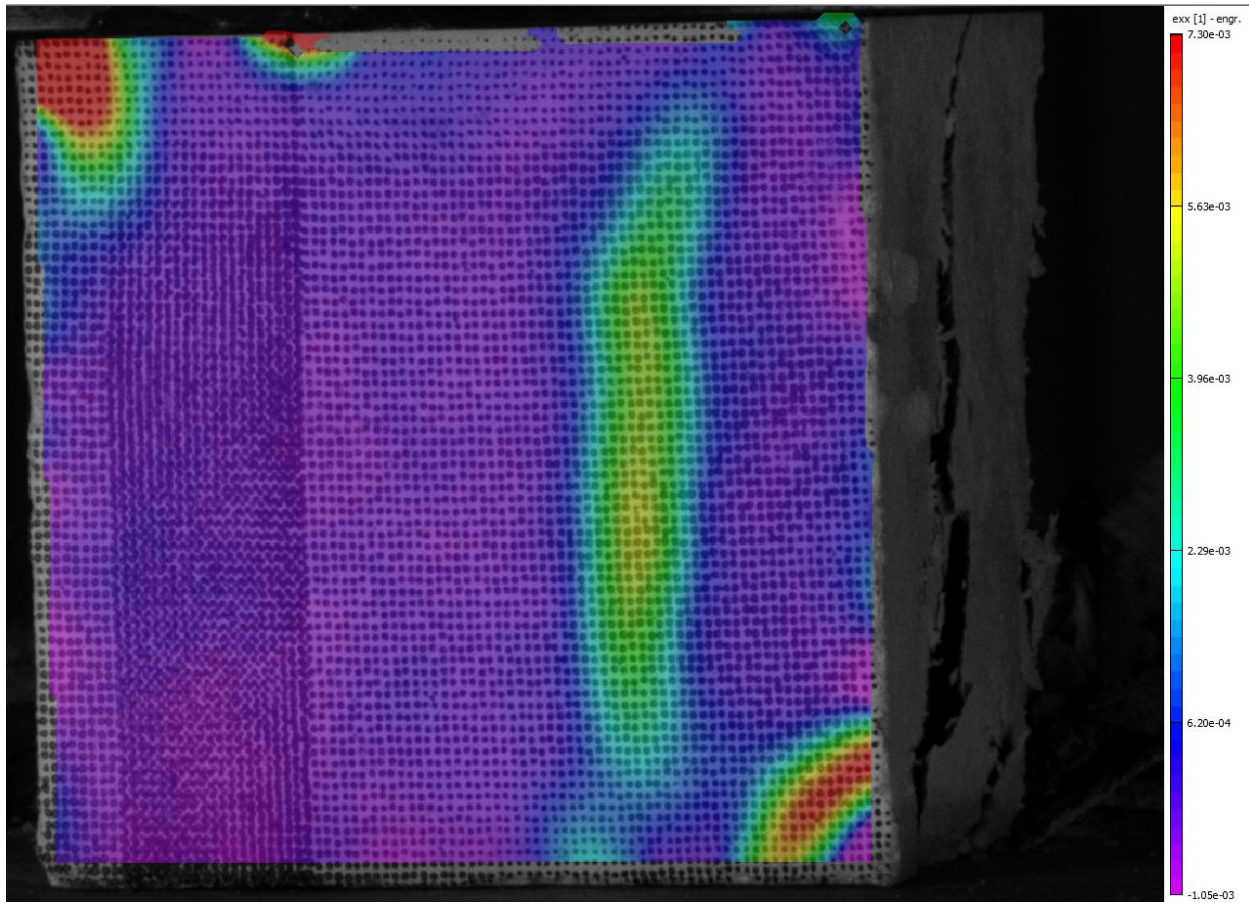


Fig. 5.7. The normal horizontal strain field for a printed cube with compression parallel to the Z axis. In Fig. 5.8, compression is applied parallel to the Y axis. Three axial splitting localizations appear to coalesce near the center of the cube's bottom face. In this orientation, the adjacent interlayers run vertically, so these localizations may coincide with these interlayers. Contrastingly, the vertical interlayers run horizontally and no localizations are shown in this direction. It is unclear if the failure mode here represents another instance of axial splitting with some shear inclinations or if the interlayers affect the failure.

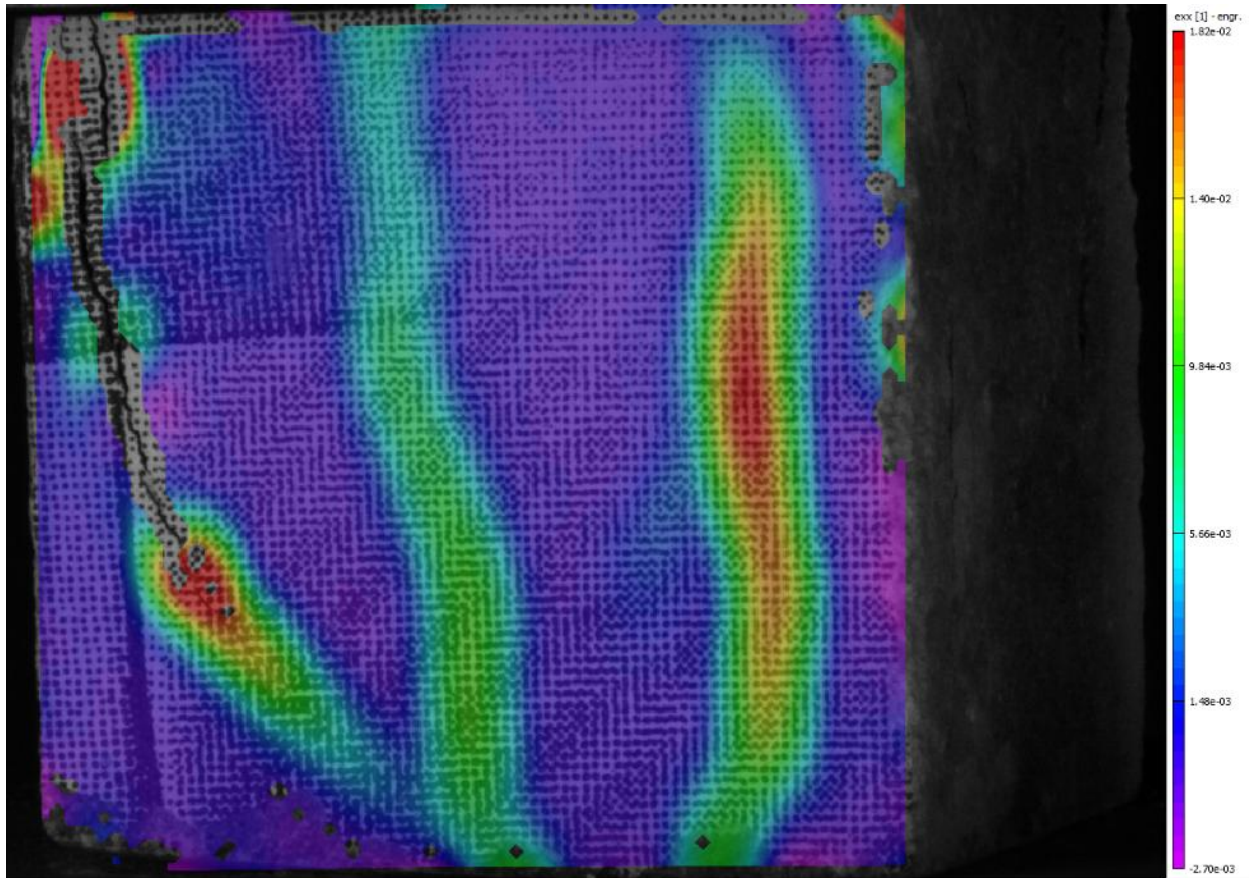


Fig. 5.8. The normal horizontal strain field for a printed cube with compression parallel to the Y axis. The failure modes of the compression specimens are all characteristic of typical mortar cubes; there is no difference in failure mode in the printed specimens as compared to those cast which can be readily attributed to effects of the printing process. This aligns with the compressive strengths of all specimens being similar at the 5% significance level.

5.5.2. Flexure

Fig. 5.9 shows a cast beam displaying localization of tensile strain at the extreme tension fiber near the midspan of the beam. While Euler-Bernoulli beam theory predicts a uniformly increasing stress with increasing moment (i.e., from the support to the midspan), the image shows a small area of increased strain with relatively constant strain elsewhere along the bottom

fiber. This is characteristic of the behavior of quasi-brittle materials, where a localized damage zone accompanies fracture propagation and subsequent failure.

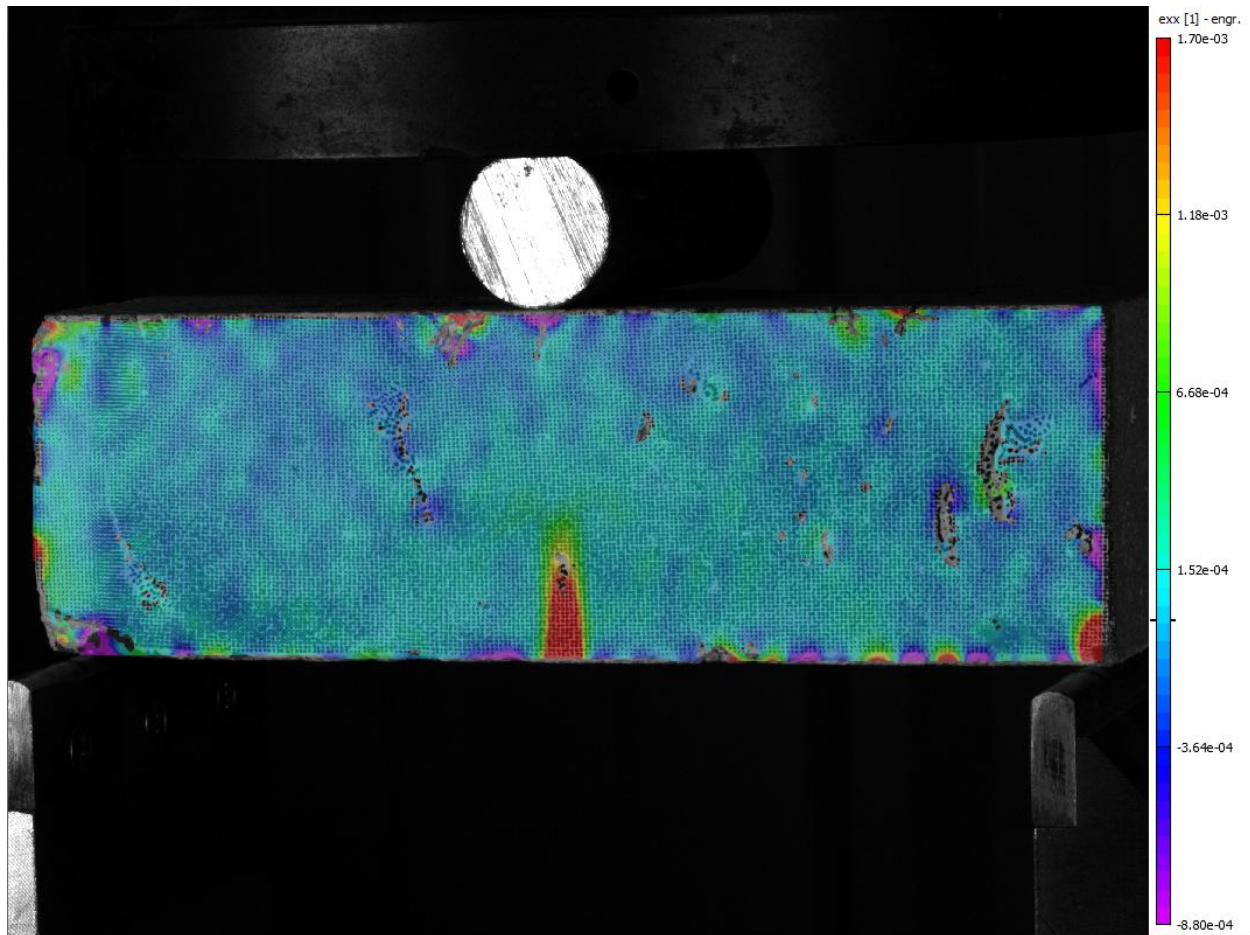


Fig. 5.9. The normal longitudinal strain field for a cast beam.

For bending about the X axis, as shown in Fig. 5.10, there is no interlayer region (either vertical or adjacent) which would be under tension—the printing direction aligns with the longitudinal direction of the beam. Therefore, it is expected that the failure mode of such a beam would align with that of the cast beams, which is demonstrated here, though a less well-defined damage zone is observed in this particular test.

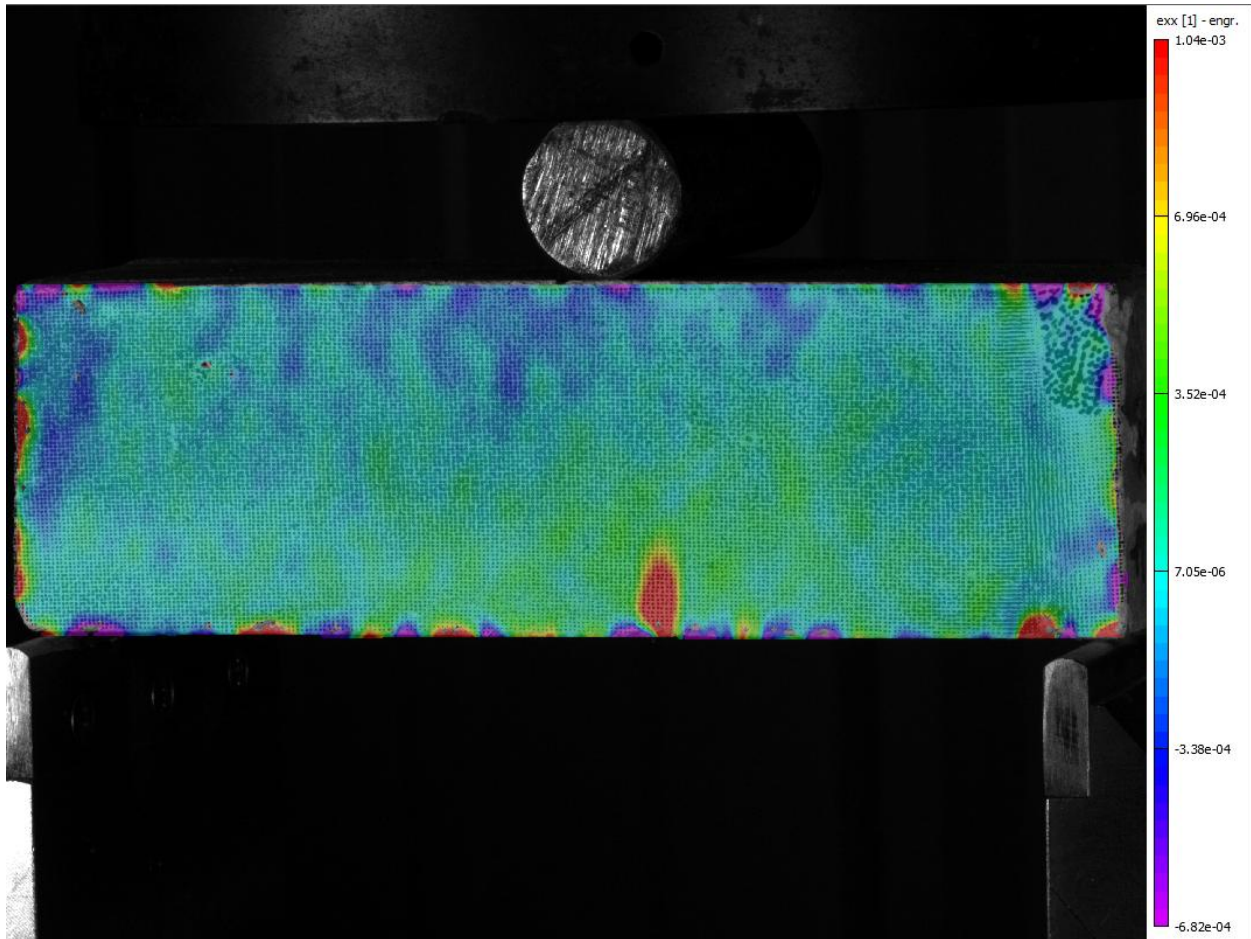


Fig. 5.10. The normal longitudinal strain field for a printed beam with bending about the X axis. When bending about the Y or Z axis, the adjacent or vertical interlayer region, respectively, is loaded in tension. For bending about the Y axis, Fig. 5.11 shows little damage on the tension face before failure, rather appearing to be controlled by crushing of the material under the load point. This may mean that the presence of the (adjacent) interlayer leads to a material with lower fracture resistance, in that it has less damage localization before total failure. However, for bending about the Z axis as shown in Fig. 5.12, the (vertical) interlayer does not appear to have the same effect—the behavior of this beam is similar to the cast specimen, and more generally, aligns with the predicted behavior of a homogenous section. It is possible that the vertical interlayer contains less voids than the adjacent interlayer due to vertical compaction pressure

induced by the nozzle during printing, though the 10% adjacent overlap, as detailed in Section 5.3.2, is meant to remedy this. Nonetheless, further repetition is required under different printing processes and loading conditions to determine the full extent of the effect of interlayer regions on failure modes in flexural loading.

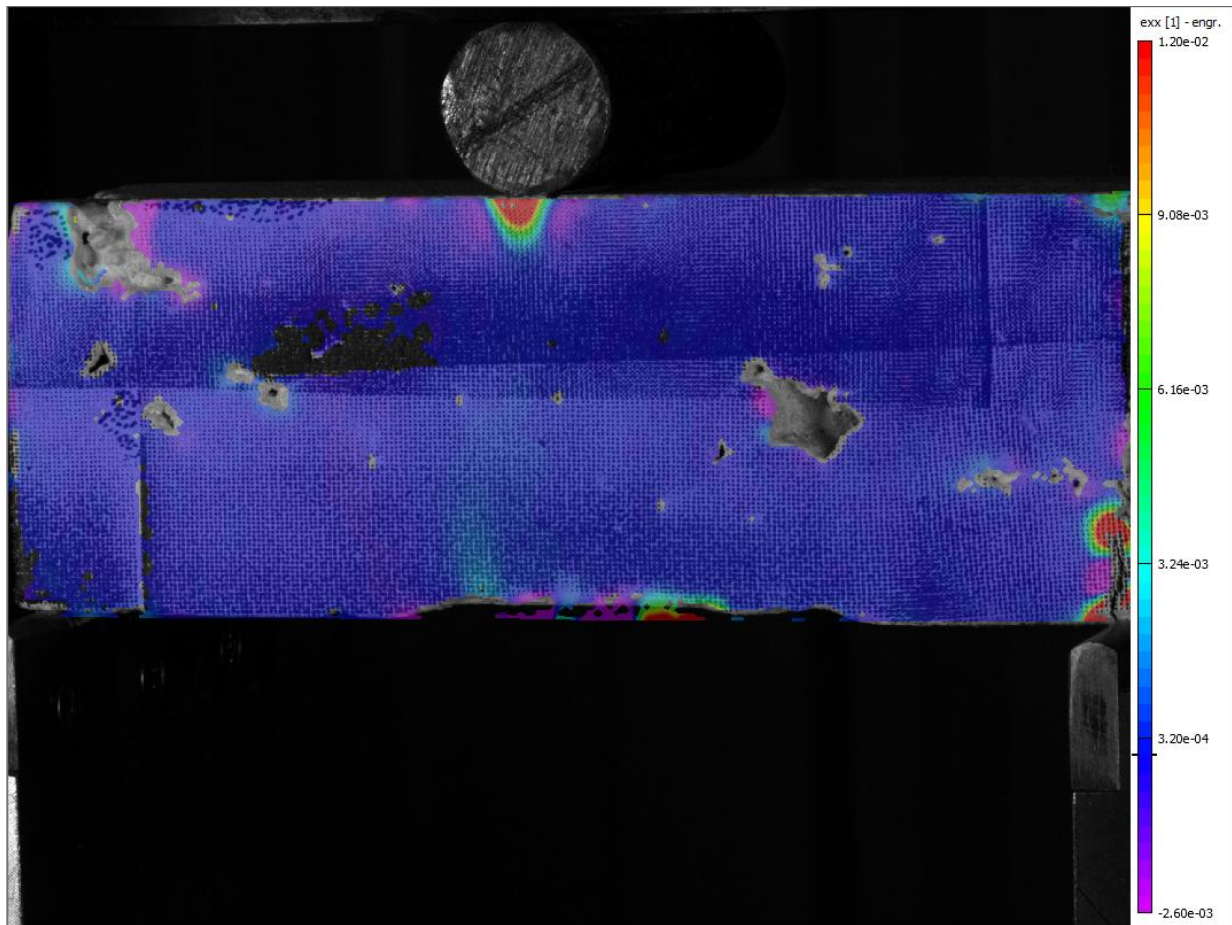


Fig. 5.11. The normal longitudinal strain field of a printed beam with bending about the Y axis.

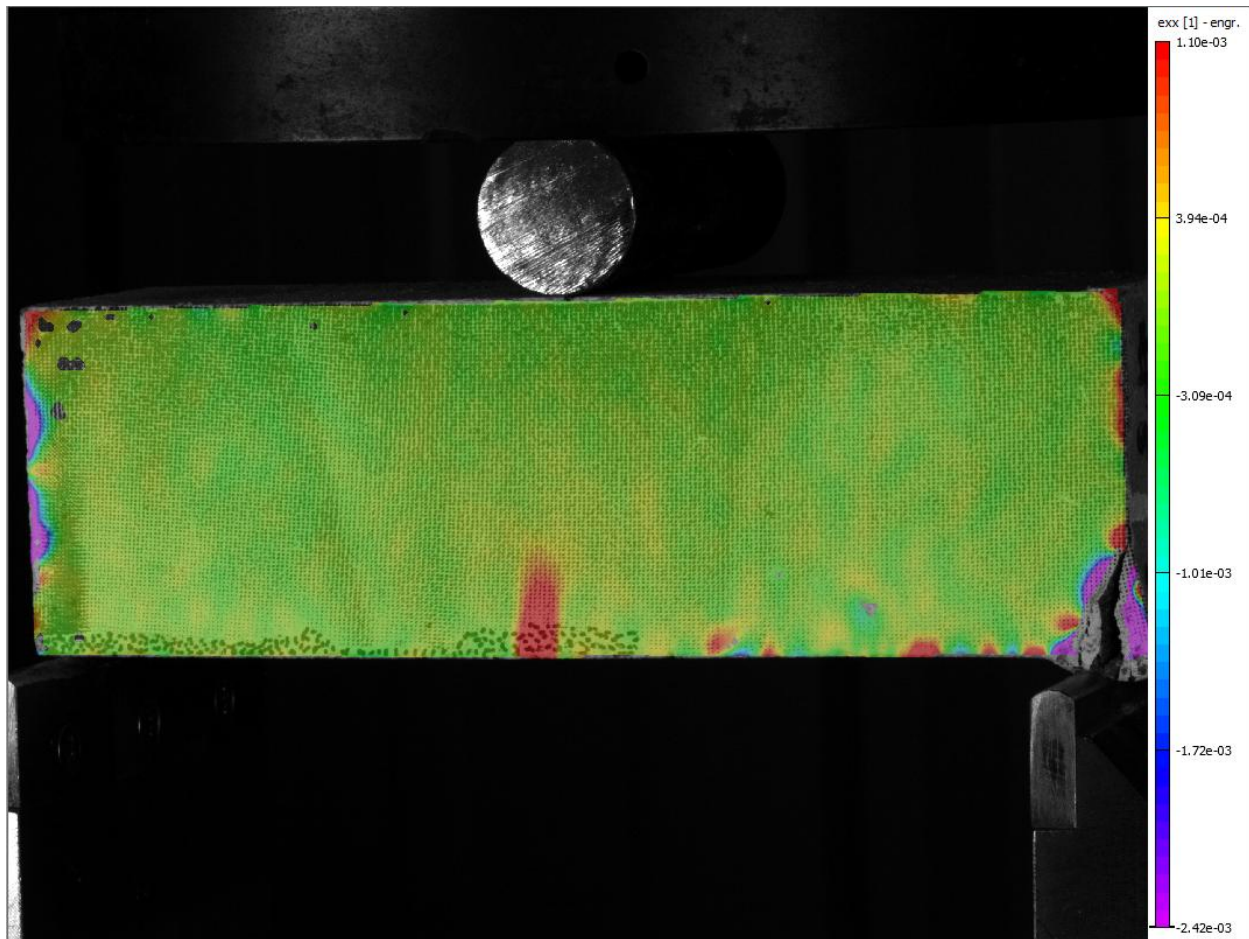


Fig. 5.12. The normal longitudinal strain field of a printed beam with bending about the Z axis.

5.6. Conclusions

This study evaluated the hardened-state mechanical performance of a printable cementitious material for a given printing system and suite of settings. Using digital image correlation, further insight is gained into the failure modes of the printed specimens based on their orientations, and as compared to cast controls. The present work largely found insignificant differences in the quantitative and qualitative properties between cast and printed specimens, or between different orientations of printed samples, except for two instances of reduced stiffness in printed samples as compared to cast. In the literature, mechanical inferiority due to printing or directional dependence are observed in widely varying degrees. This study may have mitigated such issues

by providing a 10% adjacent layer overlap and by maintaining very short interlayer pass times. With further experimentation, including varying printer settings designed to expose differences between mechanics of cast and printed specimens, more definite cause-effect relationships can be established that map features of the printing process to mechanical, phenomenological observations.

CHAPTER 6. CONCLUSIONS AND RECOMMENDATIONS

6.1. Conclusions

This work aims to elucidate fundamental mechanisms which govern the success of 3D concrete printing. By characterizing the material in the fresh and hardened states and across scales, the following questions have been addressed:

1. How does mechanical behavior (i.e., rheology) of cementitious materials in the fresh state relate to pumpability, extrudability, and buildability?
2. What are optimal formulations of plasticized, blended cement systems for successful printing?
3. How does the microstructure of printed mortars vary from conventionally cast counterparts, and how do these microstructure changes manifest on the macro-scale?
4. What are the differences in mechanical strength, stiffness, isotropy, and failure mechanisms between cast and printed mortars?

By pursuing these research goals, the viability of 3DCP as a construction technology is promoted. This allows for construction with reduced dependence on labor and reduced material consumption, promoting sustainability and economy. Additionally, by utilizing blended cement systems, sustainability can be further enhanced.

6.2. Recommendations for Practice

The results of this work demonstrate that 3DCP has many differences to conventional concrete construction, and thus many different considerations to assure quality. In the fresh state, requirements of material rheology are both stringent and difficult to achieve. This work, and the work of others, has shown promise in the use of clays to achieve suitable rheology. However,

when using clays, caution must be exhibited to avoid shear thickening. While one mixture in this research exhibited shear thickening, the other was extrudable—though with filament tearing. Further understanding of how filament tearing occurs and material formulations or additives which help mitigate it are crucial for practical success of this technology.

In service, the microstructural features of 3DCP discussed in this work may lead to poor durability compared to conventional concrete. While some researchers [230,231] have proposed techniques focused on mitigating the effect of the interlayer on fluid ingress, this work and the work of others [26] identifies microstructural anisotropy as an intrinsic phenomenon not solely governed by the interlayer region. This must be considered as allowing preferential paths for ingress of deleterious agents (from soil, deicing salt, etc.) and should be considered in the environmental exposure of 3DCP structures.

6.3. Recommendations for Future Work

Further work is still required to understand the behavior of concrete under and shortly after extrusion. The shearing which takes place in mixing and pumping must sufficiently destroy the microstructure to facilitate ease of extrusion, and the microstructure must rapidly reassemble to support the freshly printed element; materials and formulations thereof which promote this behavior of strong shear thinning yet rapid thixotropy will be key to robust, scalable 3DCP construction.

Moreover, for 3DCP to be viable in large-scale, heavy civil construction, the challenges associated with reinforcing it must be solved. Traditional reinforcing steel in 3DCP limits geometric complexity and is typically installed manually, either after printing or by interrupting printing. Questions remain concerning how much fiber reinforcement, nanoparticles, and other

mixture additives can replace rebar—partially or fully—and should be explored in future research. Relatedly, the automated placement of rebar or other discrete reinforcement in tandem with the printing process poses a potential solution.

REFERENCES

- [1] L. Gebhard, J. Mata-Falcón, R. Ammann, N. Preßmair, B. Kromoser, C. Menna, A. Baghdadi, H. Kloft, M. Gabriel, M. Walch, W. Kaufmann, Enhancing structural efficiency with digital concrete – Principles, opportunities and case studies, *Cem. Concr. Res.* 185 (2024). <https://doi.org/10.1016/j.cemconres.2024.107645>.
- [2] K.L. Scrivener, V.M. John, E.M. Gartner, Eco-efficient cements: Potential economically viable solutions for a low-CO₂ cement-based materials industry, *Cem. Concr. Res.* 114 (2018) 2–26. <https://doi.org/10.1016/j.cemconres.2018.03.015>.
- [3] B. Khoshnevis, Automated construction by contour crafting—related robotics and information technologies, *Autom. Constr.* 13 (2004) 5–19. <https://doi.org/10.1016/J.AUTCON.2003.08.012>.
- [4] F. Bos, R. Wolfs, Z. Ahmed, T. Salet, Large Scale Testing of Digitally Fabricated Concrete (DFC) Elements, in: T. Wangler, R.J. Flatt (Eds.), 2019: pp. 129–147. https://doi.org/10.1007/978-3-319-99519-9_12.
- [5] F.P. Bos, C. Menna, M. Pradena, E. Kreiger, W.R.L. da Silva, A.U. Rehman, D. Weger, R.J.M. Wolfs, Y. Zhang, L. Ferrara, V. Mechtcherine, The realities of additively manufactured concrete structures in practice, *Cem. Concr. Res.* 156 (2022) 106746. <https://doi.org/10.1016/j.cemconres.2022.106746>.
- [6] T.T. Le, S.A. Austin, S. Lim, R.A. Buswell, A.G.F. Gibb, T. Thorpe, Mix design and fresh properties for high-performance printing concrete, *Materials and*

- Structures/Materiaux et Constructions 45 (2012) 1221–1232.
<https://doi.org/10.1617/S11527-012-9828-Z/FIGURES/16>.
- [7] M.K. Mohan, A. V. Rahul, G. De Schutter, K. Van Tittelboom, Extrusion-based concrete 3D printing from a material perspective: A state-of-the-art review, *Cem. Concr. Compos.* 115 (2021) 103855.
<https://doi.org/10.1016/J.CEMCONCOMP.2020.103855>.
- [8] K. Scrivener, F. Martirena, S. Bishnoi, S. Maity, Calcined clay limestone cements (LC3), *Cem. Concr. Res.* 114 (2018) 49–56.
<https://doi.org/10.1016/j.cemconres.2017.08.017>.
- [9] D. Marchon, S. Kawashima, H. Bessaies-Bey, S. Mantellato, S. Ng, Hydration and rheology control of concrete for digital fabrication: Potential admixtures and cement chemistry, *Cem. Concr. Res.* 112 (2018) 96–110.
<https://doi.org/10.1016/J.CEMCONRES.2018.05.014>.
- [10] H. Kloft, B. Sawicki, F. Bos, R. Dörrie, N. Freund, S. Gantner, L. Gebhard, N. Hack, E. Ivaniuk, J. Kruger, W. Kaufmann, J. Mata-Falcón, V. Mechtcherine, A. Mirjan, R. Wolfs, D. Lowke, Interaction of reinforcement, process, and form in Digital Fabrication with Concrete, *Cem. Concr. Res.* 186 (2024) 107640.
<https://doi.org/10.1016/j.cemconres.2024.107640>.
- [11] R. Wolfs, The status quo of 3D concrete printing: are we there yet?, *RILEM Technical Letters* (2023). <https://doi.org/10.21809/rilemtechlett.2023.197>.

- [12] R.A. Buswell, W.R. Leal de Silva, S.Z. Jones, J. Dirrenberger, 3D printing using concrete extrusion: A roadmap for research, *Cem. Concr. Res.* 112 (2018) 37–49. <https://doi.org/10.1016/j.cemconres.2018.05.006>.
- [13] R. Wolfs, D. Bos, J.F. Caron, M. Gerke, R. Mesnil, R. Buswell, N. Ducoulombier, N. Hack, E. Keita, P. Kinnell, K. Mawas, V. Mechtcherine, L. Miranda, D. Sokolov, J. Versteeg, N. Roussel, On-line and in-line quality assessment across all scale levels of 3D concrete printing, *Cem. Concr. Res.* 185 (2024). <https://doi.org/10.1016/j.cemconres.2024.107646>.
- [14] M. Kreiger, E. Kreiger, S. Mansour, S. Monkman, M.A. Delavar, P. Sideris, C. Roberts, M. Friedell, S. Platt, S. Jones, Additive construction in practice – Realities of acceptance criteria, *Cem. Concr. Res.* 186 (2024). <https://doi.org/10.1016/j.cemconres.2024.107652>.
- [15] F. Brun, F. Gaspar, A. Mateus, J. Vitorino, F. Diz, Experimental Study on 3D Printing of Concrete with Overhangs, in: 2020: pp. 778–789. https://doi.org/10.1007/978-3-030-49916-7_77.
- [16] A. Anton, L. Reiter, T. Wangler, V. Frangez, R.J. Flatt, B. Dillenburger, A 3D concrete printing prefabrication platform for bespoke columns, *Autom. Constr.* 122 (2021) 103467. <https://doi.org/10.1016/J.AUTCON.2020.103467>.
- [17] O. Ozturk, C. Lunsford, J. Strait, S.D. Nair, Breaking barriers in underwater construction: A two-stage 3D printing system with on-demand material adaptation, *Cem. Concr. Compos.* 164 (2025). <https://doi.org/10.1016/j.cemconcomp.2025.106306>.

- [18] L. Reiter, T. Wangler, A. Anton, R.J. Flatt, Setting on demand for digital concrete – Principles, measurements, chemistry, validation, *Cem. Concr. Res.* 132 (2020) 106047. <https://doi.org/10.1016/j.cemconres.2020.106047>.
- [19] H.F. Brinson, L.C. Brinson, *Polymer Engineering Science and Viscoelasticity*, 2nd ed., New York, 2015. <https://doi.org/10.1007/978-1-4899-7485-3>.
- [20] M. Sonebi, D. Feys, RILEM State-of-the-Art Reports Measuring Rheological Properties of Cement-based Materials State-of-the-Art Report of the RILEM Technical Committee 266-MRP, n.d. www.RILEM.net.
- [21] T.G. Mezger, *The Rheology Handbook*, 2nd ed., Hannover, 2006.
- [22] J.T. Kolawole, W.P. Boshoff, A.J. Babafemi, R. Combrinck, Shear and viscoelastic properties of early-age concrete using small-amplitude and low-rate rheometry – From fresh state to initial set, *Cem. Concr. Compos.* 124 (2021). <https://doi.org/10.1016/j.cemconcomp.2021.104223>.
- [23] N. Roussel, D. Lowke, RILEM State-of-the-Art Reports Digital Fabrication with Cement-Based Materials State-of-the-Art Report of the RILEM TC 276-DFC, n.d. <https://link.springer.com/bookseries/8780>.
- [24] R. Moini, J. Olek, P.D. Zavattieri, J.P. Youngblood, Early-age buildability-rheological properties relationship in additively manufactured cement paste hollow cylinders, *Cem. Concr. Compos.* 131 (2022). <https://doi.org/10.1016/j.cemconcomp.2022.104538>.

- [25] A. Perrot, D. Rangeard, A. Pierre, Structural built-up of cement-based materials used for 3D-printing extrusion techniques, *Materials and Structures/Materiaux et Constructions* 49 (2016) 1213–1220. <https://doi.org/10.1617/s11527-015-0571-0>.
- [26] J.T. Kolawole, R. Buswell, S. Mahmood, M.N. Isa, S. Cavalaro, S. Austin, D. Engelberg, J. Dobrzanski, J. Xu, P.J. Withers, On the origins of anisotropy of extrusion-based 3D printed concrete: The roles of filament skin and agglomeration, *Cem. Concr. Res.* 192 (2025). <https://doi.org/10.1016/j.cemconres.2025.107817>.
- [27] T. Wangler, E. Lloret, L. Reiter, N. Hack, F. Gramazio, M. Kohler, M. Bernhard, B. Dillenburger, J. Buchli, N. Roussel, R. Flatt, Digital concrete: Opportunities and challenges, *RILEM Technical Letters* 1 (2016) 67–75. <https://doi.org/10.21809/rilemtechlett.2016.16>.
- [28] T.S. Rushing, P.B. Stynoski, L.A. Barna, G.K. Al-Chaar, J.F. Burroughs, J.D. Shannon, M.A. Kreiger, M.P. Case, Investigation of Concrete Mixtures for Additive Construction, in: *3D Concrete Printing Technology*, Elsevier, 2019: pp. 137–160. <https://doi.org/10.1016/B978-0-12-815481-6.00007-5>.
- [29] A. V. Rahul, M. Santhanam, H. Meena, Z. Ghani, 3D printable concrete: Mixture design and test methods, *Cem. Concr. Compos.* 97 (2019) 13–23. <https://doi.org/10.1016/J.CEMCONCOMP.2018.12.014>.
- [30] A. Kazemian, X. Yuan, E. Cochran, B. Khoshnevis, Cementitious materials for construction-scale 3D printing: Laboratory testing of fresh printing mixture, *Constr. Build. Mater.* 145 (2017) 639–647. <https://doi.org/10.1016/J.CONBUILDMAT.2017.04.015>.

- [31] S. Hou, Z. Duan, J. Xiao, J. Ye, A review of 3D printed concrete: Performance requirements, testing measurements and mix design, *Constr. Build. Mater.* 273 (2021) 121745. <https://doi.org/10.1016/J.CONBUILDMAT.2020.121745>.
- [32] S. Paritala, K.K. Singaram, I. Bathina, M.A. Khan, S.K.R. Jyosyula, Rheology and pumpability of mix suitable for extrusion-based concrete 3D printing – A review, *Constr. Build. Mater.* 402 (2023).
<https://doi.org/10.1016/j.conbuildmat.2023.132962>.
- [33] M.K. Mohan, A. V. Rahul, K. Van Tittelboom, G. De Schutter, Rheological and pumping behaviour of 3D printable cementitious materials with varying aggregate content, *Cem. Concr. Res.* 139 (2021).
<https://doi.org/10.1016/j.cemconres.2020.106258>.
- [34] A.R. Arunothayan, B. Nematollahi, R. Ranade, S.H. Bong, J. Sanjayan, Development of 3D-printable ultra-high performance fiber-reinforced concrete for digital construction, *Constr. Build. Mater.* 257 (2020) 119546.
<https://doi.org/10.1016/J.CONBUILDMAT.2020.119546>.
- [35] Y. Weng, M. Li, M.J. Tan, S. Qian, Design 3D printing cementitious materials via Fuller Thompson theory and Marson-Percy model, *Constr. Build. Mater.* 163 (2018) 600–610. <https://doi.org/10.1016/J.CONBUILDMAT.2017.12.112>.
- [36] Z. Malaeb, F. AlSakka, F. Hamzeh, 3D Concrete Printing, in: *3D Concrete Printing Technology*, Elsevier, 2019: pp. 115–136. <https://doi.org/10.1016/B978-0-12-815481-6.00006-3>.

- [37] Y. Chen, S. Chaves Figueiredo, Z. Li, Z. Chang, K. Jansen, O. Çopuroğlu, E. Schlangen, Improving printability of limestone-calcined clay-based cementitious materials by using viscosity-modifying admixture, *Cem. Concr. Res.* 132 (2020) 106040. <https://doi.org/10.1016/j.cemconres.2020.106040>.
- [38] J. Reinold, V.N. Nerella, V. Mechtcherine, G. Meschke, Extrusion process simulation and layer shape prediction during 3D-concrete-printing using the Particle Finite Element Method, *Autom. Constr.* 136 (2022) 104173. <https://doi.org/10.1016/J.AUTCON.2022.104173>.
- [39] I. Ivanova, E. Ivaniuk, S. Bisetti, V.N. Nerella, V. Mechtcherine, Comparison between methods for indirect assessment of buildability in fresh 3D printed mortar and concrete, *Cem. Concr. Res.* 156 (2022). <https://doi.org/10.1016/j.cemconres.2022.106764>.
- [40] M. Mahmoudi, T. Wangler, R.J. Flatt, Robustness of Digital Concrete: Effects of Temperature, Accelerator Type and Dosage, in: *RILEM Bookseries*, Springer Science and Business Media B.V., 2024: pp. 209–216. https://doi.org/10.1007/978-3-031-70031-6_25.
- [41] T. Wangler, Y. Tao, A. Das, M. Mahmoudi, S. Gürel, R.J. Flatt, Aluminate 2K systems in digital concrete: Process, design, chemistry, and outlook, *Cem. Concr. Res.* 185 (2024). <https://doi.org/10.1016/j.cemconres.2024.107644>.
- [42] N. Roussel, Rheological requirements for printable concretes, *Cem. Concr. Res.* 112 (2018) 76–85. <https://doi.org/10.1016/J.CEMCONRES.2018.04.005>.

- [43] P. Jousset, D. Lootens, N. Roussel, R.J. Flatt, Rheology of penetrations tests I: theory and finite element simulations, in: 12th International Congress on the Chemistry of Cement, Montreal, 2007.
- [44] D. Lootens, R.J. Flatt, N. Roussel, Rheology of penetrations tests II: penetrometers, Vicat and Hilti needles, in: 12th International Congress on the Chemistry of Cement, Montreal, 2007.
- [45] N. Roussel, H. Bessaies-Bey, S. Kawashima, D. Marchon, K. Vasilic, R. Wolfs, Recent advances on yield stress and elasticity of fresh cement-based materials, *Cem. Concr. Res.* 124 (2019). <https://doi.org/10.1016/j.cemconres.2019.105798>.
- [46] S. Ma, Y. Qian, S. Kawashima, Experimental and modeling study on the non-linear structural build-up of fresh cement pastes incorporating viscosity modifying admixtures, *Cem. Concr. Res.* 108 (2018) 1–9.
<https://doi.org/10.1016/j.cemconres.2018.02.022>.
- [47] R.J. Flatt, T. Wangler, On sustainability and digital fabrication with concrete, *Cem. Concr. Res.* 158 (2022) 106837.
<https://doi.org/10.1016/J.CEMCONRES.2022.106837>.
- [48] D. Feys, G. De Schutter, S. Fataei, N.S. Martys, V. Mechtcherine, Pumping of concrete: Understanding a common placement method with lots of challenges, *Cem. Concr. Res.* 154 (2022) 106720.
<https://doi.org/10.1016/j.cemconres.2022.106720>.

- [49] Y. Liu, R. Jing, F. Cao, P. Yan, Effects of aggregate content on rheological properties of lubrication layer and pumping concrete, *ACI Mater. J.* 118 (2021) 7–18. <https://doi.org/10.14359/51734147>.
- [50] T. Tavangar, M. Hosseinpoor, A. Yahia, K.H. Khayat, Computational investigation of concrete pipe flow: Critical review, *ACI Mater. J.* 118 (2021) 203–215. <https://doi.org/10.14359/51733124>.
- [51] W.R. Leal da Silva, H. Fryda, J.N. Bousseau, P.A. Andreani, T.J. Andersen, Evaluation of early-age concrete structural build-up for 3D concrete printing by oscillatory rheometry, in: *Advances in Intelligent Systems and Computing*, Springer Verlag, 2020: pp. 35–47. https://doi.org/10.1007/978-3-030-20216-3_4.
- [52] F.B. Rodriguez, J. Olek, R. Moini, P.D. Zavattieri, J.P. Youngblood, Linking Solids Content and Flow Properties of Mortars to their Three-Dimensional Printing Characteristics, *ACI Mater. J.* 118 (2021) 371–382. <https://doi.org/10.14359/51733136>.
- [53] Y.W.D. Tay, Y. Qian, M.J. Tan, Printability region for 3D concrete printing using slump and slump flow test, *Compos. B Eng.* 174 (2019). <https://doi.org/10.1016/j.compositesb.2019.106968>.
- [54] D. Feys, How much is bulk concrete sheared during pumping?, *Constr. Build. Mater.* 223 (2019) 341–351. <https://doi.org/10.1016/j.conbuildmat.2019.06.224>.
- [55] D. Kaplan, F. de Larrard, T. Sedran, Design of Concrete Pumping Circuit, *ACI Mater. J.* 102 (2005). <https://doi.org/10.14359/14304>.

- [56] L. Yang, S.M.E. Sepasgozar, S. Shirowzhan, A. Kashani, D. Edwards, Nozzle criteria for enhancing extrudability, buildability and interlayer bonding in 3D printing concrete, *Autom. Constr.* 146 (2023) 104671.
<https://doi.org/10.1016/j.autcon.2022.104671>.
- [57] J. Kruger, S. Zeranka, G. van Zijl, A rheology-based quasi-static shape retention model for digitally fabricated concrete, *Constr. Build. Mater.* 254 (2020) 119241.
<https://doi.org/10.1016/J.CONBUILDMAT.2020.119241>.
- [58] J. Kruger, S. Cho, S. Zeranka, C. Viljoen, G. van Zijl, 3D concrete printer parameter optimisation for high rate digital construction avoiding plastic collapse, *Compos. B Eng.* 183 (2020). <https://doi.org/10.1016/j.compositesb.2019.107660>.
- [59] D.P. Bentz, C.F. Ferraris, M.A. Galler, A.S. Hansen, J.M. Guynn, Influence of particle size distributions on yield stress and viscosity of cement-fly ash pastes, *Cem. Concr. Res.* 42 (2012) 404–409.
<https://doi.org/10.1016/j.cemconres.2011.11.006>.
- [60] R.J.M. Wolfs, F.P. Bos, T.A.M. Salet, Early age mechanical behaviour of 3D printed concrete: Numerical modelling and experimental testing, *Cem. Concr. Res.* 106 (2018) 103–116. <https://doi.org/10.1016/j.cemconres.2018.02.001>.
- [61] Test Method for Unconfined Compressive Strength of Cohesive Soil, ASTM D2166 (2024). https://doi.org/10.1520/D2166_D2166M-24.
- [62] Test Method for Direct Shear Test of Soils Under Consolidated Drained Conditions, ASTM D3080 (2023). https://doi.org/10.1520/D3080_D3080M-23.

- [63] Test Method for Unconsolidated-Undrained Triaxial Compression Test on Cohesive Soils, ASTM D2850 (2024). <https://doi.org/10.1520/D2850-24>.
- [64] R.J.M. Wolfs, F.P. Bos, T.A.M. Salet, Triaxial compression testing on early age concrete for numerical analysis of 3D concrete printing, *Cem. Concr. Compos.* 104 (2019). <https://doi.org/10.1016/j.cemconcomp.2019.103344>.
- [65] C. Negrón-McFarlan, E. Kreiger, L. Barna, P. Stynoski, M. Kreiger, Development of In-Place Test Methods for Evaluating Printable Concretes, *ACI Mater. J.* 121 (2024) 59–72. <https://doi.org/10.14359/51740265>.
- [66] H. Liu, T. Ding, J. Xiao, V. Mechtcherine, Buildability prediction of 3D–printed concrete at early-ages: A numerical study with Drucker–Prager model, *Addit. Manuf.* 55 (2022). <https://doi.org/10.1016/j.addma.2022.102821>.
- [67] A.S.J. Suiker, Mechanical performance of wall structures in 3D printing processes: Theory, design tools and experiments, *Int. J. Mech. Sci.* 137 (2018) 145–170. <https://doi.org/10.1016/j.ijmecsci.2018.01.010>.
- [68] A.S.J. Suiker, R.J.M. Wolfs, S.M. Lucas, T.A.M. Salet, Elastic buckling and plastic collapse during 3D concrete printing, *Cem. Concr. Res.* 135 (2020). <https://doi.org/10.1016/j.cemconres.2020.106016>.
- [69] G. Duarte, J.P. Duarte, A. Memari, N. Brown, J.P. Gevaudan, Towards a model for structural performance in concrete printing based on buildability and toolpath design, *Journal of Building Engineering* 69 (2023). <https://doi.org/10.1016/j.jobbe.2023.106325>.

- [70] V. Nguyen-Van, H. Nguyen-Xuan, B. Panda, P. Tran, 3D concrete printing modelling of thin-walled structures, *Structures* 39 (2022) 496–511.
<https://doi.org/10.1016/j.istruc.2022.03.049>.
- [71] A.U. Rehman, I.-G. Kim, J.-H. Kim, Exploring the Impact of the Pumping Process on the Structural Build-up in the Context of 3D Concrete Printing, (n.d.).
<https://doi.org/10.24355/dbbs.084-202408151202-0>.
- [72] K. Sriram Kompella, A. Marcucci, F. Lo Monte, M. Levi, L. Ferrara, Fracture Behavior of Three-Dimensional-Printable Cementitious Mortars in Very Early Ages and Hardened States, *ACI Mater. J.* 121 (2024).
<https://doi.org/10.14359/51740302>.
- [73] A. Marcucci, S.K. Kompella, F. Lo Monte, M. Levi, L. Ferrara, Early Age Shear and Tensile Fracture Properties of 3D Printable Cementitious Mortar to Assess Printability Window, in: *RILEM Bookseries*, Springer Science and Business Media B.V., 2022: pp. 337–342. https://doi.org/10.1007/978-3-031-06116-5_50.
- [74] N. Ducoulombier, R. Mesnil, P. Carneau, L. Demont, H. Bessaies-Bey, J.F. Caron, N. Roussel, The “Slugs-test” for extrusion-based additive manufacturing: Protocol, analysis and practical limits, *Cem. Concr. Compos.* 121 (2021).
<https://doi.org/10.1016/j.cemconcomp.2021.104074>.
- [75] D. Bos, S. Lucas, J. Blaakmeer, T. Salet, R. Wolfs, Development of the On-Line Gravity-Induced Compression Test: “The Inverse Slugs Test,” in: *RILEM Bookseries*, Springer Science and Business Media B.V., 2024: pp. 166–173.
https://doi.org/10.1007/978-3-031-70031-6_20.

- [76] R. Nicolas, B. Richard, D. Nicolas, I. Irina, K.J. Temitope, L. Dirk, M. Viktor, M. Romain, P. Arnaud, P. Ursula, R. Lex, S. Dietmar, W. Timothy, W. Rob, Z. Wenqiang, Assessing the fresh properties of printable cement-based materials: High potential tests for quality control, *Cem. Concr. Res.* 158 (2022).
<https://doi.org/10.1016/j.cemconres.2022.106836>.
- [77] A.U. Rehman, A. Perrot, B.M. Birru, J.H. Kim, Recommendations for quality control in industrial 3D concrete printing construction with mono-component concrete: A critical evaluation of ten test methods and the introduction of the performance index, *Developments in the Built Environment* 16 (2023).
<https://doi.org/10.1016/j.dibe.2023.100232>.
- [78] A. Das, L. Reiter, S. Mantellato, R.J. Flatt, Early-age rheology and hydration control of ternary binders for 3D printing applications, *Cem. Concr. Res.* 162 (2022). <https://doi.org/10.1016/j.cemconres.2022.107004>.
- [79] Test Method for Flow of Hydraulic Cement Mortar, ASTM C1437 (n.d.).
<https://doi.org/10.1520/C1437>.
- [80] R.J.M. Wolfs, F.P. Bos, T.A.M. Salet, Correlation between destructive compression tests and non-destructive ultrasonic measurements on early age 3D printed concrete, *Constr. Build. Mater.* 181 (2018) 447–454.
<https://doi.org/10.1016/j.conbuildmat.2018.06.060>.
- [81] Test Method for Time of Setting of Hydraulic Cement Mortar by Modified Vicat Needle, ASTM C807 (2021). <https://doi.org/10.1520/C0807-21>.

- [82] L. Nachbaur, J.C. Mutin, A. Nonat, L. Choplin, Dynamic mode rheology of cement and tricalcium silicate pastes from mixing to setting, n.d.
- [83] A. Das, C. Wenger, L. Walpen, R.J. Flatt, Early-age hydration of accelerated low-carbon cements for digital fabrication, *Cem. Concr. Compos.* 159 (2025).
<https://doi.org/10.1016/j.cemconcomp.2025.105991>.
- [84] S. Mantellato, M. Palacios, R.J. Flatt, Relating early hydration, specific surface and flow loss of cement pastes, *Materials and Structures/Materiaux et Constructions* 52 (2019). <https://doi.org/10.1617/s11527-018-1304-y>.
- [85] T. Zat, E.S. Duarte, J. Webber, P.R. De Matos, E.D. Rodríguez, Comparison between yield stress measurements for fiber-reinforced 3D concrete printing, (n.d.).
<https://doi.org/10.24355/dbbs.084-202408161106-0>.
- [86] L. Esposito, L. Casagrande, C. Menna, D. Asprone, F. Auricchio, Early-age creep behaviour of 3D printable mortars: Experimental characterisation and analytical modelling, *Materials and Structures/Materiaux et Constructions* 54 (2021).
<https://doi.org/10.1617/s11527-021-01800-z>.
- [87] K. Xia, Y. Chen, Y. Chen, Z. Jia, L. Jia, Y. Gao, Y. Zhang, Understanding and modeling the plastic deformation of 3D printed concrete based on viscoelastic creep behavior, *Addit. Manuf.* 84 (2024). <https://doi.org/10.1016/j.addma.2024.104132>.
- [88] I. Mehdipour, K.H. Khayat, Understanding the role of particle packing characteristics in rheo-physical properties of cementitious suspensions: A literature review, *Constr. Build. Mater.* 161 (2018) 340–353.
<https://doi.org/10.1016/j.conbuildmat.2017.11.147>.

- [89] I. Mehdipour, K.H. Khayat, Effect of particle-size distribution and specific surface area of different binder systems on packing density and flow characteristics of cement paste, *Cem. Concr. Compos.* 78 (2017) 120–131.
<https://doi.org/10.1016/j.cemconcomp.2017.01.005>.
- [90] J. Yammine, M. Chaouche, M. Guerinet, M. Moranville, N. Roussel, From ordinary rheology concrete to self compacting concrete: A transition between frictional and hydrodynamic interactions, *Cem. Concr. Res.* 38 (2008) 890–896.
<https://doi.org/10.1016/j.cemconres.2008.03.011>.
- [91] G. Sant, C.F. Ferraris, J. Weiss, Rheological properties of cement pastes: A discussion of structure formation and mechanical property development, *Cem. Concr. Res.* 38 (2008) 1286–1296.
<https://doi.org/10.1016/j.cemconres.2008.06.008>.
- [92] Y. Chen, Y. Zhang, B. Pang, Z. Liu, G. Liu, Extrusion-based 3D printing concrete with coarse aggregate: Printability and direction-dependent mechanical performance, *Constr. Build. Mater.* 296 (2021).
<https://doi.org/10.1016/j.conbuildmat.2021.123624>.
- [93] I.M. Krieger, T.J. Dougherty, A Mechanism for Non-Newtonian Flow in Suspensions of Rigid Spheres, *Transactions of the Society of Rheology* 3 (1959) 137–152. <https://doi.org/10.1122/1.548848>.
- [94] X. Chateau, G. Ovarlez, K.L. Trung, Homogenization approach to the behavior of suspensions of noncolloidal particles in yield stress fluids, *J. Rheol. (N Y. N. Y.)* 52 (2008) 489–506. <https://doi.org/10.1122/1.2838254>.

- [95] F. Mahaut, S. Mokéddem, X. Chateau, N. Roussel, G. Ovarlez, Effect of coarse particle volume fraction on the yield stress and thixotropy of cementitious materials, *Cem. Concr. Res.* 38 (2008) 1276–1285.
<https://doi.org/10.1016/j.cemconres.2008.06.001>.
- [96] V. De Bono, N. Ducoulombier, R. Mesnil, J.F. Caron, Methodology for formulating low-carbon printable mortar through particles packing optimization, *Cem. Concr. Res.* 176 (2024). <https://doi.org/10.1016/j.cemconres.2023.107403>.
- [97] W.J. Long, C. Lin, J.L. Tao, T.H. Ye, Y. Fang, Printability and particle packing of 3D-printable limestone calcined clay cement composites, *Constr. Build. Mater.* 282 (2021). <https://doi.org/10.1016/j.conbuildmat.2021.122647>.
- [98] L. Du, J. Zhou, J. Lai, K. Wu, X. Yin, Y. He, Effect of pore structure on durability and mechanical performance of 3D printed concrete, *Constr. Build. Mater.* 400 (2023) 132581. <https://doi.org/10.1016/j.conbuildmat.2023.132581>.
- [99] B. Shantanu, J. Smrati, S. Manu, Criticality of binder-aggregate interaction for buildability of 3D printed concrete containing limestone calcined clay, *Cem. Concr. Compos.* 136 (2023). <https://doi.org/10.1016/j.cemconcomp.2022.104853>.
- [100] Y. Jacquet, S. Kawashima, J. Spangenberg, Unveiling the structural build-up 3D printable cement-based materials: From small amplitude oscillatory shear (SAOS) to extensional (SAOE) rheological workflows, *Cem. Concr. Res.* 197 (2025).
<https://doi.org/10.1016/j.cemconres.2025.107971>.

- [101] M. Nodehi, F. Aguayo, S.E. Nodehi, A. Gholampour, T. Ozbakkaloglu, O. Gencel, Durability properties of 3D printed concrete (3DPC), *Autom. Constr.* 142 (2022) 104479. <https://doi.org/10.1016/j.autcon.2022.104479>.
- [102] Y. Zhang, Y. Zhang, L. Yang, G. Liu, Y. Chen, S. Yu, H. Du, Hardened properties and durability of large-scale 3D printed cement-based materials, *Materials and Structures/Materiaux et Constructions* 54 (2021). <https://doi.org/10.1617/s11527-021-01632-x>.
- [103] X. Sun, J. Zhou, Q. Wang, J. Shi, H. Wang, PVA fibre reinforced high-strength cementitious composite for 3D printing: Mechanical properties and durability, *Addit. Manuf.* 49 (2022) 102500. <https://doi.org/10.1016/j.addma.2021.102500>.
- [104] L. Ma, Q. Zhang, Z. Jia, C. Liu, Z. Deng, Y. Zhang, Effect of drying environment on mechanical properties, internal RH and pore structure of 3D printed concrete, *Constr. Build. Mater.* 315 (2022) 125731. <https://doi.org/10.1016/j.conbuildmat.2021.125731>.
- [105] S. Yu, M. Xia, J. Sanjayan, L. Yang, J. Xiao, H. Du, Microstructural characterization of 3D printed concrete, *Journal of Building Engineering* 44 (2021) 102948. <https://doi.org/10.1016/j.jobe.2021.102948>.
- [106] P. Sikora, M. Techman, K. Federowicz, A.M. El-Khayatt, H.A. Saudi, M. Abd Elrahman, M. Hoffmann, D. Stephan, S.-Y. Chung, Insight into the microstructural and durability characteristics of 3D printed concrete: Cast versus printed specimens, *Case Studies in Construction Materials* 17 (2022) e01320. <https://doi.org/10.1016/j.cscm.2022.e01320>.

- [107] J. Kruger, A. du Plessis, G. van Zijl, An investigation into the porosity of extrusion-based 3D printed concrete, *Addit. Manuf.* 37 (2021) 101740.
<https://doi.org/10.1016/J.ADDMA.2020.101740>.
- [108] R. Alarrak, B. Jeon, A.S. Brand, Fracture properties of extruded fiber-reinforced mortar with preferentially aligned fibers, *Constr. Build. Mater.* 403 (2023).
<https://doi.org/10.1016/j.conbuildmat.2023.133022>.
- [109] L. Pham, P. Tran, J. Sanjayan, Steel fibres reinforced 3D printed concrete: Influence of fibre sizes on mechanical performance, *Constr. Build. Mater.* 250 (2020) 118785. <https://doi.org/10.1016/j.conbuildmat.2020.118785>.
- [110] A.R. Arunothayan, B. Nematollahi, R. Ranade, S.H. Bong, J.G. Sanjayan, K.H. Khayat, Fiber orientation effects on ultra-high performance concrete formed by 3D printing, *Cem. Concr. Res.* 143 (2021) 106384.
<https://doi.org/10.1016/j.cemconres.2021.106384>.
- [111] R.J.M. Wolfs, F.P. Bos, T.A.M. Salet, Hardened properties of 3D printed concrete: The influence of process parameters on interlayer adhesion, *Cem. Concr. Res.* 119 (2019) 132–140. <https://doi.org/10.1016/j.cemconres.2019.02.017>.
- [112] T.T. Le, S.A. Austin, S. Lim, R.A. Buswell, R. Law, A.G.F. Gibb, T. Thorpe, Hardened properties of high-performance printing concrete, *Cem. Concr. Res.* 42 (2012) 558–566. <https://doi.org/10.1016/j.cemconres.2011.12.003>.
- [113] M. Bharti, A. Menon, M. Santhanam, Non-linear behaviour under compression of hardened 3D-printed concrete, (n.d.). <https://doi.org/10.24355/dbbs.084-202408171129-0>.

- [114] F. Bos, C. Menna, A. Robens-Radermacher, R. Wolfs, N. Roussel, H. Lombois-Burger, B. Baz, D. Weger, B. Nematollahi, M. Santhanam, Y. Zhang, S. Bhattacharjee, Z. Jia, Y. Chen, V. Mechtcherine, Mechanical properties of 3D printed concrete: a RILEM TC 304-ADC interlaboratory study — approach and main results, *Mater. Struct.* 58 (2025). <https://doi.org/10.1617/s11527-025-02686-x>.
- [115] Y. Zhang, Y. Zhang, L. Yang, G. Liu, Y. Chen, S. Yu, H. Du, Hardened properties and durability of large-scale 3D printed cement-based materials, *Materials and Structures/Materiaux et Constructions* 54 (2021) 1–14.
<https://doi.org/10.1617/S11527-021-01632-X/FIGURES/11>.
- [116] T. Ding, J. Xiao, S. Zou, X. Zhou, Anisotropic behavior in bending of 3D printed concrete reinforced with fibers, *Compos. Struct.* 254 (2020) 112808.
<https://doi.org/10.1016/j.compstruct.2020.112808>.
- [117] P.K. Mehta, P.J.M. Monteiro, *Concrete: Microstructure, Properties, and Materials*, Fourth Edition, McGraw-Hill, 2014.
- [118] K. Van Tittelboom, M.K. Mohan, B. Šavija, E. Keita, G. Ma, H. Du, J. Kruger, L. Caneda-Martinez, L. Wang, M. Bekaert, T. Wangler, Z. Wang, V. Mechtcherine, N. Roussel, On the micro- and meso-structure and durability of 3D printed concrete elements, *Cem. Concr. Res.* 185 (2024).
<https://doi.org/10.1016/j.cemconres.2024.107649>.
- [119] J.J. Assaad, F. Hamzeh, B. Hamad, Qualitative assessment of interfacial bonding in 3D printing concrete exposed to frost attack, *Case Studies in Construction Materials* 13 (2020) e00357. <https://doi.org/10.1016/j.cscm.2020.e00357>.

- [120] B. Baz, G. Aouad, J. Kleib, D. Bulteel, S. Remond, Durability assessment and microstructural analysis of 3D printed concrete exposed to sulfuric acid environments, *Constr. Build. Mater.* 290 (2021) 123220. <https://doi.org/10.1016/j.conbuildmat.2021.123220>.
- [121] A. Cicione, J. Kruger, R.S. Walls, G. Van Zijl, An experimental study of the behavior of 3D printed concrete at elevated temperatures, *Fire Saf. J.* 120 (2021) 103075. <https://doi.org/10.1016/j.firesaf.2020.103075>.
- [122] L. Gebhard, J. Mata-Falcón, A. Anton, B. Dillenburger, W. Kaufmann, Structural behaviour of 3D printed concrete beams with various reinforcement strategies, *Eng. Struct.* 240 (2021) 112380. <https://doi.org/10.1016/j.engstruct.2021.112380>.
- [123] S.-T. Kang, J.-K. Kim, The relation between fiber orientation and tensile behavior in an Ultra High Performance Fiber Reinforced Cementitious Composites (UHPFRCC), *Cem. Concr. Res.* 41 (2011) 1001–1014. <https://doi.org/10.1016/j.cemconres.2011.05.009>.
- [124] S.Y. Hiew, K. Bin Teoh, S.N. Raman, C.-C. Hung, D.-Y. Yoo, K.-W. Wen, D. Kong, Y.L. Voo, 3D micro-CT driven fibre orientation–confinement correlation model for ultra-high-performance concrete (UHPC), *Cem. Concr. Compos.* 161 (2025) 106081. <https://doi.org/10.1016/j.cemconcomp.2025.106081>.
- [125] K. Bradford, R. Gentry, L. Ben-Alon, K. Kurtis, Construction 3D printing material selection: Minimizing cost and carbon footprint of residential wall assemblies, *Constr. Build. Mater.* 493 (2025) 143150. <https://doi.org/10.1016/j.conbuildmat.2025.143150>.

- [126] Standard Test Method for Flexural Performance of Fiber-Reinforced Concrete (Using Beam With Third-Point Loading), ASTM C1609 (2019).
- [127] Standard Test Method for Measurement of Rate of Absorption of Water by Hydraulic-Cement Concretes, ASTM C1585 (2020).
- [128] M. Khanzadeh Moradillo, Q. Hu, M.T. Ley, Using X-ray imaging to investigate in-situ ion diffusion in cementitious materials, *Constr. Build. Mater.* 136 (2017) 88–98. <https://doi.org/10.1016/j.conbuildmat.2017.01.038>.
- [129] W. Zuo, L. Caneda-Martinez, E. Keita, P. Aïmediou, M. Bornert, N. Roussel, Drying-induced damages in exposed fresh cement-based materials at very early ages: From standard casting to 3D printing, *Cem. Concr. Res.* 185 (2024). <https://doi.org/10.1016/j.cemconres.2024.107614>.
- [130] V. Mechtcherine, S. Muthukrishnan, A. Robens-Radermacher, R. Wolfs, J. Versteeg, C. Menna, O. Ozturk, N. Ozyurt, J. Roupec, C. Richter, J. Jungwirth, L. Miranda, R. Ammann, J.-F. Caron, V. de Bono, R. Monte, I. Navarrete, C. Eugenin, H. Lombois-Burger, B. Baz, M. Sinka, A. Sapata, I. Harbouz, Y. Zhang, Z. Jia, J. Kruger, J.-P. Mostert, M. Štefančič, L. Hanžič, A. Kaci, S. Rahal, M. Santhanam, S. Bhattacharjee, C. Snguanayat, A. Arunothayan, Z. Zhao, I. Mai, I.J. Rasehorn, D. Böhler, N. Freund, D. Lowke, T. Neef, M. Taubert, D. Auer, C.M. Hechtel, M. Dahlenburg, L. Esposito, R. Buswell, J. Kolawole, M.N. Isa, X. Liu, Z. Wang, K. Subramaniam, F. Bos, Mechanical properties of 3D printed concrete: a RILEM 304-ADC interlaboratory study – compressive strength and modulus of elasticity, *Mater. Struct.* 58 (2025). <https://doi.org/10.1617/s11527-025-02688-9>.

- [131] M. van den Heever, A. du Plessis, J. Kruger, G. van Zijl, Evaluating the effects of porosity on the mechanical properties of extrusion-based 3D printed concrete, *Cem. Concr. Res.* 153 (2022) 106695. <https://doi.org/10.1016/j.cemconres.2021.106695>.
- [132] R. Wolfs, J. Versteegen, M. Santhanam, S. Bhattacharjee, F. Bos, A. Robens-Radermacher, S. Muthukrishnan, C. Menna, O. Ozturk, N. Ozyurt, J. Roupec, C. Richter, J. Jungwirth, L. Miranda, R. Ammann, J.-F. Caron, V. de Bono, R. Monte, I. Navarrete, C. Eugenin, H. Lombois-Burger, B. Baz, M. Sinka, A. Sapata, I. Harbouz, Y. Zhang, Z. Jia, J. Kruger, J.-P. Mostert, K. Šter, A. Šajna, A. Kaci, S. Rahal, C. Snguanay, A. Arunothayan, Z. Zhao, I. Mai, I.J. Rasehorn, D. Böhler, N. Freund, D. Lowke, T. Neef, M. Taubert, D. Auer, C.M. Hechtel, M. Dahlenburg, L. Esposito, R. Buswell, J. Kolawole, M.N. Isa, X. Liu, Z. Wang, K. Subramaniam, V. Mechtcherine, Mechanical properties of 3D printed concrete: a RILEM TC 304-ADC interlaboratory study — flexural and tensile strength, *Mater. Struct.* 58 (2025). <https://doi.org/10.1617/s11527-025-02687-w>.
- [133] D.P. Bentz, M.A. Ehlen, C.F. Ferraris, E.J. Garboczi, SORPTIVITY-BASED SERVICE LIFE PREDICTIONS FOR CONCRETE PAVEMENTS, *Proceedings of the International Conference on Concrete Pavements* (2001). <https://doi.org/10.33593/iccp.v7i1.201>.
- [134] S.J. DeSouza, R.D. Hooton, J.A. Bickley, A field test for evaluating high performance concrete covercrete quality, *Canadian Journal of Civil Engineering* 25 (1998) 551–556. <https://doi.org/10.1139/197-110>.

- [135] N.S. Martys, C.F. Ferraris, Capillary transport in mortars and concrete, *Cem. Concr. Res.* 27 (1997) 747–760. [https://doi.org/10.1016/S0008-8846\(97\)00052-5](https://doi.org/10.1016/S0008-8846(97)00052-5).
- [136] L. Reiter, T. Wangler, N. Roussel, R.J. Flatt, The role of early age structural build-up in digital fabrication with concrete, *Cem. Concr. Res.* 112 (2018) 86–95. <https://doi.org/10.1016/j.cemconres.2018.05.011>.
- [137] V. Mechtcherine, F.P. Bos, A. Perrot, W.R.L. da Silva, V.N. Nerella, S. Fataei, R.J.M. Wolfs, M. Sonebi, N. Roussel, Extrusion-based additive manufacturing with cement-based materials – Production steps, processes, and their underlying physics: A review, *Cem. Concr. Res.* 132 (2020) 106037. <https://doi.org/10.1016/j.cemconres.2020.106037>.
- [138] M.A. Schultz, L.J. Struble, Use of oscillatory shear to study flow behavior of fresh cement paste, *Cem. Concr. Res.* 23 (1993) 273–282. [https://doi.org/10.1016/0008-8846\(93\)90092-N](https://doi.org/10.1016/0008-8846(93)90092-N).
- [139] L. Nachbaur, J.C. Mutin, A. Nonat, L. Choplin, Dynamic mode rheology of cement and tricalcium silicate pastes from mixing to setting, *Cem. Concr. Res.* 31 (2001) 183–192. [https://doi.org/10.1016/S0008-8846\(00\)00464-6](https://doi.org/10.1016/S0008-8846(00)00464-6).
- [140] A. Papo, B. Caufin, A study of the hydration process of cement pastes by means of oscillatory rheological techniques, *Cem. Concr. Res.* 21 (1991) 1111–1117. [https://doi.org/10.1016/0008-8846\(91\)90071-O](https://doi.org/10.1016/0008-8846(91)90071-O).
- [141] C.M. Childs, N.R. Washburn, Embedding domain knowledge for machine learning of complex material systems, *MRS Commun.* 9 (2019) 806–820. <https://doi.org/10.1557/mrc.2019.90>.

- [142] Z. Li, T. Pei, W. Ying, W. V. Srubar, R. Zhang, J. Yoon, H. Ye, I. Dabo, A. Radlińska, Can domain knowledge benefit machine learning for concrete property prediction?, *Journal of the American Ceramic Society* 107 (2024) 1582–1602. <https://doi.org/10.1111/jace.19549>.
- [143] R.T. Rios, C.M. Childs, S.H. Smith, N.R. Washburn, K.E. Kurtis, Advancing cement-based materials design through data science approaches, *RILEM Technical Letters* 6 (2021) 140–149. <https://doi.org/10.21809/rilemtechlett.2021.147>.
- [144] M. Sharma, S. Bishnoi, F. Martirena, K. Scrivener, Limestone calcined clay cement and concrete: A state-of-the-art review, *Cem. Concr. Res.* 149 (2021) 106564. <https://doi.org/10.1016/j.cemconres.2021.106564>.
- [145] S. Ferreiro, D. Herfort, J.S. Damtoft, Effect of raw clay type, fineness, water-to-cement ratio and fly ash addition on workability and strength performance of calcined clay – Limestone Portland cements, *Cem. Concr. Res.* 101 (2017) 1–12. <https://doi.org/10.1016/j.cemconres.2017.08.003>.
- [146] B.H. Zaribaf, K.E. Kurtis, Addressing Key Challenges in MK-PLC Blends at Early Ages: Workability, Slump Retention, and Heat of Hydration, in: F. Martirena, A. Favier, K. Scrivener (Eds.), *Calcined Clays for Sustainable Concrete*, Springer, 2018: pp. 500–506. https://doi.org/10.1007/978-94-024-1207-9_80.
- [147] B.H. Zaribaf, B. Uzal, K. Kurtis, Compatibility of Superplasticizers with Limestone-Metakaolin Blended Cementitious System, in: K. Scrivener, A. Favier (Eds.), *Calcined Clays for Sustainable Concrete*, Springer, 2015: pp. 427–434. https://doi.org/10.1007/978-94-017-9939-3_53.

- [148] P. Hou, T.R. Muzenda, Q. Li, H. Chen, S. Kawashima, T. Sui, H. Yong, N. Xie, X. Cheng, Mechanisms dominating thixotropy in limestone calcined clay cement (LC3), *Cem. Concr. Res.* 140 (2021) 106316.
<https://doi.org/10.1016/j.cemconres.2020.106316>.
- [149] B. Lorentz, H. Zhu, D. Mapa, K.A. Riding, A. Zayed, Effect of Clay Mineralogy, Particle Size, and Chemical Admixtures on the Rheological Properties of CCIL and CCI/II Systems, in: S. Bishnoi (Ed.), *Calcined Clays for Sustainable Concrete*, Springer, 2020: pp. 211–218. https://doi.org/10.1007/978-981-15-2806-4_24.
- [150] N.A. Tregger, M.E. Pakula, S.P. Shah, Influence of clays on the rheology of cement pastes, *Cem. Concr. Res.* 40 (2010) 384–391.
<https://doi.org/10.1016/j.cemconres.2009.11.001>.
- [151] T.R. Muzenda, P. Hou, S. Kawashima, T. Sui, X. Cheng, The role of limestone and calcined clay on the rheological properties of LC3, *Cem. Concr. Compos.* 107 (2020) 103516. <https://doi.org/10.1016/j.cemconcomp.2020.103516>.
- [152] K.A. Ibrahim, G.P.A.G. van Zijl, A.J. Babafemi, Influence of limestone calcined clay cement on properties of 3D printed concrete for sustainable construction, *Journal of Building Engineering* 69 (2023) 106186.
<https://doi.org/10.1016/j.jobe.2023.106186>.
- [153] I. Mehdipour, H. Atahan, N. Neithalath, M. Bauchy, E. Garboczi, G. Sant, How clay particulates affect flow cessation and the coiling stability of yield stress-matched cementing suspensions, *Soft Matter* 16 (2020) 3929–3940.
<https://doi.org/10.1039/c9sm02414j>.

- [154] S.A.O. Nair, H. Alghamdi, A. Arora, I. Mehdipour, G. Sant, N. Neithalath, Linking fresh paste microstructure, rheology and extrusion characteristics of cementitious binders for 3D printing, *Journal of the American Ceramic Society* 102 (2019) 3951–3964. <https://doi.org/10.1111/jace.16305>.
- [155] T.-D. Nguyen, T.-H. Tran, N.-D. Hoang, Prediction of interface yield stress and plastic viscosity of fresh concrete using a hybrid machine learning approach, *Advanced Engineering Informatics* 44 (2020) 101057. <https://doi.org/10.1016/j.aei.2020.101057>.
- [156] Y. EL Asri, M. Benaïcha, M. Zaher, A. Hafidi Alaoui, Prediction of plastic viscosity and yield stress of self-compacting concrete using machine learning technics, *Mater. Today Proc.* 59 (2022) A7–A13. <https://doi.org/10.1016/j.matpr.2022.04.891>.
- [157] N. Roussel, G. Ovarlez, S. Garrault, C. Brumaud, The origins of thixotropy of fresh cement pastes, *Cem. Concr. Res.* 42 (2012) 148–157. <https://doi.org/10.1016/j.cemconres.2011.09.004>.
- [158] L. Michel, L. Reiter, A. Sanner, R.J. Flatt, D.S. Kammer, Structural build-up at rest in the induction and acceleration periods of Portland Cement, (2024). <https://doi.org/10.3929/ethz-b-0>.
- [159] N. Roussel, A. Lemaître, R.J. Flatt, P. Coussot, Steady state flow of cement suspensions: A micromechanical state of the art, *Cem. Concr. Res.* 40 (2010) 77–84. <https://doi.org/10.1016/j.cemconres.2009.08.026>.

- [160] A.M. Mostafa, A. Yahia, New approach to assess build-up of cement-based suspensions, *Cem. Concr. Res.* 85 (2016) 174–182.
<https://doi.org/10.1016/j.cemconres.2016.03.005>.
- [161] A.M. Mostafa, A. Yahia, Physico-chemical kinetics of structural build-up of neat cement-based suspensions, *Cem. Concr. Res.* 97 (2017) 11–27.
<https://doi.org/10.1016/j.cemconres.2017.03.003>.
- [162] Q. Yuan, X. Lu, K.H. Khayat, D. Feys, C. Shi, Small amplitude oscillatory shear technique to evaluate structural build-up of cement paste, *Materials and Structures/Materiaux et Constructions* 50 (2017). <https://doi.org/10.1617/s11527-016-0978-2>.
- [163] Q. Yuan, D. Zhou, K.H. Khayat, D. Feys, C. Shi, On the measurement of evolution of structural build-up of cement paste with time by static yield stress test vs. small amplitude oscillatory shear test, *Cem. Concr. Res.* 99 (2017) 183–189.
<https://doi.org/10.1016/j.cemconres.2017.05.014>.
- [164] M. Bellotto, Cement paste prior to setting: A rheological approach, *Cem. Concr. Res.* 52 (2013) 161–168. <https://doi.org/10.1016/j.cemconres.2013.07.002>.
- [165] L.E. Al-Hasani, G. Perez, H.N. Herndon, J. Park, J.L. Poole, I. Tien, N.R. Washburn, Y.K. Cho, T.R. Gentry, K.E. Kurtis, Prediction of heat of hydration of cementitious systems using Gaussian process regression enables mass concrete thermal modeling, *Materials and Structures/Materiaux et Constructions* 56 (2023).
<https://doi.org/10.1617/s11527-023-02134-8>.

- [166] O. Canbek, Q. Xu, Y. Mei, N.R. Washburn, K.E. Kurtis, Predicting the rheology of limestone calcined clay cements (LC3): Linking composition and hydration kinetics to yield stress through Machine Learning, *Cem. Concr. Res.* 160 (2022).
<https://doi.org/10.1016/j.cemconres.2022.106925>.
- [167] A. Menon, C.M. Childs, B. Poczós, N.R. Washburn, K.E. Kurtis, Molecular Engineering of Superplasticizers for Metakaolin-Portland Cement Blends with Hierarchical Machine Learning, *Adv. Theory Simul.* 2 (2019).
<https://doi.org/10.1002/adts.201800164>.
- [168] C. Childs, A. Miller, W. Neiswanger, B. Poczós, L. Stewart, K. Kurtis, N. Washburn, Bayesian machine learning for inverse design of ultra-high-performance concrete, *Philos. Trans. A Math. Phys. Eng. Sci.* 383 (2025) 20240041.
<https://doi.org/10.1098/rsta.2024.0041>.
- [169] J.M. Bone, C.M. Childs, A. Menon, B. Póczos, A.W. Feinberg, P.R. Leduc, N.R. Washburn, Hierarchical Machine Learning for High-Fidelity 3D Printed Biopolymers, *ACS Biomater. Sci. Eng.* 6 (2020) 7021–7031.
<https://doi.org/10.1021/acsbiomaterials.0c00755>.
- [170] A. Menon, B. Póczos, A.W. Feinberg, N.R. Washburn, Optimization of Silicone 3D Printing with Hierarchical Machine Learning, *3D Print. Addit. Manuf.* 6 (2019) 181–189. <https://doi.org/10.1089/3dp.2018.0088>.
- [171] K. Vallurupalli, N. Farzadnia, K.H. Khayat, Effect of flow behavior and process-induced variations on shape stability of 3D printed elements – A review, *Cem. Concr. Compos.* 118 (2021). <https://doi.org/10.1016/j.cemconcomp.2021.103952>.

- [172] K. Vance, G. Sant, N. Neithalath, The rheology of cementitious suspensions: A closer look at experimental parameters and property determination using common rheological models, *Cem. Concr. Compos.* 59 (2015) 38–48.
<https://doi.org/10.1016/j.cemconcomp.2015.03.001>.
- [173] D. Feys, R. Cepuritis, S. Jacobsen, K. Lesage, E. Secrieru, A. Yahia, Measuring Rheological Properties of Cement Pastes: Most common Techniques, Procedures and Challenges, *RILEM Technical Letters* 2 (2017) 129–135.
<https://doi.org/10.21809/rilemtechlett.2017.43>.
- [174] O.H. Wallevik, D. Feys, J.E. Wallevik, K.H. Khayat, Avoiding inaccurate interpretations of rheological measurements for cement-based materials, *Cem. Concr. Res.* 78 (2015) 100–109. <https://doi.org/10.1016/j.cemconres.2015.05.003>.
- [175] T. Liberto, M. Bellotto, A. Robisson, Small oscillatory rheology and cementitious particle interactions, *Cem. Concr. Res.* 157 (2022).
<https://doi.org/10.1016/j.cemconres.2022.106790>.
- [176] M.K. Mohan, A. V. Rahul, Y. Villagran-Zaccardi, G. De Schutter, K. Van Tittelboom, A rheometric approach to assess plastic shrinkage and implications of early age drying on the microstructure of cement-based materials, *Cem. Concr. Res.* 180 (2024). <https://doi.org/10.1016/j.cemconres.2024.107504>.
- [177] C. Seiffert, T.M. Khoshgoftaar, J. Van Hulse, A. Napolitano, RUSBoost: A Hybrid Approach to Alleviating Class Imbalance, *IEEE Transactions on Systems, Man, and Cybernetics - Part A: Systems and Humans* 40 (2010) 185–197.
<https://doi.org/10.1109/TSMCA.2009.2029559>.

- [178] D. Kalyan, *Multiobjective Optimization Using Evolutionary Algorithms*, Wiley, New York, 2001.
- [179] D.P. Bentz, Cement hydration: Building bridges and dams at the microstructure level, *Materials and Structures/Materiaux et Constructions* 40 (2007) 397–404. <https://doi.org/10.1617/s11527-006-9147-3>.
- [180] O. Canbek, N.R. Washburn, K.E. Kurtis, Rheology of Limestone Calcined Clay Cements (LC3): Predictive Modeling of Yield Stress and Plastic Viscosity with Machine Learning, in: K. Scrivener, M. Sharma, F. Zunino (Eds.), *Calcined Clays for Sustainable Concrete*, Springer, Cham, 2025: pp. 447–456. https://doi.org/10.1007/978-3-031-83889-7_42.
- [181] L. Lei, M. Palacios, J. Plank, A.A. Jeknavorian, Interaction between polycarboxylate superplasticizers and non-calcined clays and calcined clays: A review, *Cem. Concr. Res.* 154 (2022). <https://doi.org/10.1016/j.cemconres.2022.106717>.
- [182] H. Bessaies-Bey, K.H. Khayat, M. Palacios, W. Schmidt, N. Roussel, Viscosity modifying agents: Key components of advanced cement-based materials with adapted rheology, *Cem. Concr. Res.* 152 (2022). <https://doi.org/10.1016/j.cemconres.2021.106646>.
- [183] J. Chen, J. Plank, Calcined clays for climate neutral (“net zero”) cements: shear-dependent rheological behavior and application performance, *Cem. Concr. Compos.* 162 (2025). <https://doi.org/10.1016/j.cemconcomp.2025.106145>.

- [184] E.G. Burns, D.F. Ferraz, N.A. Tregger, Characterizing Sticky Concrete from Rheological Perspective, *ACI Mater. J.* 118 (2021) 421–429.
<https://doi.org/10.14359/51734154>.
- [185] S. Real, P. Bowen, R. Moreno, L. González-Panicello, F. Puertas, M. Hanafi, M. Palacios, Impact of pore solution composition and superplasticizers on the interparticle forces and rheology of metakaolin suspensions, *Cem. Concr. Res.* 195 (2025). <https://doi.org/10.1016/j.cemconres.2025.107901>.
- [186] L. Ferrari, J. Kaufmann, F. Winnefeld, J. Plank, Interaction of cement model systems with superplasticizers investigated by atomic force microscopy, zeta potential, and adsorption measurements, *J. Colloid Interface Sci.* 347 (2010) 15–24.
<https://doi.org/10.1016/j.jcis.2010.03.005>.
- [187] D. Lowke, Thixotropy of SCC—A model describing the effect of particle packing and superplasticizer adsorption on thixotropic structural build-up of the mortar phase based on interparticle interactions, *Cem. Concr. Res.* 104 (2018) 94–104.
<https://doi.org/10.1016/j.cemconres.2017.11.004>.
- [188] H. Bessaies-Bey, X. Yu, W. Zuo, O. Ahmadah, J. Deou, L. Caneda-Martínez, N. Roussel, Packing properties assessment of cement and alternative powders: Artefacts and protocols, *Cem. Concr. Res.* 186 (2024).
<https://doi.org/10.1016/j.cemconres.2024.107685>.
- [189] F. De Larrard, *Concrete Mixture Proportioning*, CRC Press, 1999.
<https://doi.org/10.1201/9781482272055>.

- [190] C. Szeto, Q. Jin, F. Zunino, K.E. Kurtis, Assessment of particle packing approach for design of low-clinker, LC3 binders at low water-to-solids ratio, *Cem. Concr. Compos.* 161 (2025) 106104. <https://doi.org/10.1016/j.cemconcomp.2025.106104>.
- [191] L.G. Li, A.K.H. Kwan, Concrete mix design based on water film thickness and paste film thickness, *Cem. Concr. Compos.* 39 (2013) 33–42. <https://doi.org/10.1016/j.cemconcomp.2013.03.021>.
- [192] A.K.H. Kwan, L.G. Li, Combined effects of water film thickness and paste film thickness on rheology of mortar, *Mater. Struct.* 45 (2012) 1359–1374. <https://doi.org/10.1617/s11527-012-9837-y>.
- [193] A.K.H. Kwan, W.W.S. Fung, H.H.C. Wong, Water film thickness, flowability and rheology of cement–sand mortar, *Advances in Cement Research* 22 (2010) 3–14. <https://doi.org/10.1680/adcr.2008.22.1.3>.
- [194] A. Zingg, F. Winnefeld, L. Holzer, J. Pakusch, S. Becker, L. Gauckler, Adsorption of polyelectrolytes and its influence on the rheology, zeta potential, and microstructure of various cement and hydrate phases, *J. Colloid Interface Sci.* 323 (2008) 301–312. <https://doi.org/10.1016/j.jcis.2008.04.052>.
- [195] J.R. Martins, J.C. Rocha, R.M. Novais, J.A. Labrincha, D. Hotza, L. Senff, Zeta potential in cementitious systems: A comprehensive overview of influencing factors and implications on material properties, *Journal of Building Engineering* 99 (2025). <https://doi.org/10.1016/j.jobbe.2024.111556>.

- [196] D. Lowke, C. Gehlen, The zeta potential of cement and additions in cementitious suspensions with high solid fraction, *Cem. Concr. Res.* 95 (2017) 195–204.
<https://doi.org/10.1016/j.cemconres.2017.02.016>.
- [197] L.R.M. de Miranda, K. Lesage, G. De Schutter, N. Roussel, Concrete printing through lace pressing: Head, shoulders, knees and toes, *Cem. Concr. Res.* 197 (2025). <https://doi.org/10.1016/j.cemconres.2025.107968>.
- [198] A. Geffrault, H. Bessaies-Bey, N. Roussel, P. Coussot, Printing by yield stress fluid shaping, *Addit. Manuf.* 75 (2023). <https://doi.org/10.1016/j.addma.2023.103752>.
- [199] H. Kemer, R. Bouras, N. Mesboua, M. Sonebi, O. Kinnane, Shear-thickening behavior of sustainable cement paste — Controlling physical parameters of new sources of supplementary cementitious materials, *Constr. Build. Mater.* 310 (2021) 125277. <https://doi.org/10.1016/j.conbuildmat.2021.125277>.
- [200] M. Cyr, C. Legrand, M. Mouret, Study of the shear thickening effect of superplasticizers on the rheological behaviour of cement pastes containing or not mineral additives, *Cem. Concr. Res.* 30 (2000) 1477–1483.
[https://doi.org/10.1016/S0008-8846\(00\)00330-6](https://doi.org/10.1016/S0008-8846(00)00330-6).
- [201] A. Yahia, Shear-thickening behavior of high-performance cement grouts — Influencing mix-design parameters, *Cem. Concr. Res.* 41 (2011) 230–235.
<https://doi.org/10.1016/j.cemconres.2010.11.004>.
- [202] J.F. Morris, Lubricated-to-frictional shear thickening scenario in dense suspensions, *Phys. Rev. Fluids* 3 (2018) 110508.
<https://doi.org/10.1103/PhysRevFluids.3.110508>.

- [203] E. Brown, N.A. Forman, C.S. Orellana, H. Zhang, B.W. Maynor, D.E. Betts, J.M. DeSimone, H.M. Jaeger, Generality of shear thickening in dense suspensions, *Nat. Mater.* 9 (2010) 220–224. <https://doi.org/10.1038/nmat2627>.
- [204] A.N. Seshadri, M. Kaboolian, Y.J. Chen, A.M. Ardekani, J.P. Youngblood, K. Weigandt, K.A. Erk, R.D. Corder, Effects of non-adsorbing polymer molecular weight on the rheology and microstructure of dense suspensions, *Rheol. Acta* (2025). <https://doi.org/10.1007/s00397-025-01501-2>.
- [205] A. Perrot, D. Rangeard, V.N. Nerella, V. Mechtcherine, Extrusion of cement-based materials - an overview, *RILEM Technical Letters* 3 (2018) 91–97. <https://doi.org/10.21809/rilemtechlett.2018.75>.
- [206] R.J.M. Wolfs, T.A.M. Salet, N. Roussel, Filament geometry control in extrusion-based additive manufacturing of concrete: The good, the bad and the ugly, *Cem. Concr. Res.* 150 (2021) 106615. <https://doi.org/10.1016/j.cemconres.2021.106615>.
- [207] A. Perrot, D. Rangeard, Y. Mélinge, Prediction of the ram extrusion force of cement-based materials, *Applied Rheology* 24 (2014). <https://doi.org/10.3933/APPLRHEOL-24-53320>.
- [208] John. Benbow, J.. Bridgwater, *Paste flow and extrusion*, Clarendon Press ; Oxford University Press, 1993.
- [209] A. Perrot, Y. Mélinge, D. Rangeard, F. Micaelli, P. Estellé, C. Lanos, Use of ram extruder as a combined rheo-tribometer to study the behaviour of high yield stress fluids at low strain rate, *Rheol. Acta* 51 (2012) 743–754. <https://doi.org/10.1007/s00397-012-0638-6>.

- [210] P.R. de Matos, T. Zat, M.M. Lima, J. da S. Andrade Neto, M.T. Souza, E.D. Rodríguez, Effect of the superplasticizer addition time on the fresh properties of 3D printed limestone calcined clay cement (LC3) concrete, *Case Studies in Construction Materials* 19 (2023) e02419.
<https://doi.org/10.1016/j.cscm.2023.e02419>.
- [211] Y. Chen, S. He, Y. Zhang, Z. Wan, O. Çopuroğlu, E. Schlangen, 3D printing of calcined clay-limestone-based cementitious materials, *Cem. Concr. Res.* 149 (2021). <https://doi.org/10.1016/j.cemconres.2021.106553>.
- [212] M.A.B. Beigh, V.N. Nerella, C. Schröfl, V. Mechtcherine, Studying the Rheological Behavior of Limestone Calcined Clay Cement (LC3) Mixtures in the Context of Extrusion-Based 3D-Printing, in: *RILEM Bookseries*, Springer, 2020: pp. 229–236. https://doi.org/10.1007/978-981-15-2806-4_26.
- [213] L. Ferrari, G. Rizzieri, L. Ferrara, E. Franzoni, Rheological control of cementitious composites incorporating ceramic wastes for 3D printing applications, *Cem. Concr. Compos.* 167 (2026) 106452. <https://doi.org/10.1016/j.cemconcomp.2025.106452>.
- [214] S.A.O. Nair, A. Tripathi, N. Neithalath, Examining layer height effects on the flexural and fracture response of plain and fiber-reinforced 3D-printed beams, *Cem. Concr. Compos.* 124 (2021) 104254.
<https://doi.org/10.1016/j.cemconcomp.2021.104254>.
- [215] B. Zahabizadeh, J. Pereira, C. Gonçalves, E.N.B. Pereira, V.M.C.F. Cunha, Influence of the printing direction and age on the mechanical properties of 3D

- printed concrete, *Mater. Struct.* 54 (2021) 73. <https://doi.org/10.1617/s11527-021-01660-7>.
- [216] D. Dey, A. Sahu, S. Prakash, B. Panda, A study into the effect of material deposition methods on hardened properties of 3D printed concrete, *Mater. Today Proc.* (2023). <https://doi.org/10.1016/j.matpr.2023.03.034>.
- [217] Y. Tang, J. Xiao, T. Ding, H. Liu, M. Zhang, J. Zhang, Trans-layer and inter-layer fracture behavior of extrusion-based 3D printed concrete under three-point bending, *Eng. Fract. Mech.* 296 (2024) 109836. <https://doi.org/10.1016/j.engfracmech.2023.109836>.
- [218] J. Ye, M. Yang, J. Yu, Y. Dai, B.B. Yin, Y. Weng, Size effect on flexural and fracture behaviors of 3D printed engineered cementitious composites: Experimental and numerical studies, *Eng. Struct.* 298 (2024). <https://doi.org/10.1016/j.engstruct.2023.117062>.
- [219] M. Chen, J. Cheng, T. Zhang, Y. Wang, Experimental characterization and constitutive modelling of the anisotropic dynamic compressive behavior of 3D printed engineered cementitious composites, *Cem. Concr. Compos.* 160 (2025). <https://doi.org/10.1016/j.cemconcomp.2025.105995>.
- [220] F. Mukhtar, 3D-printed concrete fracture: Effects of cohesive laws, mixes, and print parameters in 3D eXtended FEM, *Comput. Struct.* 315 (2025). <https://doi.org/10.1016/j.compstruc.2025.107822>.
- [221] K.S. Kompella, M. Levi, L. Ferrara, Identifying interlayer fracture properties in 3D printed concrete specimens via multidirectional flexural tests, in: *International*

Association for Fracture Mechanics of Concrete and Concrete Structures, 2025.
<https://doi.org/10.21012/fc12.1362>.

- [222] D. Asprone, C. Menna, F.P. Bos, T.A.M. Salet, J. Mata-Falcón, W. Kaufmann, Rethinking reinforcement for digital fabrication with concrete, *Cem. Concr. Res.* 112 (2018) 111–121. <https://doi.org/10.1016/J.CEMCONRES.2018.05.020>.
- [223] S.H. Bong, B. Nematollahi, V. Mechtcherine, V.C. Li, K.H. Khayat, Three-Dimensional-Printed Engineered, Strain-Hardening Geopolymer Composite as Permanent Formwork for Construction of Reinforced Concrete Beam, *ACI Struct. J.* 121 (2024) 37–48. <https://doi.org/10.14359/51739159>.
- [224] Z. Wu, H. Rong, J. Zheng, F. Xu, W. Dong, An experimental investigation on the FPZ properties in concrete using digital image correlation technique, *Eng. Fract. Mech.* 78 (2011) 2978–2990. <https://doi.org/10.1016/j.engfracmech.2011.08.016>.
- [225] S.G. Shah, J.M. Chandra Kishen, Fracture Properties of Concrete–Concrete Interfaces Using Digital Image Correlation, *Exp. Mech.* 51 (2011) 303–313. <https://doi.org/10.1007/s11340-010-9358-y>.
- [226] D. Corr, M. Accardi, L. Graham-Brady, S. Shah, Digital image correlation analysis of interfacial debonding properties and fracture behavior in concrete, *Eng. Fract. Mech.* 74 (2007) 109–121. <https://doi.org/10.1016/j.engfracmech.2006.01.035>.
- [227] T.C. Chu, W.F. Ranson, M.A. Sutton, Applications of digital-image-correlation techniques to experimental mechanics, *Exp. Mech.* 25 (1985) 232–244. <https://doi.org/10.1007/BF02325092>.

- [228] M.A. Sutton, J.J. Orteu, H. Schreier, Image correlation for shape, motion and deformation measurements: Basic concepts, theory and applications, Springer US, 2009. <https://doi.org/10.1007/978-0-387-78747-3>.
- [229] F. Bos, V. Mechtcherine, N. Roussel, C. Menna, R. Wolfs, H. Lombois-Burger, B. Baz, D. Weger, S. Moro, B. Nematollahi, M. Santhanam, Y. Zhang, S. Bhattacharjee, Z. Jia, Y. Chen, RILEM TC 304-ADC ILS-mech Study Plan, 2023.
- [230] R. Munemo, J. Kruger, G.P.A.G. van Zijl, Surface treatment of 3DPC interlayers with silicate-based solution for enhanced interfacial bonding, *Cem. Concr. Res.* 196 (2025). <https://doi.org/10.1016/j.cemconres.2025.107948>.
- [231] J. Van Der Putten, G. De Schutter, K. Van Tittelboom, Surface modification as a technique to improve inter-layer bonding strength in 3D printed cementitious materials, *RILEM Technical Letters* 4 (2019) 33–38. <https://doi.org/10.21809/rilemtechlett.2019.84>.